A national laboratory of the U.S. Department of Energy
Office of Energy Efficiency & Renewable Energy

NREL National Renewable Energy Laboratory

Innovation for Our Energy Future

# High Efficiency and High Rate Deposited Amorphous Silicon-Based Solar Cells

## Final Technical Report
## 1 September 2001 – 6 March 2005

*Subcontract Report*
NREL/SR-520-39091
January 2006

X. Deng
*University of Toledo*
*Toledo, Ohio*

NREL is operated by Midwest Research Institute ● Battelle    Contract No. DE-AC36-99-GO10337

# High Efficiency and High Rate Deposited Amorphous Silicon-Based Solar Cells

*Subcontract Report*
NREL/SR-520-39091
January 2006

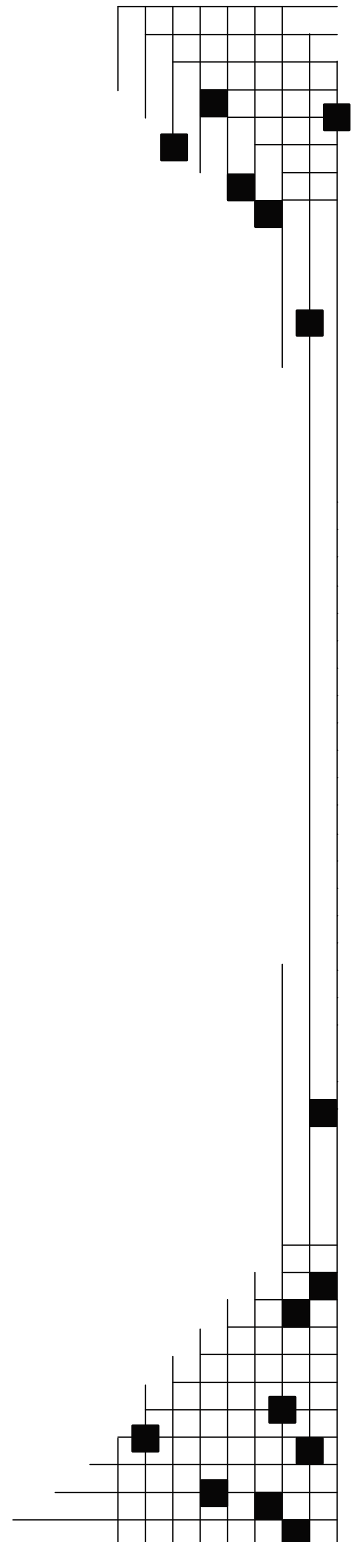

## Final Technical Report
## 1 September 2001 – 6 March 2005


X. Deng
*University of Toledo*
*Toledo, Ohio*


NREL Technical Monitor: Bolko von Roedern
Prepared under Subcontract No. NDJ-2-30630-08


**National Renewable Energy Laboratory**
**1617 Cole Boulevard, Golden, Colorado 80401-3393**
**303-275-3000 • www.nrel.gov**

Operated for the U.S. Department of Energy
Office of Energy Efficiency and Renewable Energy
by Midwest Research Institute • Battelle

Contract No. DE-AC36-99-GO10337

**This publication was reproduced from the best available copy submitted by the subcontractor and received no editorial review at NREL.**

**NOTICE**

This report was prepared as an account of work sponsored by an agency of the United States government. Neither the United States government nor any agency thereof, nor any of their employees, makes any warranty, express or implied, or assumes any legal liability or responsibility for the accuracy, completeness, or usefulness of any information, apparatus, product, or process disclosed, or represents that its use would not infringe privately owned rights. Reference herein to any specific commercial product, process, or service by trade name, trademark, manufacturer, or otherwise does not necessarily constitute or imply its endorsement, recommendation, or favoring by the United States government or any agency thereof. The views and opinions of authors expressed herein do not necessarily state or reflect those of the United States government or any agency thereof.

Available electronically at http://www.osti.gov/bridge

Available for a processing fee to U.S. Department of Energy and its contractors, in paper, from:
U.S. Department of Energy
Office of Scientific and Technical Information
P.O. Box 62
Oak Ridge, TN 37831-0062
phone: 865.576.8401
fax: 865.576.5728
email: mailto:reports@adonis.osti.gov

Available for sale to the public, in paper, from:
U.S. Department of Commerce
National Technical Information Service
5285 Port Royal Road
Springfield, VA 22161
phone: 800.553.6847
fax: 703.605.6900
email: orders@ntis.fedworld.gov
online ordering: http://www.ntis.gov/ordering.htm

Printed on paper containing at least 50% wastepaper, including 20% postconsumer waste

# Summary

This final technical report covers the highlights of the research activities and results on the project of "High Efficiency and High-Rate Deposited Amorphous Silicon-Based Solar Cells" at the University of Toledo for the Period of September 1, 2001 to March 6, 2005, under NREL Subcontract No. NDJ-2- 30630-08.

**Project Objective**:

The objectives of this project are: (1) to establish a transferable knowledge and technology base for the fabrication of high-efficiency triple-junction a-Si-based solar cells, and (2) to develop high-rate deposition techniques for the growth of a-Si-based and related alloys including poly-Si, μc-Si, a-SiGe and a-Si films and photovoltaic devices with these materials.

**Approaches/Tasks:**

The approaches and tasks toward the project objectives are outlined as follows:

1) Developing a "grand phase diagram" of deposition conditions for the growth of protocrystalline silicon and protocrystalline silicon germanium alloys and use these materials for the fabrication of top, middle, and bottom component cells of spectrum-splitting triple-junction solar cells;

2) Exploring the deposition of a-Si-based materials using new chemical precursors including trisilane;

3) Studying the impact of mismatch of band edges at the interfaces on the solar cell I-V characteristics and the physics of buffer layers;

4) Combining these improvements made in component cells and fabricating triple cells with high stable, total-area efficiency;

5) Developing a technique to measure component cell I-V performance in a two-terminal triple stack;

6) Performing AMPS modeling on triple cells and comparing the modeling results with the actual fabricated triple-cell devices;

7) Fabricating poly-Si, μc-Si, a-SiGe and a-Si at high rates using a newly developed hot-wire system that employs a coiled filament design with multiple gas inlets allowing us to inject gases with and without going through the coiled filament; and depositing a-SiGe and a-Si at high rates using VHF plasma.

**Accomplishments and Results:**

Major accomplishments and results for this project include the following:

Phase I (Sept. 01, 2001 – Aug. 31, 2002):

1) We have studied the phase diagram for a-Si deposition for different hydrogen dilution R and substrate temperature $T_s$ and found that the transition from amorphous to microcrystalline occurs with lower hydrogen dilution R at $T_s \sim 200$ °C. At higher and lower $T_s$, higher R is needed to deposit microcrystalline silicon films.

2) We have installed trisilane gas for deposition of a-Si based materials.

3) We have studied extensively two interfaces: a) the p-i interface and b) the $p^+$-$n^+$ interface at the tunnel junctions. We have found that the p-layer optimized for a-Si top cell causes severe J-V roll-over when it is used for narrow bandgap a-SiGe alloys. It was concluded that the band mismatch at the p-i interface prevents holes from being collected at the p-layer under a forward bias near $V_{oc}$ point (when the field is weakened). We have also studied $p^+$-$n^+$ interface at the tunnel junction.

4) We have fabricated triple-junction solar cells to improve efficiency of triple-junction solar cells. Many of these solar cells show initial, active-area efficiency exceeding 12% and stabilized efficiency around 10.5-11%.

5) We have established a procedure that is expected to allow us to measure the J-V of component cells in a triple-junction stack.

6) We have performed modeling work in conjunction with the fabrication of triple cells. We have also performed modeling research on single-junction solar cells to study the interface behavior.

7) We have conducted extensive research using a hot-wire CVD process. a-Si films was deposited at a deposition rate up to 240 Å/s. These films show a low microstructure R*. Unfortunately, a-Si films deposited at a low Ts and without H dilution, at a rate up to 800 Å/s, are porous.

Phase II (Sept. 01, 2002 – Aug. 31, 2003):

1) We studied the phase diagram for a-Si deposition for different $H_2$ dilution and substrate temperature $T_s$. In order to be able to cover a broader parameter space within a limited time, we designed and installed a load lock chamber that allows us to load in simultaneously a set of ten 4”x4” masks with different patterns of coverage for the deposition. In this way, we could explore a large set of parameters in a single vacuum pump down. We have also studied the deposition of protocrystalline Si and SiGe using RF PECVD and HWCVD during this program period.

2) We have performed a systematic study of Si:H deposition using $Si_3H_8$ and $Si_2H_6$ In this study, Si:H films and solar cells deposited using $Si_3H_8$ and using $Si_2H_6$ have been compared. At the same hydrogen dilution, $Si_3H_8$ leads to higher deposition rate. However, at the same atomic ratio of hydrogen and silicon, the deposition rate of Si:H using $Si_3H_8$ and $Si_2H_6$ is approximately the same. The deposition rate is more influenced by the ratio of the total number of Si atoms to hydrogen atoms introduced into the chamber rather than the number of Si-containing molecules. Measurement of activation energy, microstructure and photosensitivity indicate that a) the transition from amorphous to amorphous/nanocrystalline mixed phase occurs at a higher $H_2$ dilution level when $Si_3H_8$ is used; and b) the transition from amorphous to mixed phase is more gradual for $Si_3H_8$ as compared with $Si_2H_6$. This suggests that the window of parameter space for deposition of high-quality protocrystalline silicon may be wider when $Si_3H_8$ is used as compared with $Si_2H_6$ and $SiH_4$.

3) We have studied nanometer-sized p-layer that forms a desirable hetero-interface with the intrinsic absorber layer and yet has minimal optical absorption. A multiple-sublayer approach is used to meet these two requirements simultaneously. Using such a multiple-sublayered nanometer-sized p-layer, we achieved single-junction a-SiGe solar cells with initial efficiency approximately 12.5% and stabilized efficiency of 10.5% (not yet independently confirmed). A US utility patent application was filed for the p-layer concept. In addition, we have designed and partially completed the installation of a 5-chamber addition to UT's existing four-chamber PECVD/HWCVD systems. Four of the five chambers are used for the sputter deposition of metal (Al, Ag, etc), ZnO, ITO, $SiO_2$ layers and the fifth one is a new load-lock chamber capable of simultaneously loading 10 substrates, masks, or combinations of substrates and masks. This system allows us to complete the entire 12 layers of a triple-junction solar cell, Al/ZnO/nip/nip/nip/ITO in a single vacuum pump down, thus avoiding the undesirable air exposure at some of the critical interfaces. The ability to control the air exposure at these interfaces could lead us to understand and analyze the optical and electrical losses at these interfaces such as ZnO/n and p-ITO interfaces. The design and the process optimization of these five new chambers is supported by this NREL-funded project while the acquisition of components and the installation are supported by a complementary project funded by Air Force Research Lab.

4) Activities in this task area is mostly focused on 1) the optimization of top component cell, as summarized in Section 3; 2) the optimization of the sputter deposition of ITO, Al, ZnO in one of the new sputter deposition chambers; 3) the generation of metal fingers using lithography; and 4) deposition of triple-junction a-Si based solar cells. We fabricated wide band gap a-Si top cells with 11.1% initial efficiency and top cells with $V_{oc} = 1.023V$ and FF = 0.78 using improved intrinsic and doped layers. We maintained our baseline deposition of triple-junction solar cells with initial active-area efficiency >12%.

5) We developed the methodology for measuring component cell I-V characteristics in a two-terminal tandem and triple-junction stack.

6) We started using Advanced Semiconductor Analysis (ASA) program developed by Delft University to complement our modeling work using AMPS.

7) Under this task area, we continued our study of the deposition of Si:H materials using HWCVD and VHF PECVD. In the HWCVD area, we studied the effect of the Si:H growth on different filament geometry. We also studied SiGe:H materials with different Ge content in the film and the deposition of amorphous and nanocrystalline SiGe:H alloys using different amounts of hydrogen dilution. In the VHF PECVD area, new matching box was installed. The modification of hardware allows us to incorporate more power into the plasma and leads to higher deposition rate. Study of the deposition uniformity was also carried out. It was found that the film uniformity is the highest when the chamber pressure was kept near 0.35 Torr in our deposition system.

In addition, in collaboration with Syracuse University, we completed a comprehensive review chapter, "Amorphous Silicon Related Solar Cells", in Handbook of Photovoltaic Engineering, ed. A. Luque & S. Hegedus, John Wiley & Sons, Ltd. , June 2003. This $60^+$-page chapter reviews the science and technology related to a-Si:H photovoltaics.

Phase III (Sept. 01, 2003 – March 06, 2005):

1) We have achieved: a). a-SiGe single-junction solar cells with >12.5% initial, active-area efficiency; b). a-Si/a-SiGe tandem-junction solar cells with >12.5% initial, active-area efficiency; c). a-Si/a-SiGe/a-SiGe triple-junction solar cells with >12.5% initial, active-area efficiency.

2) We have completed the construction of a five-chamber addition to UT's four-chamber solar cell deposition system. Among the five new chambers, four are for the sputter deposition of Ag(Al), ZnO, ITO and other non standard materials. The load lock chamber has an "elevator" that allows the use of ten substrates/masks with one pump down. The substrates and masks could be changed in situ without breaking the system vacuum. The deposition of back reflector layers (Al/ZnO and Ag/ZnO) and top conducting electrode (ITO) have been optimized. Triple-junction solar cells using this new 9-chamber deposition system have been fabricated on a routine basis.

3) We have studied VHF deposition of a-Si and nc-Si at high rate. Investigated deposition conditions that lead to uniform deposition at high rate. Fabricated nc-Si based single-junction solar cells.

4) We have performed High Resolution TEM study of p-layer materials that lead to high Voc a-Si solar cells. Concluded that the p-layer that leads to high Voc contains nc-Si particles, about 2nm to 3nm in size, imbedded in a-Si matrix. It is further concluded that the mixed phase p-layer with a higher volume fraction of nc-Si:H phase, within the range studied, leads to a higher $V_{oc}$. The optimum p-layer material for nip-type a-Si:H solar cells is neither at the onset of the transition between amorphous to (amorphous and nanocrystalline) mixed phase nor a nanocrystalline/microcrystalline material with a high volume fraction of crystalline phase. Optical transmission measurements show that the *nc*-Si *p*-layer has a wide bandgap of 1.96 eV, due to the quantum confinement effects (QCE). Using this kind of *p*-layer in *n-i-p* *a*-Si:H solar cells, the cell performances were improved with a $V_{oc}$ of 1.042 V, while the

solar cell deposited under a similar condition but incorporating a hydrogenated microcrystalline silicon (*μc*-Si:H) *p*-layer leads to a $V_{oc}$ of 0.526 V.

5) We have modeled and simulated triple-junction a-Si solar cells using the Advanced Semiconductor Analysis (ASA). The device performance is analyzed with numerically simulated I-V characteristics. We have studied several failure scenarios such as variations in the thickness of different layers of the multilayered triple-junction structure. Distinctive features of the I-V characteristics and solar parameters have been found which have been correlated and discussed with the basis of device physics.

6) We have developed a light-assisted electrochemical shunt passivation process with improved effectiveness in removing shunts and shorts in a-Si. A patent application was filed in US Patent and Trade Mark office.

7) We have employed the novel technique developed at UT to measure the component cell current-voltage characteristics in a multiple-junction stack. Demonstrated the I-V measurement of component cells in tandem-junction solar cells.

8) We have fabricated prototype minimodules (4"x4" and 4"x8" sizes) using a-SiGe based solar cells. The minimodules are encapsulated with silicone elastomer.

# Table of Contents

**Summary** ........ iii

**Table of Contents** ........ viii

**List of Figures** ........ ix

**List of Tables** ........ xii

**1 Introduction** ........ 1

**2 Triple-Junction a-Si Solar Cells with Heavily Doped Thin Interface Layers at the Tunnel Junctions** ...... 5

**3 High-Efficiency Single-junction a-SiGe Solar Cells** ........ 11

**4 Optimization of High-efficiency a-Si Top Cell** ........ 17

**5 Raman and IR study of narrow bandgap a-SiGe and μc-SiGe films deposited using different hydrogen dilution** ........ 20

**6 Phase Diagram for Deposition of Amorphous and Microcrystalline Silicon** ........ 27

**7 High Rate Deposition of Amorphous Silicon Films Using Hot-Wire CVD with Coil-Shaped Filament** ... 34

**8 Deposition of a-SiGe:H and nc-SiGe:H Films Using HWCVD** ........ 40

**9 Amorphous Silicon Deposited Using Trisilane as Precursor** ........ 48

**10 Fine-Grained Nanocrystalline Silicon p-Layer for High-$V_{oc}$ a-Si:H Solar Cells** ........ 58

**11 Hydrogenated Nanocrystalline Silicon *p*-Layer in *a*-Si:H *n-i-p* Solar Cells** ........ 63

**12 Modeling of Triple Junction a-Si Solar Cells Using ASA: Analysis of Device Performance under Various Failure Scenarios** ........ 69

**13 Measurement of Component-Cell Current-Voltage Characteristics in a Tandem-Junction Two-Terminal Solar Cell** ........ 73

**14 Amorphous Silicon Based Minimodules with Silicone Elastomer Encapsulation** ........ 81

**15 Expansion of UT's Fabrication Capability for Triple-Junction Amorphous Silicon Based Solar Cells** .. 84

# List of Figures

Fig. 2-1: IV curve of a UT fabricated triple cell, showing 12.7% initial, active-area efficiency. ................................8

Fig. 2-2: Quantum efficiency curve of 12.7% cell (GD585) showing the QE for top, middle and bottom cells. The figure also shows the short circuit current under UT simulator and AM1.5 spectrum. ........................................8

Fig. 2-3: IV curve of GD585 measured at NREL, showing 11.8% initial, total-area efficiency. ................................9

Fig. 2-4: I-V curve of a triple cell showing 10.7% stable efficiency ..........................................................................10

Fig. 3-1: Schematic of the device showing the p-layer with sublayers deposited at different temperature. ................12

Fig. 3-2: J-V curves of a-SiGe cell (GD904-2.32) measured before and after light soaking for 100 and 3300 hours, showing 10.47% stable, active-area efficiency. ..........................................................................................14

Fig. 3-3: J-V curve of a single-junction a-SiGe solar cell with initial, active-area efficiency of around 13%. ..........15

Fig. 4-1: An optimized top cell deposited on Ag/ZnO back reflector, showing 11.1% initial, active-area efficiency.18

Fig. 4-2: J-V curve of an improved a-Si solar cell showing 1.023 V open circuit voltage and 78% fill factor. The current is such that it is ideal for use as the top cell of a triple cell. ..................................................................19

Fig. 5-1(a): FTIR absorption spectra of a-SiGe:H films in the range from 400 to 800 $cm^{-1}$. The IR spectra were taken from the samples deposited under H-dilution $R_H$ = 1.7 (GD419), 10 (GD420), 30 (GD422), 50 (GD423), 120 (GD424), 180 (GD449) and 240 (GD450), respectively ......................................................................21

Fig. 5-1(b): FTIR absorption spectra of a-SiGe:H films in the range from 1800 to 2200 $cm^{-1}$ . The IR spectra were taken from the same samples as in Fig. 5-1(a).........................................................................................22

Fig. 5-2: The relative intensity $I_{2090}$ and hydrogen content $C_H$ of a-SiGe:H samples as a function of H-dilution $R_H$ .23

Fig. 5-3: Raman spectra of high H-dilution a-SiGe:H samples, with $R_H$=120 (GD424), 180 (GD449) and 240 (GD450), respectively. The Raman spectra were taken from the front surface of the samples, except GD450R, which was taken from the back side of sample GD450 through the glass substrate...........................................24

Fig. 6-1: Calibration of actual substrate temperature from the reading temperature for UT's PECVD deposition system. ..........................................................................................................................................28

Fig. 6-2: Voc of nip solar cells as a function of hydrogen dilution for different substrate temperatures.....................31

Fig. 6-3: Contour plot of the Voc as a function of substrate temperature and H dilution. ..........................................31

Fig. 6-4: Phase diagram for the a-Si and microcrystalline growth in Ts-R plot. .......................................................32

Fig. 7-1: Schematic diagram of the Hot Wire CVD deposition chamber. ..................................................................35

Fig. 8-1: Dependence of the deposition rate $r_{dep}$ on the filament temperature $T_{fil}$ and the substrate Temperature $T_{sub}$ at a $Si_2H_6$ flow rate $F_{Si2H6}$ = 3.4 sccm, $GeH_4$ flow rate $F_{GeH4}$ = 1.7 sccm, $H_2$ flow rate $F_{H2}$ = 7.0 sccm, a total process pressure p = 3.1 mtorr. .........................................................................................................42

Fig. 8-2: Top-view SEM images of SiGe samples deposited at a $Si_2H_6$ flow rate $F_{Si2H6}$ = 3.4 sccm, $GeH_4$ flow rate $F_{GeH4}$ = 1.7 sccm, $H_2$ flow rate $F_{H2}$ = 7.0 sccm, a total process pressure p = 3.1 mtorr using a) $T_{fil}$ =1800 °C and $T_{sub}$ = 200°C, b) $T_{fil}$ =1800 °C and $T_{sub}$ = 300°C, c) $T_{fil}$ =2000 °C and $T_{sub}$ = 200°C, and d) $T_{fil}$ =2000 °C and $T_{sub}$ = 300°C.......................................................................................................................................43

Fig. 8-3: Raman spectra of SiGe and Ge films deposited with different $T_{fil}$, $T_{sub}$ and gas mixtures...........................44

Fig. 8-4: The GID X-ray spectrum of the SiGe film deposited at $F_{Si2H6}$ = 3.4 sccm, $F_{GeH4}$ = 1.7 sccm, $F_{H2}$ = 7.0 sccm, p = 2.5 mTorr, $T_{sub}$ = 200 °C and $T_{fil}$ = 1800°C for 10 min with a film thickness of d = 141 nm. ......................45
Fig. 8-5: Raman and FTIR spectra of SiGe films deposited at $F_{Si2H6}$=3.4 sccm, $F_{GeH4}$=1.7 sccm, $F_{H2}$=7.0 sccm, p=3.1 mTorr, $T_{sub}$ = 200 °C and $T_{fil}$ = 1800°C for 15 min using filament Type S. ......................................................46
Fig. 9-1: Deposition rates of intrinsic a-Si:H film deposited under the conditions of RF power =25mW/cm$^2$ and $T_s$=150ºC. Square symbols represent $Si_2H_6$ series and diamond symbols represent $Si_3H_8$ series; The solid triangles represent the relationship between deposition rates and $R_a$=[H]/[Si] for $Si_3H_8$ series. .........................51
Fig. 9-2: Raman spectra of the series of sample deposited using $Si_3H_8$ (2a) and $Si_2H_6$ (2b). In Fig. 9-2a, curves from bottom to top are for Si:H deposited with R=143, 179, 213, and 286. In Fig. 9-2b, curves from bottom to top are for a-Si:H deposited with R=75; 100; 125; and 150. ......................................................................52
Fig. 9-3: Activation energy of a-Si:H films made using $Si_2H_6$ and $Si_3H_8$ as a function of hydrogen dilution R. ........53
Fig. 9-4: Microstructure factor R* as a function of hydrogen dilution R. ..................................................................54
Fig. 9-5: H content estimated from FTIR spectra as a function of $H_2$ dilution R. ......................................................55
Fig. 9-6: Photosensitivity of a-Si:H films deposited using $Si_2H_6$ and $Si_3H_8$ as a function of hydrogen dilution. ........55
Fig. 9-7: Open circuit voltage versus $H_2$ dilution for $Si_2H_6$ and $Si_3H_8$ devices..........................................................56
Fig.10-1: The Raman spectra taken from (a) the front side surface and (b)the back side of the p-layer through the glass substrate. ..........................................................................................................................................60
Fig. 10-2: a) and b) are HAADF and SAED images of the Sample A with a seed layer between the p-and i-layer; c) and d) are HAADF and NED images of the Sample B which has a slightly less Voc........................................61
Fig. 11-1: Raman spectra of the µc-Si:H p-layer (Curve a) and the nc-Si:H p-layer samples taken from the front surface (Curve b) and the back surface (Curve c) th...........................................................................................66
Fig. 11-2: TEM micrographs of a thin nc-Si:H p-layer of 30 nm thick with a hybrid, stacked structure. (a) HAADF image, where bright dots represent nanocrystalline particles; in the insert is a SAED image, showing the diffraction pattern with crystalline features; (b) HREM image, exhibiting the lattice image; (c) Nano electron diffraction (NED) taken from one of the bright dots indicating the crystalline nature of the particle. ................67
Fig. 11-3: I-V characteristics of n-i-p a-Si:H solar cells on SS coated with Al/ZnO using the nc-Si:H p-layer (Curve a) or µc-Si:H p-layer into the cell (Curve b )...........................................................................................67
Fig. 12-1: Schematic diagram of the modeled triple junction solar cell. ....................................................................70
Fig. 12-2: ASA generated I-V characteristics of the standard triple junction solar cell (Normal case) and cases designated in Table 1 as A1, A2, B1, B2, C1, C2, D1, D2, E1, E2, F1, and F2. ...............................................72
Fig. 13-1: Relationship between $V_{oc}$ and $I_{sc}$ of single junction top cell under intensity variation of different wavelength of monochromatic light. .........................................................................................................75
Fig. 13-2: Relationship between $V_{oc}$ and $I_{sc}$ of single junction bottom cell under intensity variation of different wavelength of monochromatic light. .........................................................................................................76
Fig. 13-3: Quantum efficiency curves of a tandem-junction a-Si/a-SiGe solar cell used in this study to illustrate the method. ...........................................................................................................................................76

Fig. 13-4: Relationship between $V_{oc}$ and $I_{sc}$ of top component cell in a tandem cell under variation of 400 nm light intensity. ....77
Fig. 13-5: Relationship between $V_{oc}$ and $I_{sc}$ of bottom component cell in a tandem cell under variation of 700 nm light intensity. ....77
Fig. 13-6: Variation of tandem cell current ($I_{tandem}$) with variation of intensity of red light as a function of detector voltage. ....78
Fig. 13-7: I-V characteristic of top component cell in a tandem-junction cell. ....79
Fig. 13-8: I-V characteristic of bottom component cell in a tandem-junction cell. ....80
Fig. 14-1: Transmission of glass encapsulated with EVA and Sylgard. ....81
Fig. 14-2: Silicone elastomer encapsulated a-SiGe based minimodules ....82
Fig. 15-1: A photo of UT's PECVD system before expansion. ....84
Fig. 15-2: A photo of UT's HWCVD chamber integrated to the multi-chamber PECVD system. ....85
Fig. 15-3: AutoCAD drawing of the PECVD/HWCVD system before recent expansion. ....86
Fig. 15-4: AutoCAD drawing of the multi-chamber deposition system with additional chambers (1 load lock and 3 sputtering chambers for Al, ZnO and ITO layers, as previously planned). ....86
Fig. 15-5: Photo of the entire system with nine chambers--3 PECVD, 1 HWCVD, 4 Sputtering, and 1 Load lock chambers. ....87

# List of Tables

Table 2-1: I-V performance of triple cell having heavily doped tunnel-junction interface layers with different thicknesses ... 6
Table 2-2: IV performance of top, middle and bottom component cells before and after 1000 hours of light soaking with 1 sun intensity at 50 $^oC$. ... 7
Table 2-3: IV performance for triple-junction a-Si based solar cells measured at UT and NREL. ... 9
Table 3-1: Deposition conditions and device performance for a series of a-SiGe solar cells having bandgap optimal for use in high-efficiency single-junction solar cells ... 13
Table 3-2: Performance of a-SiGe solar cells deposited using p-layers deposited at different temperature or different combination of temperatures ... 15
Table 4-1: Deposition conditions and J-V performance for a series of a-Si solar cells ... 17
Table 5-1: Performance of a SiGe:H n-i-p devices made with different H dilution $R_{H.}$ ... 25
Table 6-1: Single-junction a-Si solar cell devices fabricated to map out the deposition phase diagram in terms of substrate temperature and hydrogen dilution ... 29
Table 6-2: Thickness of the nip layers for the 42 samples fabricated to map out the phase diagram. The thickness shown is in nm. ... 29
Table 6-3: Growth rate, in A/s, of i-layers deposited under different conditions. ... 30
Table 6-4: Open circuit voltage of the 42 samples fabricated to map out the phase diagram. ... 30
Table 7-1: Deposition conditions of a-Si:H films using HWCVD. All samples were deposited at 100 mTorr with a filament temperature of 2000 °C. ... 36
Table 7-2: Properties of a-Si:H films deposited using HWCVD. ... 37
Table 8-1: The parameters of the coil-shaped filament used in this study ... 41
Table 9-1: Volume fraction of nanocrystalline silicon phase estimated from Raman spectra for two series of sample. Thicknesses of samples are also included in the Table. ... 52
Table 11-1: Gaussion deconvolution of the Raman spectra of Curve (b) and Curve (c) in Fig.1, including the peak position ($P_k$) and the peak area (A) of the TO modes for crystalline ($TO_c$), amorphous ($TO_a$) and interfacial ($TO_i$) inclusions. The volume crystalline fraction (C) is also listed. ... 65
Table 12-1: Description of different simulation cases for the triple junction solar cells studied in the present work. 70

# 1 Introduction

## 1.1 Background

This final report covers the research works on the Project "High Efficiency and High-Rate Deposited Amorphous Silicon-Based Solar Cells" at the University of Toledo for the Period of September 1, 2001 to March 06, 2005, under NREL Subcontract No. NDJ-2- 30630-08. The objectives of this project are (1) to establish a transferable knowledge and technology base for the fabrication of high-efficiency triple-junction a-Si-based solar cells and (2) to develop high-rate deposition techniques for the growth of a-Si-based and related alloys including poly-Si, μc-Si, a-SiGe and a-Si films and photovoltaic devices with these materials.

## 1.2 Technical Approach

The approaches toward the program objective include (1) developing a "grand phase diagram" of deposition conditions for the growth of protocrystalline Si and protocrystalline SiGe alloys and use these materials for the fabrication of top, middle, and bottom component cells of spectrum-splitting triple-junction solar cells; (2) exploring the deposition of a-Si-based materials using new chemical precursors including trisilane; (3) studying the impact of mismatch of band edges at the interfaces on the solar cell I-V characteristics and the physics of buffer layers; (4) combining these improvements made in component cells and fabricate triple cells with high stable, total-area efficiency; (5) developing a technique to measure component cell I-V performance in a two-terminal triple stack; (6) performing modeling on triple cells and compare the modeling results with the actual fabricated triple-cell devices; and (7) fabricating poly-Si, μc-Si, a-SiGe and a-Si at high rates using a hot-wire CVD process and depositing a-SiGe and a-Si at high rates using VHF plasma.

## 1.3 Accomplishments and Organization of the Final Report

Task 1: Grand phase diagram for deposition of protocrystalline Si and SiGe materials.

Under this task, we studied the phase diagram for a-Si deposition for different $H_2$ dilution ratio R and substrate temperature $T_s$. We found that the transition from amorphous to microcrystalline occurs with lower hydrogen dilution R at $T_s$ ~ 200 °C. At higher and lower $T_s$, higher R is needed to deposit microcrystalline Si films. The results are summarized in Chapter 6.

In order to be able to cover a broader parameter space within a limited time, we designed and installed a load lock chamber that allows us to load in simultaneously a set of ten 4"x4" masks with different patterns of coverage for the deposition. In this way, we could explore a large set of parameters in a single vacuum pump down. We have also studied the deposition of protocrystalline Si and SiGe using RF PECVD and HWCVD during this program period.

The p-layer materials which lead to high $V_{oc}$ a-Si solar cells have been analyzed by high resolution TEM. It is concluded that the p-layer that leads to high $V_{oc}$ contains nc-Si particles, about 2nm to 3nm in size, imbedded in a-Si matrix. It is further concluded that the mixed phase p-layer with a higher volume fraction of nc-Si:H phase, within the range studied, leads to a higher $V_{oc}$. The optimum p-layer material for nip-type a-Si:H solar cells is neither at the onset of the transition between amorphous to (amorphous and nanocrystalline) mixed phase nor a nanocrystalline/microcrystalline material with a high volume fraction of crystalline phase. Optical transmission measurements show that the *nc*-Si *p*-layer has a wide optical bandgap of 1.96 eV indicated by Tauc's plot, due to the quantum confinement effects (QCE). Using this kind of *p*-layer in *n-i-p a*-Si:H solar cells, the cell performances were improved with a $V_{oc}$ of 1.042 V, while the solar cell deposited under a similar condition but incorporating a hydrogenated microcrystalline silicon (*μc*-Si:H) *p*-layer leads to a $V_{oc}$ of 0.526 V. These results are summarized in Chapter 10 and Chapter 11.

Task 2: Deposition of a-Si based materials using new gas precursors

This task is performed together with Voltaix, Inc., which supplies trisilane gas for deposition of a-Si based materials. Trisilane gas cylinder has been produced and installed in UT's deposition system. We have carried out extensive system calibration so that a comparative study between trisilane and disilane can be performed. Detailed results on the trisilane study are reported in Chapter 9.

Task 3: Study of nanometer-sized doped layers and the band-edge mismatch at hetero-interfaces

Extensive research is carried out in this area. We studied extensively two interfaces: 1) the p-i interface and 2) the $p^+$-$n^+$ interface at the tunnel junctions. The study on p-i interface for a-Si and a-SiGe solar cells is reported in the 29th IEEE Photovoltaic Specialist Conference, held in May, 2002. The paper is not attached in this report but can be obtained from the Proceedings of IEEE PVSC. In summary, we found that the p-layer optimized for a-Si top cell causes severe J-V roll-over when it is used for narrow bandgap a-SiGe alloys. We conclude that the band mismatch at the p-i interface prevents holes from being collected at the p-layer under a forward bias near $V_{oc}$ point (when the field is weakened). This causes reduced carrier injection, and consequently the poor roll-over behavior in the J-V characteristics.

The study on the $p^+$-$n^+$ interface at the tunnel junction is summarized in Chapter 2.

As described in Chapter 15, we have completed the installation and optimization of a 5-chamber addition to UT's existing four-chamber PECVD/HWCVD systems. Four of the five chambers are used for the sputter deposition of metal (Al, Ag, etc), ZnO, ITO, $SiO_2$ layers and the fifth one is a new load-lock chamber capable of simultaneously loading 10 substrates, marks, or combinations of substrates and masks. This system allows us to complete the entire 12 layers of a triple-junction solar cell, Al/ZnO/nip/nip/nip/ITO in a single vacuum pump down, thus avoiding the undesirable air exposure at some of the critical interfaces. The ability to control the air exposure at these interfaces could lead us to understand and analyze the optical and electrical

losses at these interfaces such as ZnO/n and p-ITO interfaces. The deposition of back reflector layers (Al/ZnO and Ag/ZnO) and top conducting electrode (ITO) have been optimized. Triple-junction solar cells using this new 9-chamber deposition system have been fabricated on a routine basis The design and the process optimization of these five new chambers is supported by this NREL-funded project while the acquisition of components and the installation are supported by a complementary project funded by Air Force Research Lab.

### Task 4: Fabrication of triple-junction cells

Highlights of the accomplishment of this task include:

- Fabrication of a-SiGe single-junction solar cells with >12.5% initial, active-area efficiency.
- Fabrication of a-Si/a-SiGe tandem-junction solar cells with >12.5% initial, active-area efficiency.
- Fabrication of a-Si/a-SiGe/a-SiGe triple-junction solar cells with >12.5% initial, active-area efficiency.
- Fabrication of wide bandgap a-Si top cells with 11.1% initial efficiency.
- Fabrication of top cells with $V_{oc}$ = 1.023 V and FF = 0.78 using improved intrinsic and doped layers.

The details of the research on this task are summarized in Chapter 2, Chapter 3 and Chapter 4.

### Task 5: Technique for measuring component cell I-V in a two-terminal triple stack

The research activities in this area consist of two parts: 1) the experimental work has been mostly focused on two-junction, two-terminal device. The study was carried out using UT's quantum efficiency system. The component cell performance in a tandem structure was measured using various bias light conditions. Further systematic study is still needed to demonstrate satisfactory results; 2) In addition to the experimental work, we have established a procedure that is expected to allow us to measure the J-V of component cells in a triple-junction stack. Employments of a novel technique have been developed at UT to measure the component cell current-voltage characteristics in a multiple-junction stack. We also have demonstrated the I-V measurement of component cells in tandem-junction solar cells. This technique is described in Chapter 13.

### Task 6: Modeling of triple-junction cells with AMPS and comparison with fabricated devices.

We have performed modeling work in conjunction with the fabrication of triple cells. Modeling and simulation of triple junction a-Si solar cells have been studied by using the Advanced Semiconductor Analysis (ASA). The device performance is analyzed with numerically simulated I-V characteristics. We have studied several failure scenarios such as

variations in the thickness of different layers of the multilayered triple-junction structure. Distinctive features of the I-V characteristics and solar parameters have been found which have been correlated and discussed with the basis of device physics. This work is summarized in Chapter 12.

Task 7: High-rate deposition of a-Si based solar cells

Under this task area, we studied of the deposition of Si:H materials using HWCVD and VHF PECVD.

In the HWCVD area, We have conducted extensive research using a hot-wire CVD process with a coiled filament and multiple gas inlets. Two papers were presented in the 2nd International Conference on Cat-CVD. Using such a coiled filament, we deposited a-Si films at a deposition rate up to 240 Å/s. These films show a low microstrcture R* (around or less than 0.1). At low Ts and without H dilution, we deposited a-Si films at a rate up to 800 Å/s. We studied the effect of the Si:H growth on different filament geometry. We also studied SiGe:H materials with different Ge content in the film and the deposition of amorphous and nanocrystalline SiGe:H alloys using different amounts of hydrogen dilution. Some of the studies in this area are summarized in Chapter 7 and Chapter 8.

In the VHF PECVD area, new matching box was installed. The modification of hardware allows us to incorporate more power into the plasma and leads to higher deposition rate. Study of the deposition uniformity was also carried out. It was found that the film uniformity is the highest when the chamber pressure was kept near 0.35 Torr in our deposition system. Fabricated nc-Si based single-junction solar cells with >25% quantum efficiency in the 800-900nm range.

# 2 Triple-Junction a-Si Solar Cells with Heavily Doped Thin Interface Layers at the Tunnel Junctions

*Contributors: W. Wang, H. Povolny, W. Du, X.B. Liao and X. Deng*

**ABSTRACT**

Triple-junction a-Si based solar cells, having a structure of SS/Ag/ZnO/$n^+$/n/b/a-SiGe-i/b/p/$p^+$/$n^+$/n/b/a-SiGe-i/b/p/$p^+$/$n^+$/n/a-Si-i/p/$p^+$/ITO, are fabricated at the University of Toledo using a multi-chamber, load-locked PECVD system. We studied the effect of heavily doped $p^+$ and $n^+$ layers deposited at the tunnel junction interfaces between the top and middle component cells and between the middle and bottom component cells on the efficiency of triple-junction solar cells. Preliminary results show that thin, ~ 1nm, interface $p^+$/$n^+$ layers improve the solar cell efficiency while thicker interface layers, ~4nm thick, cause the efficiency to decrease. Incorporating the improved interface layers at the tunnel junctions, as well as earlier improvements in the intrinsic layers, the p-i interface in terms of reducing the band-edge offset, and the a-SiGe component cells using bandgap-graded buffer layers, we fabricated triple-junction solar cells with 12.71% efficiency in the initial state and 10.7% stable efficiency after 1000 hours of 1-sun light soaking. Samples sent to NREL for independent measurements show 11.8% total-area (or 12.5% active-area) initial efficiency.

## 2.1 INTRODUCTION

Triple-junction solar cell structure have been studied and used extensively to deposit high-efficiency a-Si based solar cells. Using a triple cell structure, United Solar Systems Corp. fabricated a-Si/a-SiGe/a-SiGe solar cells with 13% stabilized efficiency [1]. In such a triple-junction, two-terminal structure, the tunnel junction between the doped layers of neighboring component cells are formed due to the high concentration of recombination centers from the dangling bond defects in the doped a-Si materials. For this reason, the doped layers at the tunnel junctions are usually made thicker and/or with higher doping concentrations than those for single-junction solar cells [2]. However, a thicker doped layer would result in an optical loss and a higher doping concentration would result in a reduced bandgap, consequently, a lower Voc. In an earlier work [3], doping graded p-layer was studied in an n-i-p-n test structure. It was found that a p-layer with higher doping near the n-layer and lower doping near the i-layer leads to improved efficiency compared with a p-layer with constant doping [3]. In this work, we investigate the impact of inserting heavily doped thin interface layers at the tunnel junction to enhance the recombination of carriers from neighboring component cells.

## 2.2 EXPERIMENTAL

The structure of triple-junction a-Si based solar cell fabricated in this study is SS/Ag/ZnO/$n^+$/n/b/a-SiGe-i/b/p/$p^+$/$n^+$/n/b/a-SiGe-i/b/p/$p^+$/$n^+$/n/a-Si-i/p/$p^+$/ITO, where SS is

stainless steel foil substrate, $p^+$ and $n^+$ are heavily doped interface layers, and /b/ on both sides of a-SiGe i-layers are bandgap graded buffer layers. All of the semiconductor layers were deposited using University of Toledo (UT)'s multiple-chamber PECVD system. The substrate coated SS is provided by Energy Conversion Devices, Inc. (ECD) and United Solar. ITO is deposited at UT using rf sputtering from a ITO target in Ar ambient. The solar cells were characterized at UT using a Xe-lamp solar simulator and a quantum efficiency measurement system with optical and electrical bias capability, allowing us to measure the QE of component cells in a triple-junction two-terminal stack. Detailed description of the experimental details can be found in our earlier reports [4].

## 2.3 RESULTS AND DISCUSSIONS

### *2.3.1 Heavily doped $p^+$ and $n^+$ interface layer at the tunnel junctions*

Table 2-1 shows the I-V characteristics of a series of four triple-junction solar cells having a structure $SS/Ag/ZnO/n_1^+/n_1/b/a\text{-}SiGe\text{-}i_1/b/p_1/p_1^+/n_2^+/n_2/b/a\text{-}SiGe\text{-}i_2/b/p_2/p_2^+/n_3^+/n_3/a\text{-}Si\text{-}i_3/p_3/p_3^+/ITO$, where $p_1^+/n_2^+$ and $p_2^+/n_3^+$ interface layers are varied while all other layers are essentially kept unchanged for the set of devices. These heavily doped layers were deposited using a doping ratio of $BF_3:SiH_4=1.7:1$ for the $p^+$ layer and $PH_3: SiH_4=1:10$ for the $n^+$ layer. The deposition rates for the $p^+$ and $n^+$ layers are estimated to be 0.3 Å/s and 1 Å /s, respectively.

***Table 2-1: I-V performance of triple cell having heavily doped tunnel-junction interface layers with different thicknesses***

| $p^+$ and $n^+$ interface layer deposition time (s) | | Voc (V) | Jsc (mA/cm$^2$) | FF (%) | η (%) | Device Number |
|---|---|---|---|---|---|---|
| $p_1^+$ & $p_2^+$ | $n_2^+$ & $n_3^+$ | | | | | |
| 0 | 0 | 2.300 | 7.25 | 68.4 | 11.4 | GD846 |
| 10 | 10 | 2.314 | 7.54 | 69.2 | 12.1 | GD840 |
| 20 | 20 | 2.276 | 7.55 | 69.7 | 11.9 | GD842 |
| 40 | 40 | 2.222 | 7.02 | 66.3 | 10.4 | GD854 |

As we see from the Table, GD846 was fabricated without heavily doped interface layer and is used here as a reference sample. Compared with GD846, GD840 (made with 10 s $p^+/n^+$ layers) show an improvement in both the $J_{sc}$ and FF. More devices will be fabricated to confirm that there is indeed an improvement in the current when thin $p^+/n^+$ layers are inserted at the tunnel junctions. The loss of current in GD846, if further confirmed, would likely be due to an insufficient amount of recombination centers near the tunnel-junction interface, hindering photo-generated carriers from flowing to the tunnel junction to recombine. However, when thicker $p^+$ and $n^+$ layers, with 20 s or longer deposition time, are used, $V_{oc}$ drops significantly, from 2.31 V to 2.22 V. There are two possible reasons for this Voc drop. First, since the bandgap of a-Si decreases with increased doping, the effective bandgaps of the doped layers, $p/p^+$ and $n/n^+$, are reduced when the $p^+$ and $n^+$ layers are made thicker, resulting in a reduced built-in potential. Second, when the heavily doped layers are too thick, holes from $p_1$ ($p_2$) could fall into deep traps

in $p_1^+$ ($p_2^+$) while electrons from $n_2$ ($n_3$) could fall into deep traps in $n_2^+$ ($n_3^+$); and these traps could be 50 Å apart, as in the case of GD854. These trapped charges could form a reversed electrical field at the $p^+/n^+$ interface, reducing the total voltage of the triple cell. These trapped charges also generate potential barriers at the $p/p^+$ and $n/n^+$ interfaces, hindering the flow of carriers toward the $p^+/n^+$ interface, resulting in reduced current, as reflected in the $J_{sc}$ of GD854. The loss in FF in GD854 could have two contributions. First, it could be from these potential barriers indicated above. Second, the additional optical absorption by the thicker $p_2^+/n_3^+$ layers and $p_1^+/n_2^+$ would reduce the current of the middle and bottom component cells, respectively, causing the triple cell to be more limited in current, at the power point, by the middle or bottom cell which has poorer FF than the top component cell. This results in a drop in the overall triple-cell FF.

### *2.3.2 Fabrication of Triple-Junction a-Si Solar Cells*

Incorporating optimized $p^+/n^+$ layers at the tunnel junctions, as well as other recent improvements related to our triple-cell fabrication including: a) an improved intrinsic a-Si:H top cell i-layer made at low temperature and very high hydrogen dilution (see IV performance data of component cells in Table 2-2); b) improved a-SiGe component cells using bandgap graded buffer layers [5] (See IV data in Table 2-2) ; c) optimized nanocrystalline p-layer deposition conditions to reduce the band-edge offset at the p-i interfaces for component cells with different i-layer bandgaps [6]; and d) a careful analysis of the light spectrum of our solar simulator and improved the current matching among component cells, we achieved the fabrication of a-Si/a-SiGe/a-SiGe triple cells with 12.7% initial efficiency. Fig. 2-1 shows the IV curve of the 12.7% triple cell, GD585. The performance for the triple cell is $V_{oc}$=2.29V, $J_{sc}$=8.34 mA/cm$^2$, FF=66.5% and the initial efficiency is 12.7%.

***Table 2-2: IV performance of top, middle and bottom component cells before and after 1000 hours of light soaking with 1 sun intensity at 50 °C.***

| Cell Number | Cell Type | Subs | | Voc (V) | Jsc (mA/cm$^2$) | FF (%) | η (%) | Degradation (%) |
|---|---|---|---|---|---|---|---|---|
| Gd550-1 | Top | SS | Initial | 1.00 | 9.49 | 71.61 | 6.77 | |
| | | | Stable | 0.98 | 9.20 | 66.66 | 6.01 | 11.23 |
| Gd572-2 | Middle | BR | Initial | 0.80 | 18.95 | 65.51 | 9.97 | |
| | | | Stable | 0.78 | 19.63 | 54.14 | 8.29 | 16.85 |
| Gd575-2 | Bottom | BR | Initial | 0.62 | 22.85 | 60.96 | 8.57 | |
| | | | Stable | 0.62 | 22.94 | 52.44 | 7.41 | 13.54 |

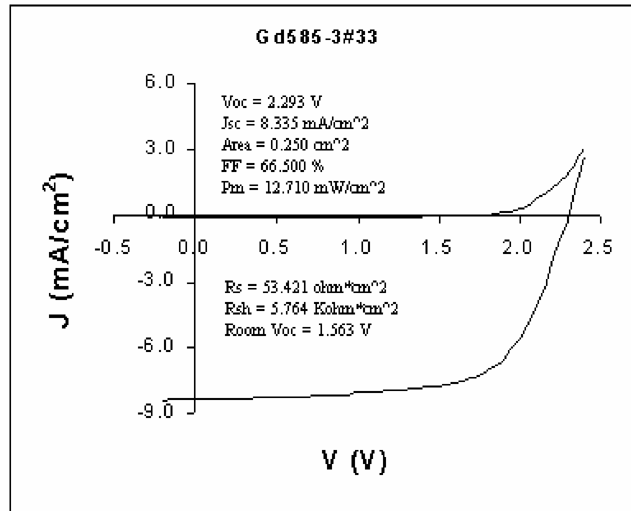


***Fig. 2-1: IV curve of a UT fabricated triple cell, showing 12.7% initial, active-area efficiency.***

Fig. 2-2 shows the quantum efficiency curves of the component cells in this triple cell. At the top of Fig. 2-2, we show the calculated short circuit currents of the component cells under both UT simulator and the AM1.5 global spectrum. Since the Xenon lamp spectrum does not match exactly the AM1.5 global spectrum, different short circuit currents were obtained when being calculated using different spectrums. It should also be pointed out that the top cell current was calculated with wavelength longer than 370 nm. Therefore, the actual current should be larger than the current of shown in the figure for top cell by about 0.3 mA/cm$^2$ in according to our estimations.

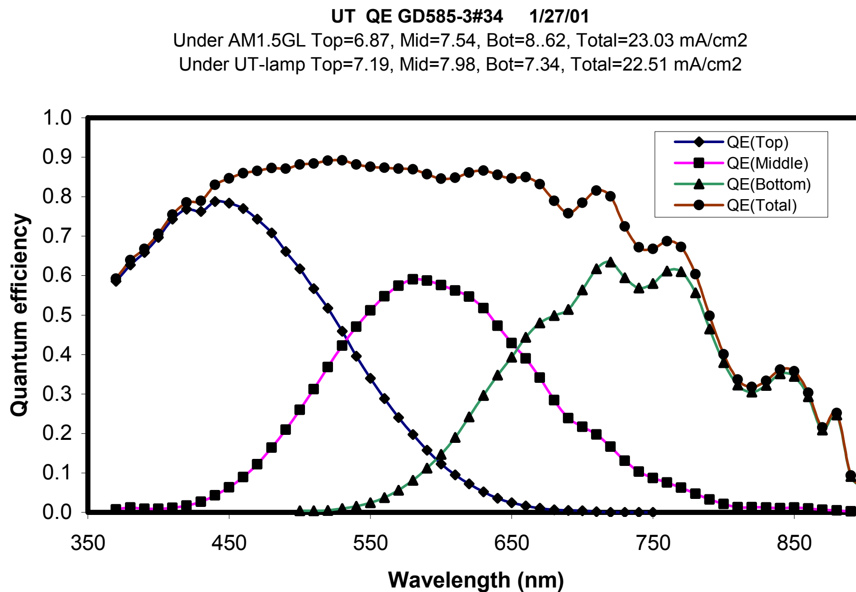


***Fig. 2-2: Quantum efficiency curve of 12.7% cell (GD585) showing the QE for top, middle and bottom cells. The figure also shows the short circuit current under UT simulator and AM1.5 spectrum.***

Some triple cells fabricated at UT were sent to NREL for independent measurements. Table 2-3 shows the measurement for GD585 measured at NREL and UT, which agree with each other very well. The small difference in the $J_{sc}$ and FF is because UT's simulator is slightly insufficient in the red, leading to a lower FF and a higher $J_{sc}$ for a triple cell limited in the current by the top cell. The total-area η measured by NREL for GD585-3#33 is 11.8% (12.55% active-area), as shown in Fig. 2-3.

***Table 2-3: IV performance for triple-junction a-Si based solar cells measured at UT and NREL.***

| Cell# | $V_{oc}$ (V) | $I_{sc}$ (mA) | FF (%) | Active area ($cm^2$) | Active -area η (%) | Total area ($cm^2$) | Total-area η (%) | Measur em't Lab |
|---|---|---|---|---|---|---|---|---|
| UT585-3#33 | 2.293 | 2.084 | 66.50 | 0.25 | 12.71 | | | UT |
| UT585-3#22 | 2.286 | 2.046 | 66.35 | 0.25 | 12.41 | | | UT |
| UT 585-3#33 | 2.3234 | 2.0591 | 67.17 | 0.256 | 12.55 | 0.272 | 11.81 | NREL |
| UT 585-3#22 | 2.3191 | 2.0331 | 66.14 | 0.255 | 12.41 | 0.271 | 11.68 | NREL |

We have conducted light soaking stability tests for these UT fabricated triple-junction solar cells. After 1000 hours of one-sun light soaking at 50 °C, these triple cells degrade around 11-12% and show stable active-area efficiency above 10.5% with the highest stable efficiency (active area) at 10.7%, shown in Fig. 2-4. The achievement of 10.7% stable efficiency is a significant improvement from our previously fabricated triple junction solar cells.

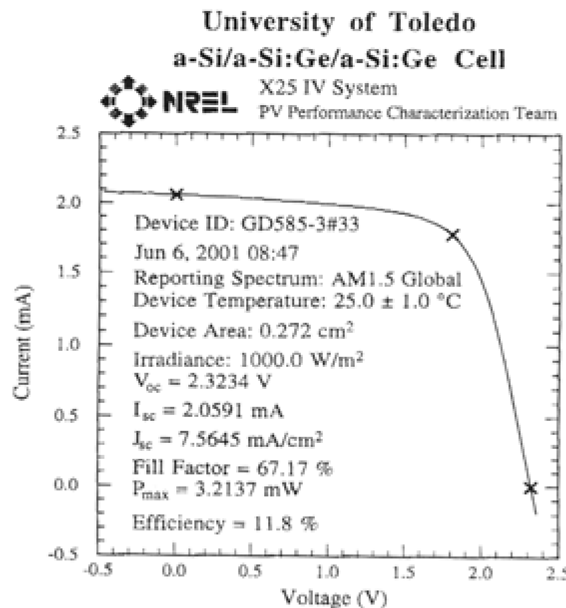


***Fig. 2-3: IV curve of GD585 measured at NREL, showing 11.8% initial, total-area efficiency.***

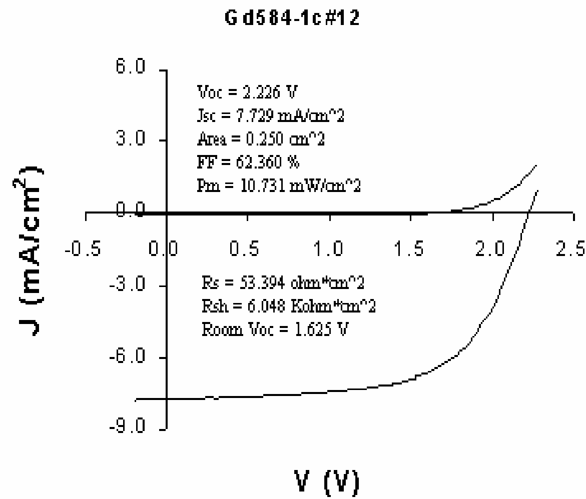


***Fig. 2-4: I-V curve of a triple cell showing 10.7% stable efficiency***

## 2.4 SUMMARY

The effect of heavily doped $p^+/n^+$ interface layers at the tunnel junction of triple-junction solar cells is studied. Preliminary results show that heavily doped thin interface layers could enhance the $J_{sc}$ and FF of the triple cell. However, thicker interface layers (~4 nm or thicker) could result in significant reduction in Voc, Jsc and FF, possibly due to the formation of reversed electrical field at the tunnel junction and electrical potential barriers inside the doped layers.

Incorporating improved component cells and tunnel junctions into triple cell fabrication, we achieved triple-junction a-Si/a-SiGe/a-SiGe solar cells with 12.7% initial active-area efficiency. NREL measurements for these cells show 11.8% initial total-area efficiency (12.55% active-area efficiency). After 1000 hours of light soaking, these triple cells stabilized at efficiencies of 10.5-10.7%, with a degradation of 11-12%.

## REFERENCES


1. J. Yang, A. Banerjee, and S. Guha, Appl. Phys. Lett. 70 2975 (1997).
2. A. Banerjee, J. Yang, T. Glatfelter, K. Hoffman and S. Guha, Appl. Phys. Lett. 64, 1517 (1994).
3. X. Deng, NREL Phase I Annual Subcontract Report, NREL/TP-411-20687, pp65-74. Available NTIS: Order No. DE9696000530 (Feb. 1996).
4. X. Deng, AIP Conf. Proc. 462, NCPV Photovoltaics Program Review, p.297 (1998).
5. X.B. Liao, J. Walker, and X. Deng, MRS Symp. Proc. 557, 779 (1999).
6. X.B. Liao, W. Wang, and X. Deng, this Proceeding.

# 3 High-Efficiency Single-junction a-SiGe Solar Cells

*Contributors: W. Du, X. Yang, H. Povolny and X. Deng*


## ABSTRACT

Single-junction a-SiGe solar cells were fabricated using plasma enhanced chemical vapor deposition on stainless steel substrate coated with Ag/ZnO back-reflector. Incorporating 1) an optimized a-SiGe i-layer with thickness and bandgap more suitable for single-junction cell, and 2) a hybrid p-layer with the sub-layer near a-SiGe i-layer deposited at a relatively high temperature for an optimal p-i interface and the bulk of the p-layer deposited at a relatively lower temperature for a better transparency, we achieved single-junction a-SiGe solar cells with initial, active-area efficiency greater than 12.5% and stable, active-area efficiency of 10.4%. Such high efficiency single-junction solar cells have important applications since they have initial and stabilized efficiencies approaching those usually obtainable with a multiple-junction structure, yet can be fabricated using a much simpler deposition process.


## 3.1 INTRODUCTION

We have previously reported our optimization of medium bandgap a-SiGe solar cell for use as the middle component cell of a triple-junction solar cell. In order to fabricate high efficiency single-junction solar cell which is simpler to manufacture, an ideal bandgap is close to that of the middle cell but not necessary the same. In this work, we investigated medium bandgap a-SiGe solar cell toward achieving single-junction solar cells with highest stable efficiency.

In our earlier work, we also reported the stability test of single-junction a-SiGe devices with different Ge in the i-layer. It was surprising to find a-SiGe cells with small amount of Ge in the i-layer were more stable than a-Si cell without Ge in the i-layer after light soaking. It is for this reason, we expect to fabricate single-junction a-SiGe cells with higher stabilized efficiency than single-junction a-Si cells.

In terms of p-layer fabrication, we reported previously that high performance wide bandgap single-junction a-Si solar cells ($V_{oc}$=1.014V and FF=74.6%) were obtained using p-layer deposited near the transition region between nanocrystalline silicon (nc-Si) and a-Si at a low temperate (Ts = 70 C). However, when such a p-layer, ideal for wide bandgap a-Si top cell, is used for narrow bandgap a-SiGe bottom cell in a multiple-junction solar cell, severe roll-over occurs in the J-V curve, possibly due to a mismatch at the p-i interface. It was further discovered that p-layer deposited at a higher Ts (140 C) forms a good interface with NBG a-SiGe i-layer and leads to ideal J-V curve [1]. The diode characteristics are even better than that of top cell. However, this p-layer, p ($T_s$=140C), is less transparent than p ($T_s$=70C). Although it is acceptable for use in middle and bottom component cell in a triple stack, it is not acceptable for use as the window layer in any single-junction solar cell.

## 3.2 APPROACH

Intrinsic Layer Optimization

We start with a-SiGe medium bandgap cell used as the middle cell inside a triple-junction stack and adjust the bandgap (i.e., Si:Ge ratio) and the thickness while maintaining the hydrogen dilution to be near the transition region from amorphous to microcrystalline.

Doped Layer Optimization

To obtain a p-layer that forms good interface with a-SiGe and is more transparent as the window layer, we explored the use of a hybrid, stacked p-layer with sublayers deposited at $T_s$=140°C and 70°C [2], as depicted in Fig. 3-1.

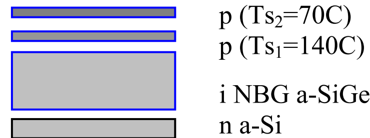


***Fig. 3-1: Schematic of the device showing the p-layer with sublayers deposited at different temperature.***

## 3.3 EXPERIMENTAL

The structure of single-junction a-SiGe solar cell fabricated in this study is SS/Ag/ZnO/$n^+$/n/b/a-SiGe-i/b/p/$p^+$/ITO, where SS is stainless steel foil substrate, $p^+$ and $n^+$ are heavily doped interface layers, and /b/ on both sides of a-SiGe i-layers are bandgap graded buffer layers. All of the semiconductor layers were deposited using University of Toledo (UT)'s multiple-chamber PECVD system. The substrate coated SS is provided by Energy Conversion Devices, Inc. (ECD) and United Solar. ITO is deposited at UT using rf sputtering from a ITO target in Ar ambient. The solar cells were characterized at UT using a Xe-lamp solar simulator and a quantum efficiency measurement system Detailed description of the experimental details can be found in our earlier reports [3].

Thickness of the nip cells were measured using reflection measurement from interference peaks of the actual device. Therefore, the thickness used here is the combined thickness of n,i,p layers rather than that of the i-layer.

## 3.4 RESULTS

### *3.4.1 Optimization of the i-layer*

Table 3-1 shows the results of a series of a-SiGe solar cells having a structure of SS/$n^+$/n/b/a-SiGe-i/b/p/$p^+$/ ITO (for GD830, GD895, GD896, GD897) or SS/Ag/ZnO/$n^+$/n/b/a-SiGe-i/b/p/$p^+$/ ITO (for GD905). GD895 is deposited under our standard middle cell condition,

used for the fabrication of triple cells with 12.7% initial efficiency. Device GD895, 896, 897 incorporate increasingly more $Si_2H_6$ in the gas mixture, results in increasingly higher bandgap. The i-layer of device GD897 is deposited in 40 min while the rest of the devices in 60 min. It is expected we see increasingly higher Voc when $Si_2H_6$ is increased, the higher $J_{sc}$ is due to the increased i-layer thickness. In the table, the thickness of nip was calculated from interference fringes in the reflection spectra. There is no obvious drop in the FF, at least in the initial state, when the i-layer is made with more $Si_2H_6$ (less Ge and thicker).

Sample GD905 was made with a bandgap-graded a-SiGe i-layer so that the bandgap near the p-layer is smaller. In this way, more light is absorbed near the p-layer so that holes has less distance to travel to the p-layer and get collected. However, there is a significant drop in the open circuit voltage, which seems to be governed by the narrowest point in the i-layer bandgap, rather than the average bandgap. Sample GD905 shows higher efficiency since it is deposited on back-reflector. The thickness of GD905 is not provided since it is deposited on a texture back reflector which prevents us from using interference fringes to calculate the thickness.

***Table 3-1: Deposition conditions and device performance for a series of a-SiGe solar cells having bandgap optimal for use in high-efficiency single-junction solar cells***

| sample | $Si_2H_6$ | $GeH_4$ | $H_2$ | Time | d of nip | $V_{oc}$ | $J_{sc}$ | FF | Eff | Substrate |
|---|---|---|---|---|---|---|---|---|---|---|
| No | (sccm) | (sccm) | (sccm) | (min) | (nm) | (V) | (mA/cm2) | (%) | (%) | |
| gd830 | 1.5 | 2.75 | 100 | 60 | 323 | 0.830 | 14.2 | 70.2 | 8.7 | SS |
| gd895 | 2 | 2.75 | 100 | 60 | 271 | 0.861 | 15.6 | 70.8 | 9.5 | SS |
| gd896 | 2.5 | 2.75 | 100 | 60 | 382 | 0.873 | 16.0 | 69.4 | 9.7 | SS |
| gd897 | 3 | 2.75 | 100 | 40 | 300 | 0.886 | 14.2 | 72.7 | 9.1 | SS |
| gd905 | 2 | 1.8-3.8 | 100 | 60 | | 0.833 | 20.7 | 68.1 | 11.8 | BR |

Since GD895 shows the highest FF, in addition to higher Voc and Jsc, it is selected for use as the standard i-layer deposition condition for single-junction a-SiGe cells.

We performed light soaking stability test. The light soaking was done using metal halide lamp with 100 mW/cm$^2$ light intensity. The samples are maintained at a temperature near 50C. Fig. 3-2 shows the J-V curve of one cell in GD904, deposited under the same conditions as GD895, but on Ag/ZnO back reflector. The initial cell efficiency is 12.1%. After 100 and 3300 hours of light soaking, the stabilized efficiency is 10.5%. <u>This is, to the best of our knowledge, highest reported stabilized efficiency for a single-junction a-Si based solar cell</u>.

### *3.4.2 Optimization of the p-layer*

Using the i-layer for GD895 (or GD904 which has the same i-layer), we fabricate a serious of a-SiGe single-junction solar cells with different p-layers. Boron doped layers, deposited at different temperatures, are used for the window layer. In Table 3-2, we present a serious of

devices with p-layer deposited at: 1) only 140 C, which is the temperature for all samples shown in Table 3-1; 2) only 70 C, which is the ideal temperature for p-layer used in our high-efficiency top cells, 3) both 140 C (for time t1) and 70 C (for time t2). Again, GD904 is the standard condition as a reference. It is found that the device (GD919) with p-layer deposited at a higher temperature for a relative short time ($t_1$=1min) and a lower temperature for a relatively longer time ($t_2$=2min) forms a good interface with the narrow bandgap a-SiGe layer, as reflected in the high FF, and is more transparent, as reflected in the high Jsc.

Fig. 3-3 shows the J-V curve of one cell in GD919 showing an initial, active-area efficiency of 12.8% (Voc=0.843 V, FF=0.727 and Jsc=21.3 mA/cm$^2$). We think the current density might be slightly overestimated by a few percent according to quantum efficiency measured. We performed light soaking test for these cells for these samples. After 100 hours of light soaking, these samples with double p-layer show 10.4% stable efficiency. More light soaking test is to be performed. We believe that the improved Jsc due to the p-layer should not alter the light soaking stability.

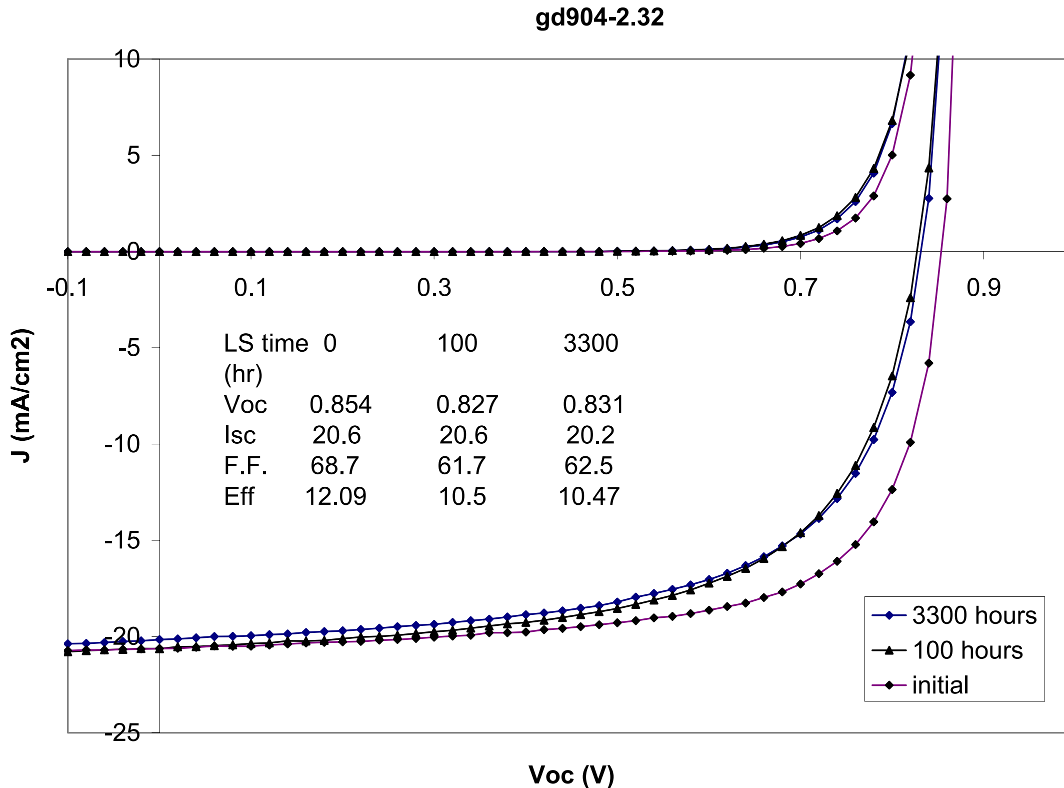


***Fig. 3-2: J-V curves of a-SiGe cell (GD904-2.32) measured before and after light soaking for 100 and 3300 hours, showing 10.47% stable, active-area efficiency.***

*Table 3-2: Performance of a-SiGe solar cells deposited using p-layers deposited at different temperature or different combination of temperatures*

| Sample | $t_1$ (min) | $t_2$ (min) | Voc | Jsc | FF | η |
|---|---|---|---|---|---|---|
| No | 140C | 70C | (V) | (mA/cm2) | (%) | (%) |
| GD904 | 3 | 0 | 0.856 | 20.6 | 68.6 | 12.1 |
| GD907 | 0 | 3 | 0.856 | 20.7 | 65.9 | 11.7 |
| GD908 | 0.5 | 2 | 0.858 | 21.0 | 66.9 | 12.1 |
| GD919 | 1 | 2 | 0.847 | 21.5 | 70.1 | 12.8 |

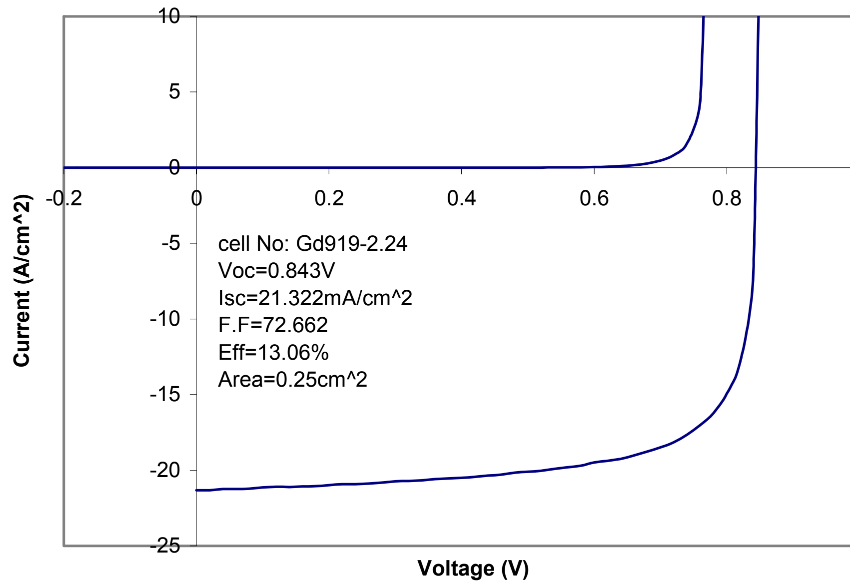


*Fig. 3-3: J-V curve of a single-junction a-SiGe solar cell with initial, active-area efficiency of around 13%.*

## 3.5 SUMMARY

High-efficiency single-junction a-SiGe solar cells are obtained using 1) improve a-SiGe i-layer and 2) a p-layer deposited with two separate steps: with one at a higher temperature for better interface with a-SiGe i-layer and the other at a lower temperature for better transmission. We achieved a-SiGe single-junction cells with greater than 12.5% initial, active-area efficiency and 10.4% stabilized efficiency.

## REFERENCES


1. X. Liao, W. Wang, and X. Deng, Proc. of 29th IEEE PVSC, 1234 (2001).
2. X. Liao et al, to be submitted to Proc. of 3rd WCPEC (2003).
3. W. Wang, H. Povolny, W. Du, X. Liao and X. Deng, Proc. of 29th IEEE PVSC, 1082 (2001).

# 4 Optimization of High-efficiency a-Si Top Cell

*Contributors: W. Du, X. Yang and X. Deng*

## 4.1 Introduction

In this study, we optimize the deposition of a-Si cell for use as top component cell inside a triple-junction stack. In addition, we optimize the solar cell for use as a single-junction a-Si solar cell without any Ge in the i-layer. Third, we explore the possibility of improving the p-layer using a double-p-layer deposited at different temperatures, which lead to significant improvement in the performance of medium bandgap a-SiGe cells.

## 4.2 Experimental

Amorphous Si solar cells having a structure of SS/Ag/ZnO/$n^+$/n/a-Si-i/p/$p^+$/ITO or SS/$n^+$/n/a-Si-i/p/$p^+$/ITO are deposited using a PECVD system with all three types of layers deposited in separated PECVD chambers. The p-layers are deposited in two different steps at different temperatures for some of the samples.

## 4.3 Results

Table 4-1 shows the performance for a series of a-Si cells deposited with different $Si_2H_6$ and $H_2$ flows and different i-layer deposition times. In addition, two samples, GD909 and GD912 are deposited with a p-layer deposited in two steps.

***Table 4-1: Deposition conditions and J-V performance for a series of a-Si solar cells***

| Sample No. | $Si_2H_6$ | $H_2$ | t(i-layer) (min) | t (p-layer) (min) 140C/70C | $V_{oc}$ (V) | $J_{sc}$ ($mA/cm^2$) | FF (%) | Eff (%) | Substrate |
|---|---|---|---|---|---|---|---|---|---|
| gd909 | 1 | 100 | 60 | 1/2 | 0.988 | 13.2 | 72.0 | 9.36 | Ag/ZnO |
| gd921 | 1 | 100 | 60 | 0/4 | 0.986 | 9.2 | 71.2 | 6.48 | SS |
| gd915 | 1 | 100 | 120 | 0/4 | 0.982 | 11.3 | 66.7 | 7.62 | SS |
| gd910 | 2 | 100 | 60 | 0/4 | 0.961 | 11.9 | 69.5 | 7.98 | SS |
| gd911 | 2 | 100 | 40 | 0/3 | 0.949 | 10.9 | 71.2 | 7.37 | SS |
| gd912 | 1.5 | 100 | 60 | 1/3 | 0.968 | 11.0 | 71.1 | 7.58 | SS |
| gd914 | 1 | 75 | 120 | 0/4 | 0.982 | 17.4 | 65.3 | 11.15 | Ag/ZnO |
| gd917 | 1 | 100-50 | 60 | 0/3 | 0.957 | 11.8 | 64.5 | 7.26 | SS |

From Table 4-1, we observe the following:

- Comparing GD921 and GD915, thicker i-layer leads to higher Jsc and lower FF, while Voc is unchanged.
- Comparing GD915 and GD910, less dilution and short time leads to device with higher FF.
- Two-step p-layer does not show improvement for the top cell.
- Sample deposited with a graded hydrogen dilution, with intent to keep the structure of a-Si on the amorphous side without becoming microcrystalline, does not show any improvement. This is puzzling and should be repeated in the future.
- Sample with intermediate H dilution ($H_2/Si_2H_6$=100/1.5) exhibit highest initial efficiency.

Fig. 4-1 shows the J-V curve of GD912, showing 11.1% initial efficiency. We have later further improve the fabrication process such as the ITO layers. This results in a further improvement in the cell performance. Fig. 4-2 shows an improved cell, ideal for use as a top component cell, showing 1.023 V open circuit voltage and 78% fill factor.

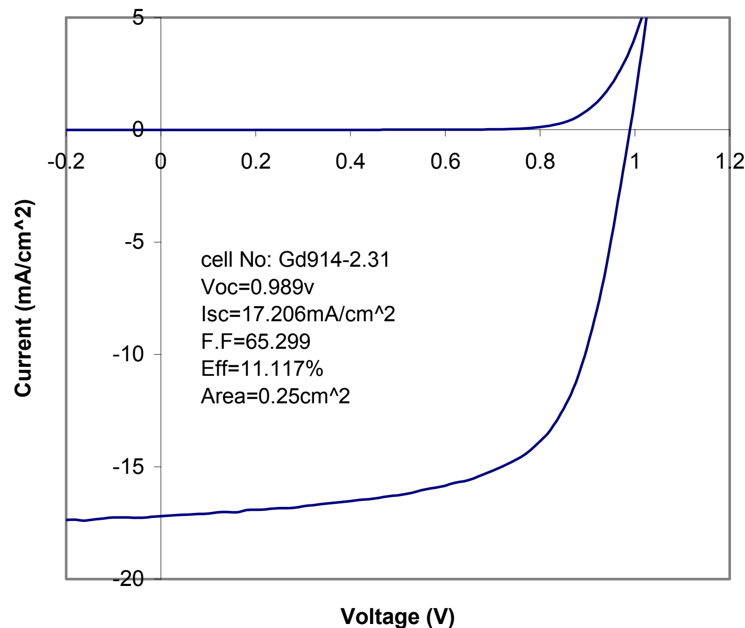


***Fig. 4-1: An optimized top cell deposited on Ag/ZnO back reflector, showing 11.1% initial, active-area efficiency.***

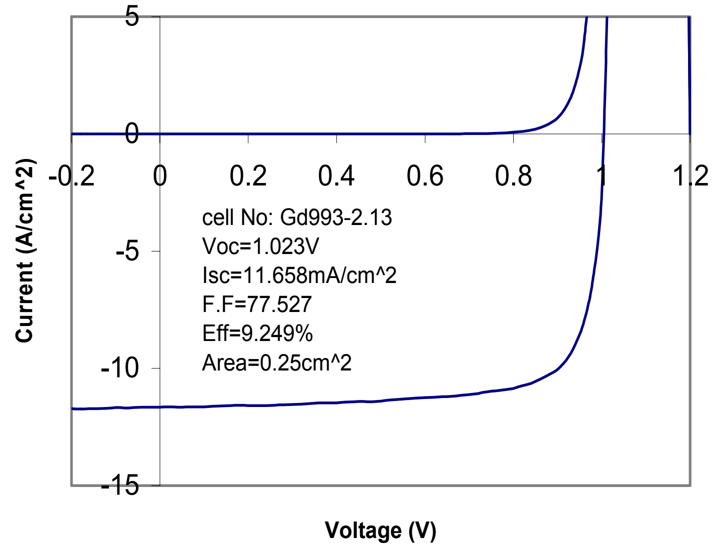


***Fig. 4-2: J-V curve of an improved a-Si solar cell showing 1.023 V open circuit voltage and 78% fill factor. The current is such that it is ideal for use as the top cell of a triple cell.***

## 4.4 Summary

We optimized a-Si solar cell i-layer and p-layer and obtained improved top cell:

- Wide bandgap a-Si top cell with 11.1% initial efficiency
- Wide bandgap a-Si top cell with 1.023V $V_{oc}$ and 78% FF

# 5 Raman and IR study of narrow bandgap a-SiGe and μc-SiGe films deposited using different hydrogen dilution

*Contributors: X. Liao, W. Wang and X. Deng*

**Summary**

Hydrogenated amorphous silicon-germanium (a-SiGe:H) films and n-i-p solar cells near the threshold of microcrystalline formation have been prepared by plasma enhanced chemical vapor deposition (PECVD) with a fixed germane to disilane ratio of 0.72 and a wide range of hydrogen dilution $R_H$=($H_2$ flow)/($GeH_4$+$Si_2H_6$ flow) values of 1.7, 10, 30, 50, 120, 180 and 240. The effects of $R_H$ on the structural properties of the films were investigated using Raman scattering and Fourier transform infrared (FTIR) absorption spectroscopy. It is found that H dilution causes the H content, especially that in $SiH_2$ configuration, in a-SiGe:H films to decrease and finally leads the films through amorphous to microcrystalline transition. The onset of the phase transition occurs at $R_H$ about 180, and the crystalline formation begins first in the Si-rich region. Light soaking tests on the solar cells demonstrate that the devices with higher $R_H$ exhibit higher stabilized efficiency after 1000 hours of 1 sun light soaking.

## 5.1 Introduction

Narrow band gap a-SiGe:H alloy has attracted a great deal of attention for application in the tandem and triple-junction solar cells, because its optical band gap can be tailored by changing the Ge content to match longer wavelengths of the solar spectrum. However, as the Ge content increases and the bandgap decreases, the electronic and structural properties of the films tend to be inferior. Although in recent years the defect density in a-SiGe:H films has been much suppressed by e.g. H-dilution [1], cathode deposition [2], and using disilane-germane mixture without H dilution [3] in PECVD process, the further improvement in the film quality has been a challenging issue in the research and development of a-Si:H based solar cells. In the previous reports we performed a systematic investigation of the effects of Ge content [4] and H dilution [5] on the electrical and optical properties of a-SiGe:H films. In this paper we report the impact of H dilution on the structural properties of a-SiGe:H films and n-i-p solar cells near and above the threshold of crystallinity.

## 5.2 Experimental

The a-SiGe:H films, approximately 0.5 μm thick, were deposited on 7059 glass, crystalline silicon (c-Si) wafer and stainless steel (SS) substrates using rf (13.56 MHz) PECVD in a ultrahigh-vacuum, multi-chamber, load-locked deposition system. A gas mixture of disilane, germane and hydrogen was used with a fixed germane to disilane ratio of 0.72 and a varying hydrogen dilution ratio $R_H$ of 1.7, 10, 30, 50, 120, 180 and 240, which is defined as the ratio of gas flows of [$H_2$] to [$Si_2H_6$] + [$GeH_4$]. The germane to disilane ratio is the same as what we

typically use for the i-layer in the narrow-bandgap bottom cell of our standard triple-junction solar cells [6]. FTIR absorption measurements were taken for samples on c-Si substrates to obtain information on the H content and bondings. In order to analyze the structural properties, Raman scattering spectra were recorded from the films on 7059 glass and n-i-p cell devices on stainless steel, upon the excitation of an argon laser with 488nm wavelength.

Single junction n-i-p solar cells using these a-SiGe materials as the i-layers were deposited on SS substrates without the use of a back-reflector. I-V measurements were taken under a Xe-lamp solar simulator under AM1.5 spectrum. Light soaking was performed under one-sun light intensity using a metal halide lamp. The light intensity is maintained at such a level that a reference Si solar cell generates the same current as it does under a Xe-lamp simulator.

## 5.3 Results and Discussions

### *5.3.1 FTIR absorption spectra*

The FTIR absorption spectra of seven a-SiGe:H samples are plotted in figures 1(a) and 1(b) with a varying H-dilution $R_H$ = 1.7 (GD419), 10 (GD420), 30 (GD422), 50 (GD423), 120 (GD424), 180 (GD449) and 240 (GD450), respectively. The arrangement of the spectra in these figures is in the sequence from top to bottom with $R_H$ increasing.

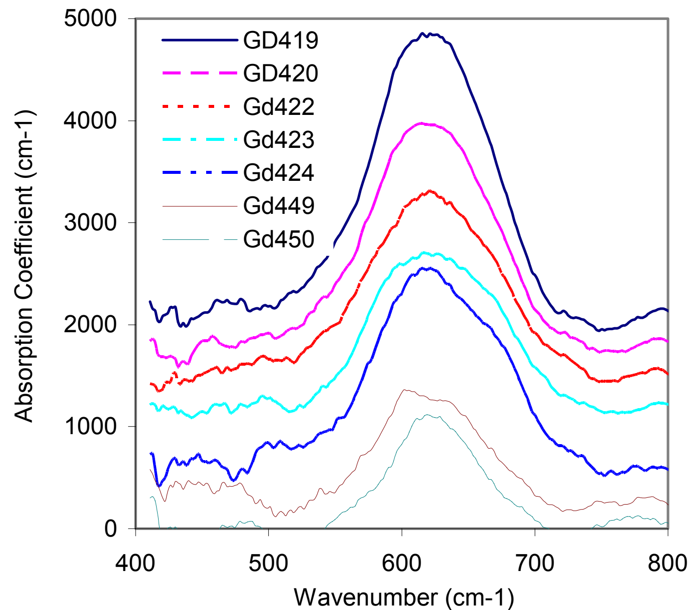


***Fig. 5-1(a): FTIR absorption spectra of a-SiGe:H films in the range from 400 to 800 cm$^{-1}$. The IR spectra were taken from the samples deposited under H-dilution $R_H$ = 1.7 (GD419), 10 (GD420), 30 (GD422), 50 (GD423), 120 (GD424), 180 (GD449) and 240 (GD450), respectively***

Fig. 5-1(a) shows the IR spectra ranging from 400 to 800 $cm^{-1}$. It is seen from this figure that a prominent peak appears at about 560-640 $cm^{-1}$ region, which is assigned to the bending vibration of Si-H and Ge-H bonds. As $R_H$ decreases from 1.7 to 240, the peak intensity is monotonically decreased, indicating that the hydrogen content ($C_H$) in the films descends with increasing H dilution, while its peak position is not obviously affected. However this peak position has a small red shift, due to the existence of Ge-H bonds in the a-SiGe:H films, in respect to the bending mode of Si-H bonds in a-Si:H at 640 $cm^{-1}$. This is similar to the earlier results in the literature [7], that reported the wagging or rocking modes of Si-H bonds gradually shifting from 640 $cm^{-1}$ to 560 $cm^{-1}$, as the Ge relative content increased from 0 to 1.

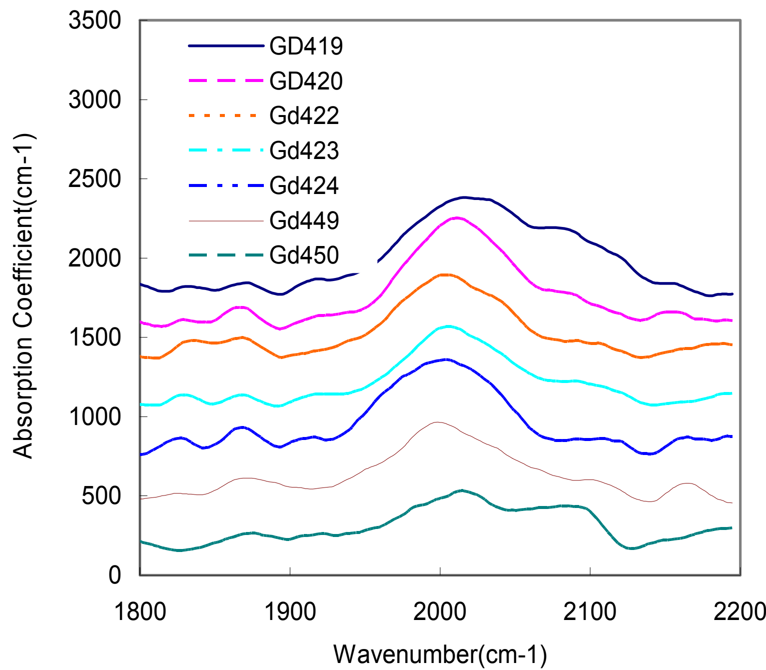


***Fig. 5-1(b): FTIR absorption spectra of a-SiGe:H films in the range from 1800 to 2200 $cm^{-1}$ . The IR spectra were taken from the same samples as in Fig. 5-1(a).***

Fig. 5-1(b) shows the IR spectra ranging from 1800 to 2200 $cm^{-1}$. It is seen that a few absorption features appear at about 2090, 2000 and 1872 $cm^{-1}$, which are respectively assigned to stretching vibrations of $SiH_2$, SiH and GeH configurations.

It is interesting to note the impact of $R_H$ on the relative intensity of the stretching mode at 2090 $cm^{-1}$, $I_{2090}$, which is defined as the ratio of its intensity to that of the peak at 2000 $cm^{-1}$. As $R_H$ increasing from 1.7 to 120, the relative intensity $I_{2090}$ becomes weaker. This suggests that the relative concentration of $SiH_2$ configuration in a-SiGe:H films decreases with $R_H$ increasing. But as $R_H$ further increasing from 120 to 240, the relative intensity $I_{2090}$ starts to increase. The dependence of $I_{2090}$ on $R_H$ could be seen more clearly in Fig. 5-2. This enhancement of $I_{2090}$ at higher $R_H$ is likely correlated with the formation of the microcrystalline phase in the films. We assigned it to $H_2$* complexes in the boundaries between microcrystallites [8].

The influences of H-dilution on the hydrogen content $C_H$ is also illustrated in Fig. 5-2, which was derived from the IR absorption coefficient of the Si-H bending mode in Fig. 5-1(a). It

shows that $C_H$ decreases as $R_H$ increases, except one point corresponding to the phase transition region $R_H$=120, where an anomalous increase in $C_H$ was found. This is similar to the observation in a-Si:H when deposited under high H-dilution to the phase transition region [9].

### *5.3.2 Raman spectra*

To clarify the structural variation we performed Raman spectroscopy measurements on the three highest diluted samples. Fig. 5-3 shows the Raman spectra taken from the front surface of the a-SiGe:H samples deposited on 7059 glass under $R_H$=120 (GD424), 180 (GD449) and 240 (GD450), respectively. For comparison the Raman spectrum of GD450R taken from the back-side of the sample of GD450 through the glass substrate is also shown in the figure.

It is seen that for the sample of GD424 ($R_H$ = 120) two broad envelops were observed at ~394 and ~260 cm$^{-1}$, which may correspond to Si-Ge and Ge-Ge vibrations in the amorphous network. In addition, a shoulder at ~476 cm$^{-1}$ was recognized, which should correspond to the TO phonon of a-Si. These results are similar to the earlier report on Raman spectra of a-SiGe:H [7].

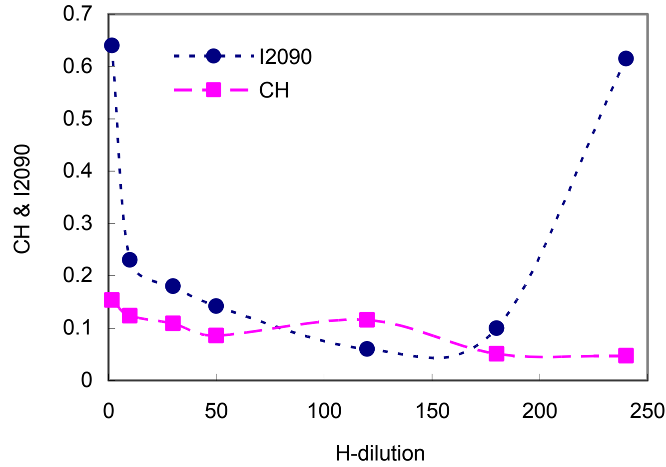


***Fig. 5-2: The relative intensity $I_{2090}$ and hydrogen content $C_H$ of a-SiGe:H samples as a function of H-dilution $R_H$ .***

For the sample of GD450, it can be seen clearly that a few crystalline SiGe Raman characteristic peaks appear in the spectrum, including the Si-Si TO phonon at 496cm$^{-1}$, the Si-Ge vibration at 402cm$^{-1}$ and Ge-Ge TO phonon at 284cm$^{-1}$. It notes that the Si-Si TO phonon has a red-shift, compared with the c-Si TO phonon. The lowered frequency could be explained in terms of the presence of the larger mass neighboring Ge atoms in the network. These observations are similar to the results reported by Jelenkovic et al [10], who obtained the similar three Raman peaks from the SiGe samples prepared by rf magnetron sputtering followed by a post-annealing crystallization at 550°C.

For Sample GD449, with a little lower H-dilution R=180 than GD450, we find that it locates near the phase transition region from amorphous to microcrystalline state. The crystalline characteristic Si-Si vibration at 498cm$^{-1}$ is just beginning to appear in the Raman spectrum, while the Si-Ge vibration at 394 cm$^{-1}$ keeps nearly unchanged, compared to its amorphous counterpart. The similar situation was also observed in the literature [10], where the crystalline Si-Si Raman peak first appeared in their spectra and then grew in intensity with the post-annealing time (see their Fig. 4). It seems that there are phase segregation phenomena occurring in a-SiGe:H films and the crystallization is beginning first from the Si-rich region in the films.

For the Raman spectrum GD450R, taken from the back-side of GD450 through the glass substrate, only one broad peak can be found at 480cm$^{-1}$, indicating that the film first grown on the glass substrate is still in amorphous state, even though $R_H$ is as high as 240. Crystallization in a-SiGe:H films is thickness-dependent as observed in a-Si:H[11].

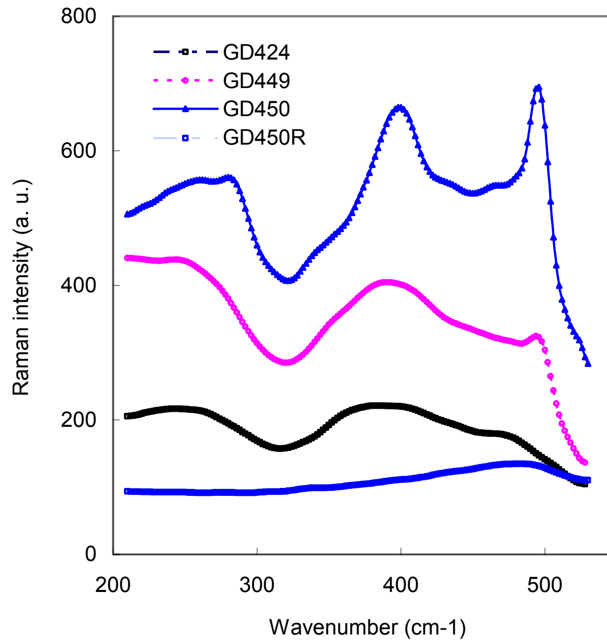


***Fig. 5-3: Raman spectra of high H-dilution a-SiGe:H samples, with $R_H$=120 (GD424), 180 (GD449) and 240 (GD450), respectively. The Raman spectra were taken from the front surface of the samples, except GD450R, which was taken from the back side of sample GD450 through the glass substrate.***

### *5.3.3 a-SiGe:H n-i-p solar cells*

The structural variation in a-SiGe:H intrinsic layer with H-dilution should be reflected in the performances of constituent solar cells. Table 5-1 lists the photovoltaic parameters of a-SiGe:H n-i-p devices made with different H dilution $R_H$ [5]. It is seen from the Table that the short circuit current density $J_{sc}$ is roughly unchanged within the experimental error. The fill factor FF seems to increase with H-dilution, but with some fluctuation. The open circuit voltage

$V_{oc}$ increases from 0.64 V to 0.67 V with $R_H$ up to 120, before it starts to decrease down to 0.64 V when $R_H$ is further increased to 240. This may be correlated with the fact that small amount of microcrystalline phase is formed at R=240.

Considering the fact that the a-SiGe n-i-p solar cells are deposited on stainless steel and only about 170nm thick, we also performed Raman scattering measurements on the solar cells. For the sample GD451 with intrinsic layer deposited under $R_H$=180, the obtained Raman spectrum shows a main peak at ~480 $cm^{-1}$ and a small shoulder at ~ 500cm-1, which could be respectively assigned to the Si-Si TO phonon in amorphous and crystalline network. This verifies that the sample is indeed at the beginning of the phase transition from amorphous to crystalline state.

Light soaking tests for these a-SiGe:H samples were also performed to understand the effect of $R_H$ on the device stability. The last column of Table 5-1 shows the degradation under one-sun light soaking at 50 $^oC$ for 1000 hours. It is found that the degradation is reduced with higher $R_H$, down from 21% for $R_H$ =10 to 11% for R=120.

***Table 5-1: Performance of a SiGe:H n-i-p devices made with different H dilution $R_H$.***

| Device | H dilut | $V_{oc}$ | $J_{sc}$ | FF | Eff | Light Degrad. |
|---|---|---|---|---|---|---|
| No. | $R_H$ | (V) | ($mA/cm^2$) | (%) | (%) | (%) |
| GD429 | 1.7 | 0.638 | 16.2 | 53.8 | 5.54 | |
| GD428 | 10 | 0.64 | 17.7 | 53.1 | 6.02 | 20.9 |
| GD425 | 30 | 0.656 | 17.4 | 59.1 | 6.76 | 21.6 |
| Gd426 | 50 | 0.662 | 17.2 | 55 | 6.25 | 14.2 |
| GD427 | 120 | 0.669 | 17 | 54.8 | 6.25 | 11.4 |
| GD451 | 180 | 0.656 | 18.1 | 56 | 6.65 | -- |
| GD452 | 240 | 0.636 | 18.5 | 55.8 | 6.55 | -- |

## 5.4 Conclusion

We have deposited a series single-layer films and n-i-p solar cells using narrow bandgap a-SiGe:H materials deposited via PECVD using different H-dilution ranging from $R_H$=1.7 to 240. Samples with higher $R_H$ value showed lower amounts of H incorporated into the films, especially in the $SiH_2$ configuration, and exhibited higher light soaking stability. The onset of the phase transition from a-SiGe:H to μc-SiGe:H occurs at about $R_H$=180. The results from the films and devices deposited using different H-dilution suggest that high H dilution up to 120 could be used to deposit a-SiGe:H films and devices with improved light stability.

**References:**

1. J. Yang, A. Banerjee, T. Glatfelter, K. Hoffman, X. Xu and S. Guha, "Correlation of component cells with high efficiency amorphous silicon alloy triple junction solar cells and modules", Proc. 1st world Conf. on Photovoltaic Energy Convention (Waikoloa, 1994) pp. 387-390.

2. P. Wickboldt, D. Pan, W. Paul, J. H. Chen, F. Zhong, J. D. Cohen, Y Chen and D. L. Williamson, "Improved a-$SiGe_{1-x}Ge_x$:H of large x deposited by PECVD", J. Non-Cryst. Solids, 198-200, 1996, pp. 567-571.
3. A.Matsuda and G. Ganguly, "Improvement of hydrogenated amorphous silicon germanium alloys using low power disilane–germane discharges without hydrogen dilution", Appl. Phys. Lett., 67, 1995 pp. 1274-1276.
4. P. Agarwal, H. Povolny, S. Han and X. Deng, "Study of a-SiGe:H Films and n-i-p Devices used in High Efficiency Triple Junction Solar Cells", J. of Non-Cryst. Solids, 299-302, 2002 pp. 1213-1218.
5. H. Povolny, P. Agarwal, S. Han and X. Deng, "Comparison Study of a-SiGe Solar Cells and Materials Deposited Using Different Hydrogen Dilution", Mat. Res. Soc. Symp. Proc. 609, 2000, A30.3.
6. X. Deng and X.B. Liao, S. Han, H. Povolny and P. Agarwal, "Amorphous Silicon and Silicon Germanium Materials for High Efficiency Triple-junction Solar Cells", Solar Energy Materials & Solar Cells, 62, 2000, pp. 89-95.
7. Y. Chou and S. Lee, "Structural, optical, and electrical properties of hydrogenated amorphous silicon germanium alloys", J. Appl. Phys. 83, 1998, pp. 4111-4123.
8. S. Sheng, X. Liao and G. Kong, "Study of the microstructure of high stability a-Si:H films by Raman Scattering and infrared absorption spectra", Appl. Phys. Lett., 73, 1998, pp. 336-338.
9. U. Kroll, J. Meier, A. Shah, S. Mikhailov and J. Weber, "Hydrogen in amorphous and microcrystalline silicon films prepared by hydrogen dilution", J. Appl. Phys., 80, 1996, pp. 4971-4975.
10. E. V.Jelenkovic, K.Y. Tong, Z. Son, C. L. .Mak, and W.Y. Cheung, "Properties of crystallized $Si_{1-x}Ge_x$ thin films deposited by Sputtering", J. Vac. Sci. Technol. A 15, 1997 pp. 2836-2841.
11. R. J. Koval et al., "Performance and stability of Si:H p-i-n solar cells with i layers prepared at the thickness-dependent amorphous-to-microcrystalline phase boundary", Appl. Phys. Lett. 75, 1999, pp. 1553-1555.

# 6 Phase Diagram for Deposition of Amorphous and Microcrystalline Silicon

*Contributors: W. Wang, W. Du, X. Yang and X. Deng*

## 6.1 Introduction

It is widely known that the deposition of amorphous and microcrystalline Si using PECVD and other thin film deposition processes depend on the hydrogen dilution of silicon containing gases ($SiH_4$ or $Si_2H_6$) in the gas phase. At lower hydrogen dilution, the film deposited is generally amorphous silicon, while at sufficiently higher hydrogen dilution, the film deposited becomes microcrystalline. For certain ranges of dilution, the film contains a mixed phases of amorphous and microcrystalline. However, the dilution level at which the phase transition from amorphous to microcrystalline occurs depends on other deposition conditions. For example, when a-Si film is thicker, it is more likely to form microcrystalline[1]. In this study, we explore the dependence of microcrystalline formation on the hydrogen dilution at different temperatures. This is important because when we want to deposit a-Si intrinsic layers for solar cells, we would like to deposit these materials near the onset of microcrystalline formation. Only if we know what the transitioning dilution level for each temperature is, we could deposit a-Si material with optimal dilution.

What is explored in this study are two dilution levels: $R_{am}$, the dilution level at which the transition between amorphous to mixed phase starts, and $R_{mc}$, the dilution level at which the mixed phase to pure microcrystalline phase starts. We investigate the dependence of $R_{am}$ and $R_{mc}$ on the substrate temperature.

The transition from a-Si to μc-Si depends not only on hydrogen dilution, it also depends on a variety of other factors, such as the film thickness and substrates. Since films for Raman measurement of microcrystalinity are usually deposited on glass and is thicker, the finding for $R_{am}$ and $R_{mc}$ may be different as in solar cell devices. To study the phase transition for application in solar cells, it is most applicable when these studies are done in real solar cell devices.

It has been reported [2] the open circuit voltage in single-junction a-Si solar cells is a sensitive measure of microcrystalline silicon formation. When the a-Si i-layer is deposited near the edge, i.e., protocrystalline, the open circuit voltage is the highest. When a mixed phase starts, the Voc starts to drop with increasing dilution. When the i-layer is dominated with microcrystalline, the Voc approaches 0.50 V. In this study, we use the open circuit voltage as an indirect measure of microcrystalline formation.

### 6.2 Experimental

Amorphous and microcrystalline n-i-p solar cells are deposited with a structure SS/n-i-p/ITO. All semiconductor layers are deposited using PECVD process. The deposition time of the i-layer is adjusted so that the i-layer thickness is approximately 120 nm, which is similar to the thickness of the i-layer as in a top component cell. The thickness of the device is calculated from the interference fringes in reflection spectra. The combined thickness of the doped layer is around 40 nm.

Forty-two nip deposition runs were made at dilution level R=$[H_2]/[Si_2H_6]$ of 25, 50, 100, 150, 175 and 200. The reading substrate temperature is set at 100, 150, 200, 250, 300, 350 and 400. The temperature range is selected to cover the temperature usually used to deposit a-Si and μc-Si while the dilution range is selected to cover the transition from amorphous to microcrystalline. Since the temperature is read from a location near the heater, away from the substrate, the actually temperature of the substrate is different. In Fig. 6-1, we show the calibration of substrate temperature as a function of the reading temperature under different gas flow scenarios. From this calibration, substrate temperatures are obtained as 75, 115, 151, 187, 220, 260, 295 C. In fact, substrate temperatures quoted in our previous reports also need to be calibrated using Fig. 6-1.

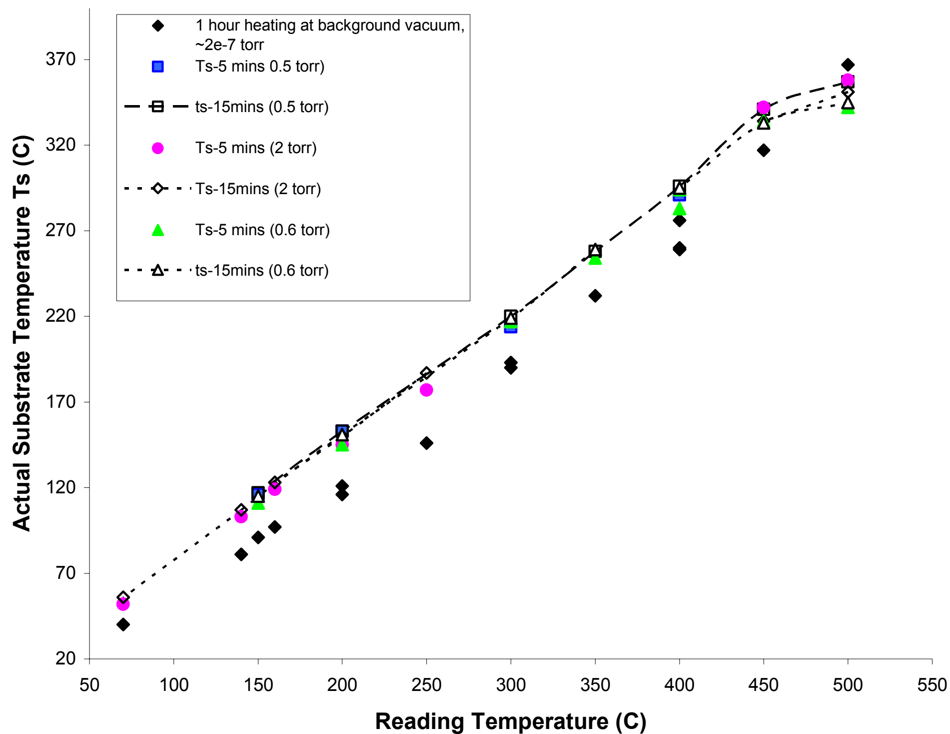


***Fig. 6-1: Calibration of actual substrate temperature from the reading temperature for UT's PECVD deposition system.***

### 6.3 Results

Table 6-1 shows the PECVD solar cell fabrication runs conducted for this study. For each deposition run, four 2"x2" samples are deposited. On each 2"x2" sample, we fabricate an array of ITO contacts. Table 6-2 shows the thickness of the nip device on stainless steel measured using reflection interference fringes. This thickness includes the thickness of the doped layers, which is around 40 nm. Therefore, the thickness of the i-layer is around 120 nm. We show the thickness here since the transition from a-Si to uc-Si depends on the thickness for each dilution level. The effect of thickness was considered in the analysis. The deposition time for the i-layers deposited at a dilution levels R of 25, 50, 100, 150, 175 and 200 are 20, 30, 60, 90, 105 and 120 min, respective, except that GD783 was deposited in 127 min. From the deposition time and thickness, the deposition rate was calculated, as shown in Table 6-3.

***Table 6-1: Single-junction a-Si solar cell devices fabricated to map out the deposition phase diagram in terms of substrate temperature and hydrogen dilution***

| Ts\R | 25 | 50 | 100 | 150 | 175 | 200 |
|---|---|---|---|---|---|---|
| 295 $^0$C | GD821 | GD808 | GD806 | GD807 | GD809 | GD816 |
| 260 $^0$C | GD788 | GD782 | GD779 | GD792 | GD810 | GD789 |
| 220 $^0$C | GD820 | GD811 | GD796 | GD812 | GD813 | GD814 |
| 187 $^0$C | GD819 | GD804 | GD780 | GD794 | GD805 | GD815 |
| 151 $^0$C | GD817 | GD801 | GD795 | GD800 | GD802 | GD803 |
| 115 $^0$C | GD818 | GD797 | GD781 | GD791 | GD793 | GD783 |
| 75 $^0$C | GD829 | GD828 | GD824 | GD826 | GD827 | GD825 |

***Table 6-2: Thickness of the nip layers for the 42 samples fabricated to map out the phase diagram. The thickness shown is in nm.***

| Ts\R | 25 | 50 | 100 | 150 | 175 | 200 |
|---|---|---|---|---|---|---|
| 295 $^0$C | 158 | 171 | 164 | 159 | 164 | 176 |
| 260 $^0$C | 154 | 164 | 154 | 180 | 165 | 173 |
| 220 $^0$C | 171 | 158 | 166 | 158 | 181 | 160 |
| 187 $^0$C | 162 | 163 | 159 | 159 | 165 | 152 |
| 151 $^0$C | 168 | 156 | 153 | 140 | 169 | 148 |
| 115 $^0$C | 168 | 156 | 159 | 135 | 158 | 146 |
| 75 $^0$C | 157 | 148 | 145 | 154 | 158 | 156 |

*Table 6-3: Growth rate, in Å/s, of i-layers deposited under different conditions.*

| Ts\R | 25 | 50 | 100 | 150 | 175 | 200 |
|---|---|---|---|---|---|---|
| 295 $^0$C | 0.98 | 0.73 | 0.35 | 0.22 | 0.20 | 0.19 |
| 260 $^0$C | 0.95 | 0.69 | 0.32 | 0.26 | 0.20 | 0.19 |
| 220 $^0$C | 1.10 | 0.66 | 0.35 | 0.22 | 0.22 | 0.17 |
| 187 $^0$C | 1.02 | 0.68 | 0.33 | 0.22 | 0.20 | 0.16 |
| 151 $^0$C | 1.06 | 0.65 | 0.31 | 0.19 | 0.21 | 0.15 |
| 115 $^0$C | 1.06 | 0.64 | 0.33 | 0.18 | 0.19 | 0.15 |
| 75 $^0$C | 0.97 | 0.60 | 0.29 | 0.21 | 0.19 | 0.15 |

*Table 6-4: Open circuit voltage of the 42 samples fabricated to map out the phase diagram*

| Ts\R | 25 | 50 | 100 | 150 | 175 | 200 |
|---|---|---|---|---|---|---|
| 295 $^0$C | 0.846 | 0.873 | 0.901 | 0.78 | 0.634 | 0.528 |
| 260 $^0$C | 0.91 | 0.921 | 0.924 | 0.77 | 0.572 | 0.52 |
| 220 $^0$C | 0.926 | 0.954 | 0.968 | 0.735 | 0.557 | 0.489 |
| 187 $^0$C | 0.948 | 0.979 | 0.989 | 0.783 | 0.538 | 0.48 |
| 151 $^0$C | 0.937 | 0.984 | 1.011 | 0.867 | 0.585 | 0.486 |
| 115 $^0$C | 0.929 | 0.976 | 1.014 | 0.814 | 0.542 | --- |
| 75 $^0$C | 0.867 | 0.927 | 0.949 | 0.862 | 0.554 | 0.512 |

Table 6-4 shows the Voc for the set of devices. Each Voc value listed in Table 6-4 is the average of the Voc values from the ITO contacts that shows highest J-V performance on each sample. Sample GD783, deposited at Ts=115C and R=200, is shunted. Therefore, the $V_{oc}$ for this sample is discarded. As we can see from Table 6-4, the highest average Voc, 1.014 V, is obtained when the i-layer is deposited at around 120C with a H dilution of 100. The highest Voc is obtained near the transition region, at a dilution level right below that for microcrystalline formation. In Fig. 6-2, we plot Voc for these devices as a function of R for each Ts. It is observed that 1) for all Ts, R=100 leads to the highest $V_{oc}$; 2) at higher $T_s$, the drop in $V_{oc}$ when R is greater than 100 occurs more slowly with increasing R, while at lower Ts, the drop in $V_{oc}$ occurs rapidly; and 3) at higher R ~ 200, all samples show Voc around 0.5 V, indicating the i-layer contains large volume fraction of microcrystalline.

Based on the information in Table 6-4, we also generated a contour plot for $V_{oc}$ in the $T_s$—R graph. The contour plot shows that highest $V_{oc}$ is generated at R ~ 90 and Ts ~ 140 °C.

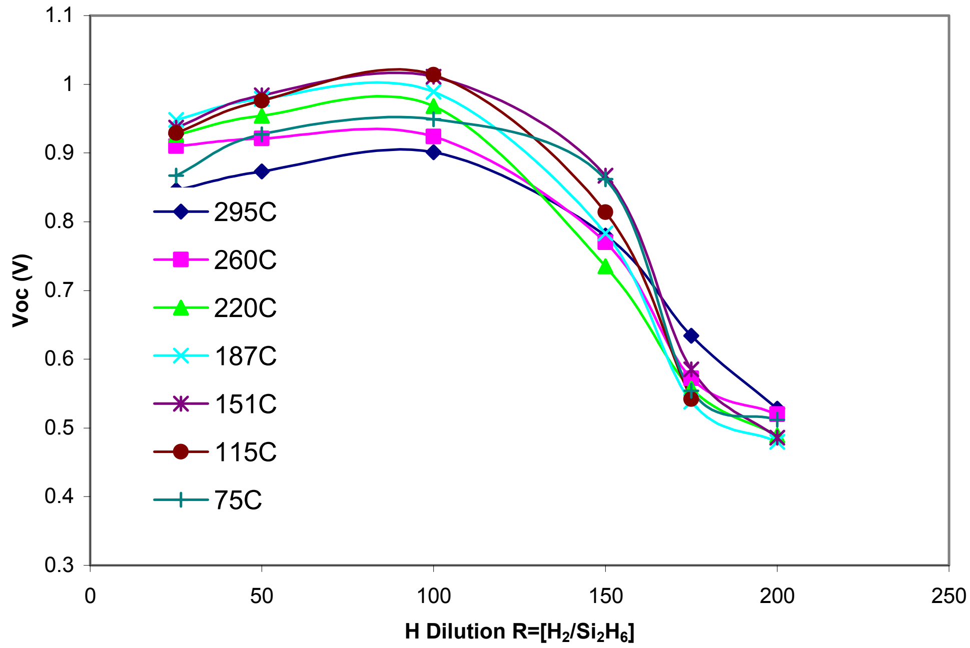


*Fig. 6-2: $V_{oc}$ of nip solar cells as a function of hydrogen dilution for different substrate temperatures*

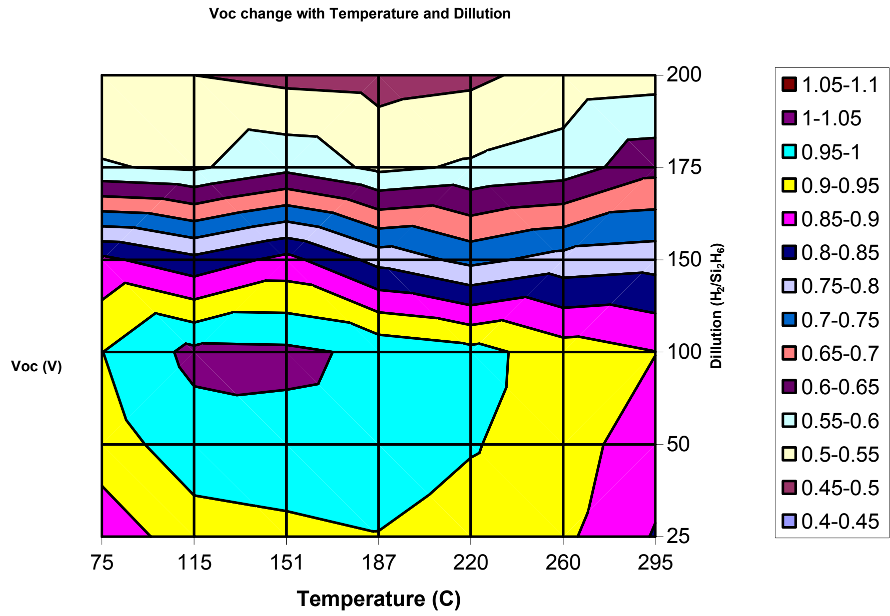


*Fig. 6-3: Contour plot of the $V_{oc}$ as a function of substrate temperature and $H_2$ dilution ratio.*

### 6.4 Discussions

Since the drop in Voc from above 0.9 V to 0.5 V with increasing R is due to the formation of microcrystalline phase in the bulk, we can use this study to generate deposition "phase diagram". The reason Voc starts to drop when R is increased beyond 100 is because small amount of microcrystals starts to form. From Fig. 6-2, we estimate the dilution at which the Voc drops 10% from its maximum value and use this dilution, $R_{am}$, as the "phase boundary" between amorphous and mixed phases, as shown in Fig. 6-4.

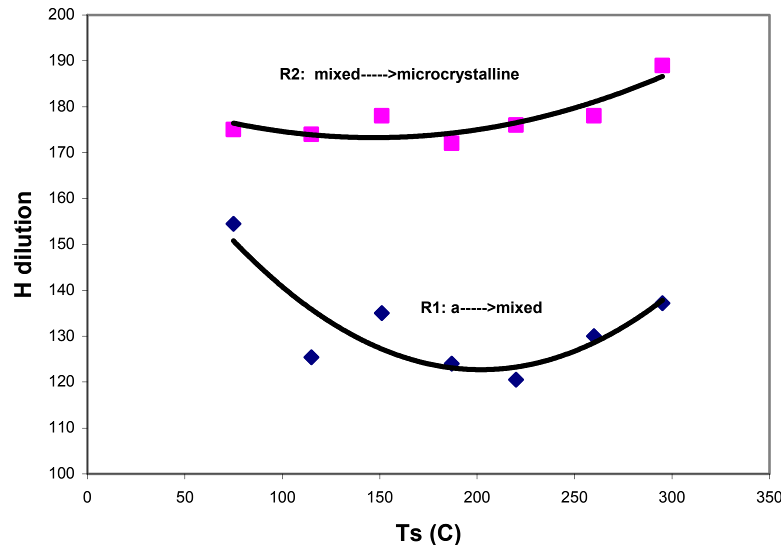


*Fig. 6-4: Phase diagram for the a-Si and microcrystalline growth in Ts-R plot.*

We then use the dilution $R_{mc}$ at which the $V_{oc}$ drops down to 0.55V as the "phase boundary" between mixed phase and microcrystalline phase, since a significant amount of microcystalites must have been formed to drop $V_{oc}$ to around 0.50 V.

From Fig. 6-2, we observe that $R_{am}$ is lowest near 200 C and it increases at both higher Ts and lower Ts. For $R_{mc}$, it is somewhat flat at low Ts and it increase when Ts is increased beyond 200C. We think the reason that $R_{am}$ is higher at low Ts, near 75 C, since at this Ts, the Si species stick to the surface easily and the material has a strong tendency to form polyhydride. Furthermore, these Si species may not land on a site that is desirable for microcrystalline Si formation and there is not enough surface mobility at this low temperature for these Si species to move around and find appropriate sites. Therefore, large amount of Si needs to be etched away from the surface through higher H dilution to form microcrystallines. At higher Ts, again, we need to have more R to form microcrystalline Si. We think this is because at higher Ts, ~300C, there maybe less H coverage on the growth surface, resulting in reduced surface mobility during growth. Consequently, higher R is needed to form microcrystallines.

## 6.5 Summary

Amorphous silicon solar cells are deposited at different substrate temperature $T_s$ and with different $H_2$ dilution ratio R. We observed the change in $V_{oc}$ with increasing R for different $T_s$. It is found that the conditions near R~90 and $T_s$~140C are most desirable to lead to high $V_{oc}$. We also generated a deposition "phase diagram" that maps out the formation of amorphous, microcrystalline and mixed phases. It is found that at Ts~200C, lowest R is needed to deposit microcrystalline Si. At both higher and lower $T_s$, we need higher R to deposit μc-Si.

### References

1. R. Collins et al. NREL a-Si team meeting. 2000.
2. J. Yang et al, NREL a-Si team meeting. 2000.

# 7 High Rate Deposition of Amorphous Silicon Films Using Hot-Wire CVD with Coil-Shaped Filament

*Contributors: Henry S. Povolny and Xunming Deng*

**Abstract**

To reduce the manufacturing cost for amorphous silicon (*a*-Si:H) based photovoltaics, it is important to deposit high-quality a-Si:H and related materials at high deposition rate. To this end, we designed and constructed a hot-wire deposition chamber with a coiled filament design and with multiple gas inlets. The process gas could be directed into the chamber through the filament coil and have maximum exposure to the high temperature filament surface. Using such a chamber design, we deposited *a*-Si:H films at high deposition rates up to 800 Å/s and dense, low-void a-Si:H at rates up to 240 Å/s.

## 7.1 Introduction

Considerable progress has been made in hydrogenated amorphous silicon (*a*-Si:H) based thin film photovoltaics during the recent years [1,2]. For high-efficiency solar cells, the *a*-Si:H layers in these devices have typically been deposited using RF Plasma Enhanced Chemical Vapor Deposition (PECVD). While RF PECVD produces cells with high efficiency, the deposition rates are generally low, around 1-5 Å/s. A number of alternative deposition techniques have been explored to deposit a-Si:H intrinsic layers at higher deposition rates. Using a very high frequency (VHF) PECVD process, high efficiency solar cell devices have been produced with a-Si:H intrinsic layers deposited at around 10 Å/s [3,4]. Hot-wire CVD (HWCVD) [5], also called Catalytic-CVD process [6], has been used to deposit a-Si:H based solar cells at higher deposition rates [7-9]. Although HWCVD-produced cells still show lower efficiency than PECVD-produced cell, the potential to deposit a-Si:H at higher rates makes HWCVD an attractive process for a-Si:H solar cell fabrication. In addition to photovoltaic application, a-Si:H is also used for other devices such as charged particle detectors [10,11]. In these devices, pin structures with i-layers thickness up to 10-20 μm are used to detect alpha particles or neutrons. Therefore, it is important to explore deposition processes that can be used to deposit a-Si:H films at high deposition rates. In this paper we report our study on the high-rate deposition of a-Si:H films using a HWCVD process employing a coiled filament design [12] and high flow rates.

## 7.2 Chamber Description

The Hot-Wire Chemical Vapor Deposition (HWCVD) chamber, shown in Fig. 7-1, consists of a high vacuum chamber, a substrate holder, a coiled filament perpendicular to the substrate, two annular gas inlets near the substrate and one axial gas inlet directed through the filament coil, a gas confinement cup and an annular RF electrode for PECVD. The substrate

holder, capable of holding a 10 cm by 10 cm substrate, is inverted over the gas confinement cup. Deposition was made on a variety of substrates including c-Si, quartz, 7059 glass, 1737 glass and stainless steel.

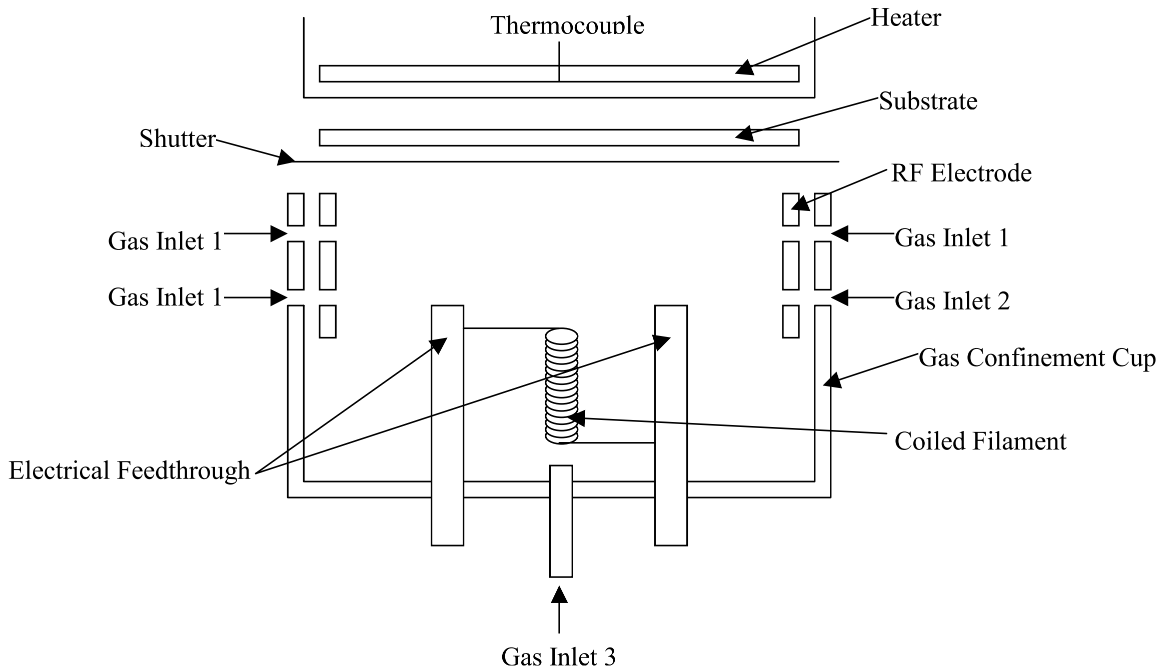


***Fig. 7-1: Schematic diagram of the Hot Wire CVD deposition chamber.***

The filament coil is typically one meter of 0.75 mm diameter tungsten wire wound in a coil approximately 7 mm in diameter and 5 cm long with around 40 evenly spaced revolutions. Both 0.2 mm and 0.5 mm diameter tungsten wires were tried but did not support themselves at deposition temperatures. The filament is attached by a short, straight length of wire at the top and bottom to two vertical posts running parallel to the filament on either side approximately 2 cm away. The top of the filament can be positioned anywhere from 4.5 cm to 6.75 cm from the substrate though 5.7 cm was the distance used for this study. Temperature of the filament was calibrated using an optical pyrometer in vacuum and with hydrogen flow at various pressures. To maintain temperature of the 0.75 mm diameter tungsten wire at 2000 °C, currents between 29.5 amps and 31.5 amps were required depending on gas flow. Only a slight dependence on flow rate was noticed though higher pressures sometimes required current increases of 1 to 2 amps to maintain filament temperature.

Process pressures ranged from 7 mTorr to 200 mTorr for HWCVD and 500 mTorr for PECVD. Process gas flows ranged from a few sccm to 140 sccm. Deposition is fairly uniform over a 2 cm by 2 cm area in the center of the substrate area but falls off by 50% or less closer to the edge.

### 7.3 Experimental Details

A series of nine samples was prepared at high flow rates both with and without hydrogen dilution on a variety of substrates including 1737 glass, 7059 glass, quartz, crystalline silicon (c-Si) and stainless steel (SS). Pressure was 100 mTorr and the filament temperature $T_{fil}$ was 2000 °C for all samples. Mixtures of $Si_2H_6$ and $H_2$ were used as the process gases. The substrate temperature $T_{sub}$ ranged from 100 to 400 °C, which was the temperature of the substrates (actually measured at the position of the heater) before filament was turned on. The actual temperature of the substrate is expected to be higher due to filament heating. The other deposition conditions are summarized in Table 7-1. A surface profilometer was employed to measure film thickness. Transmission was measured to determine the thickness and the index of refraction from the interference fringes and band gap from the Tauc plot. Fourier Transform Infrared spectroscopy (FTIR) was performed to determine hydrogen content from the integrated area of the 640 $cm^{-1}$ peak and bond preference from comparing the 2000 $cm^{-1}$ (monohydride) and 2100 $cm^{-1}$ (dihydride) peak heights. The microstructure factor, R*, the relative concentration of H in silicon dihydride and silicon polyhydride to the total H in the film, is calculated from the ratio of integrated absorption in the FTIR $[2100cm^{-1}]/([2100cm^{-1}]+[2000cm^{-1}])$. Lower R* suggests that the film is dense and has less micro voids. Electrical conductivity was measured to determine dark conductivity ($\sigma_{dark}$), photo conductivity ($\sigma_{photo}$) and the photo-to-dark conductivity ratio.

***Table 7-1: Deposition conditions of a-Si:H films using HWCVD. All samples were deposited at 100 mTorr with a filament temperature of 2000 °C.***

| Sample | $Si_2H_6$ flow (sccm) | $H_2$ flow (sccm) | $T_{sub}$ (°C) | Time (sec) | Thickness (μm) | Dep Rate (Å/s) | Sample ID |
|---|---|---|---|---|---|---|---|
| A1 | 105 | 0 | 100+ | 30 | 2.1 | 700 | HW107 |
| A2 | 105 | 0 | 200+ | 30 | 1.4 | 460 | HW113 |
| A3 | 105 | 0 | 300+ | 30 | 0.72 | 240 | HW112 |
| A4 | 105 | 0 | 400+ | 30 | 0.72 | 240 | HW111 |
| B2 | 105 | 100 | 200+ | 30 | 0.54 | 180 | HW108 |
| B3 | 105 | 100 | 300+ | 30 | 0.60 | 200 | HW109 |
| B4 | 105 | 100 | 400+ | 30 | 0.46 | 150 | HW110 |
| C | 70 | 0 | 175+ | 120 | 2.4 | 200 | HW105 |
| D | 140 | 0 | 100+ | 30 | 2.4 | 800 | HW106 |

### 7.4 Results

Table 7-1 shows the deposition conditions of a series of nine samples deposited under different conditions. Samples A1, A2, A3 and A4 were deposited at substrate temperatures of 100, 200, 300 and 400 °C. All of these four samples were deposited with a $Si_2H_6$ flow of 105 sccm without hydrogen dilution. Samples B2, B3 and B4 were deposited at $T_{sub}$ of 200, 300 and 400 °C while the flow of $Si_2H_6$ and $H_2$ were kept at 105 and 100 sccm respectively. Samples C

and D were deposited with different $Si_2H_6$ flows, designed to see whether the deposition rate is limited by $Si_2H_6$ gas flows. All of the nine samples were deposited at a pressure of 100 mTorr and a filament temperature of 2000 °C. All samples were deposited with a deposition time of 30 seconds except Sample C, which was deposited in 120 seconds. The deposition time is controlled by a shutter. The total time taken in opening and closing the shutter is estimated to be less than 1.5 sec. The thickness in Table 7-1 is obtained using a surface profilometer, measured near the center of the film, directly above the coiled filament. From Table 7-1, we see that the deposition rate of the films ranges from 150 Å/s to 800 Å/s, depending on the $Si_2H_6$ gas flow and the substrate temperature.

The deposition uniformity is poor on the 10 cm by10 cm substrates due to the nature of the coiled filament and the fact that all of the process gases were directed into the chamber through the inlet adjacent to the filament. For example, profilometer measurements indicate that at a position 3 cm away from the center the film thickness drops approximately 30%. However, the thickness is fairly uniform within a 2 cm by 2 cm area near the center.

In Table 7-2, we summarize the results from UV-visible transmission spectroscopy, FTIR spectroscopy, and photo and dark conductivity measurement. The first column lists refractive indices *n* calculated by dividing *nd* from the transmission spectroscopy and *d* from the profilometer measurement. We did not rely solely on the thickness obtained from transmission measurements as there is a large variation in the index of refraction in this set of films and the films may not be highly uniform in thickness. Here *n* is the index in the long wavelength region. The optical bandgap $E_g$ is calculated using Tauc plot $(\alpha\ h\nu)^{1/2} = B\ (h\nu - E_g)$. The bandgap for Samples A1 and D are approximate since Tauc plots do not yield straight lines. The hydrogen content ($C_H$) is calculated from the bending mode of the Si-H absorption (640 $cm^{-1}$ peak) in the FTIR spectrum. We use a conversion factor of $2.3 \times 10^{19}$ between H concentration and the integrated 640 $cm^{-1}$ absorption peak [5] and a Si density of $5\times10^{22}$ $cm^{-3}$ to calculate $C_H$. For Samples A1 and D, the actual Si density could be lower so the $C_H$ value could be higher than what is listed in Table 7-2.

***Table 7-2: Properties of a-Si:H films deposited using HWCVD.***

| Sample | n | $E_g$(opt) (eV) | hydrogen (at %) | R* (2000vs.2100) | $\sigma_{dark}$ ($\Omega^{-1}cm^{-1}$) | $\sigma_{photo}$ ($\Omega^{-1}cm^{-1}$) | Photo-sensitivity |
|---|---|---|---|---|---|---|---|
| A1 | 1.9 | ~1.9 | >10 | 1.0 | $<2\times10^{-11}$ | $1\times10^{-10}$ | >5 |
| A2 | 2.3 | 1.74 | 12 | 0.90 | $<2\times10^{-11}$ | $2\times10^{-9}$ | $>1\times10^{2}$ |
| A3 | 3.6 | 1.63 | 10 | 0.17 | $4\times10^{-10}$ | $4\times10^{-9}$ | $9\times10^{0}$ |
| A4 | 3.7 | 1.61 | 6 | 0.11 | $4\times10^{-10}$ | $5\times10^{-9}$ | $1\times10^{1}$ |
| B2 | 3.6 | 1.78 | 19 | 0.50 | $<2\times10^{-11}$ | $2\times10^{-8}$ | $>1\times10^{3}$ |
| B3 | 3.9 | 1.62 | 7 | 0.04 | $3\times10^{-10}$ | $1\times10^{-8}$ | $4\times10^{1}$ |
| B4 | 4.3 | 1.63 | 3 | 0.05 | $2\times10^{-10}$ | $2\times10^{-8}$ | $1\times10^{2}$ |
| C | 3.6 | 1.63 | 8 | 0.36 | $2\times10^{-11}$ | $8\times10^{-8}$ | $4\times10^{3}$ |
| D | 1.6 | ~1.9 | >8 | 1.0 | $3\times10^{-11}$ | $6\times10^{-9}$ | $2\times10^{2}$ |

Table 7-2 also lists the film's microstructure factor R*, calculated from FTIR spectrum. In the last three columns of Table 7-2, we show the dark conductivity ( $\sigma_{dark}$), photoconductivity

($\sigma_{photo}$), which is measured under 1 sun light intensity, as well as photosensitivity ($\sigma_{photo}/\sigma_{dark}$). $\sigma_{photo}$ and $\sigma_{dark}$ are measured using a coplanar geometry with painted silver paste electrodes.

For the four samples in series A that were deposited without H dilution, when $T_{sub}$ increases from 100° to 400 °C, the deposition rate $r_d$ drops from 700 to 240 Å/s, as we see from Table 7-1. However, as reflected in the increase in the index of refraction to ~3.7 and decrease in R*, at higher $T_{sub}$, the films are dense and with little micro voids. The bandgap drops down from ~1.9 eV to 1.61 eV, due to the drop in $C_H$ in the film from 12 at.% or greater down to 6.0 at.% when $T_{sub}$ is increased from 100° to 400 °C, since at higher $T_{sub}$, more H diffuses out of the film during the deposition, leaving less H inside. $\sigma_{dark}$ increases with $T_{sub}$, consistent with reduced bandgap at higher $T_{sub}$. $\sigma_{photo}$ increases with $T_{sub}$, partially due to the reduced bandgap and partially due to the improved structural properties. There is no obvious trend in the photosensitivity since $\sigma_{dark}$ is below the limit of the electrometer currently used in our set up. Sample A1, although deposited at high deposition rate, contains high concentration of H in dihydride and/or polyhydride mode, indicating a porous film and is not of interest for photovoltaic applications.

With H dilution during the deposition, Samples in series B show a similar trend that at higher $T_{sub}$ the films show higher n, lower bandgap, and less $C_H$ but with lower R*. Comparing Samples B2 and A2, a moderate level of H dilution, with $H_2$:$Si_2H_6$=1:1.05, reduces the deposition rate but improves significantly the structural quality of the film, as reflected from the reduced R* and higher index of refraction. It contains more H than A2 and has a slightly higher bandgap. Comparing Samples B3 and B4 with Samples A3 and A4, a moderate level of H dilution does not change the bandgap or $\sigma_{dark,}$ but it reduces $C_{H,}$ reduces R* and increases $\sigma_{photo}$ as well as the photosensitivity, and is therefore beneficial.

Sample A1, A2, C and D exhibit the effect of $Si_2H_6$ gas flow F as well as $T_{sub}$. At higher F and lower $T_{sub}$ (Samples A1 and D), the deposition rate is high, up to 800 Å/s. However, the film is porous with an R*=1. At higher $T_{sub}$ but lower F (Sample C), the film is denser and with low R*, but with lower $r_{d,}$ which is still much higher than the deposition rate typically reported in the literature, usually less than 50 Å/s. The photosensitivity is comparable among this set of films.

## 7.5 Discussions

We believe that the ability to grow films at high deposition rate is largely due to the highly efficient dissociation of gases at the filament due to the increased interaction time of the process gas with the filament. However, when the high flux of $SiH_3$ and other radicals arrive at the growth surface, $SiH_3$ radicals and H atoms do not have sufficient time to move around and find an appropriate site before the next radical arrives. Thus the non-ideal structure gets "frozen" and the material becomes porous. High temperature is needed so that the radicals on the surface can quickly move to favorable sites.

However, at these high temperatures hydrogen would diffuse out of the film at a correspondingly high rate. To maintain a high deposition rate and yet to keep H in the a-Si:H structure, we suggest to cool the substrate rapidly to below 250 °C after the completion of

deposition at high $T_{sub}$. In this way high surface mobility can be maintained during the growth to promote dense, void free films, without losing hydrogen from the bulk due to effusion after the film is deposited.

## 7.6 Conclusion

Using a HWCVD process employing a coiled filament adjacent to the gas inlet, we deposited *a*-Si:H films at high deposition rates, in the range of 140 Å/s to 800 Å/s. The higher-rate samples are porous and contain H in mostly polyhydride bonding. At higher substrate temperature, *a*-Si:H films with low microstructure are deposited at a rate up to 240 Å/s. These films are dense but with relatively low H content. We suggest that dense a-Si:H films could be deposited at high rate (e.g., 800 Å/s) at a higher substrate temperature (e.g. 400 °C) but the substrates need to be cooled down rapidly from the growth temperature immediately after the deposition to prevent H from out effusion.

**References:**


1. S. Guha, J. Yang, A. Banerjee, T. Glatfelter, K. Hoffman, S. Ovshinsky, M. Izu, H. Ovshinsky, X. Deng, Materials Research Society Symp. Proc. Vol. **336**, 645 (1994).
2. Yang, A. Banerjee, and S. Guha, Appl. Phys. Lett. **70**, 2977 (1997).
3. A. Shah, Dutta J, Wyrsch N, Prasad K, Curtins H, Finger F, Howling A, Hollenstein C, *Materials Research Society Symp. Proc. Vol.* **258**, 15 (1992).
4. X. Deng, Jones S, Liu T, Izu M, Ovshinsky S, *Proceedings of the 26th Photovoltaic Specialists Conference*, 591 (1997).
5. A. Mahan, Carapella J, Nelson B, Crandall R, Balberg I, *J. Appl . Phys*. **69**, 6728-6730 (1991).
6. H. Matsumura, *Jpn. J. Appl. Phys.* **25**, L949-951 (1986).
7. A. Mahan, Xu Y, Nelson B, Crandall R, Cohen J, Palinginis K, Gallagher A, *Appl. Phys. Lett.* **78**, 3788 (2001).
8. Q. Wang, E. Iwaniczko, J. Yang, K. Lord and S. Guha, MRS Proc. Vol. **664**, A7.5.1 (2001).
9. S. Bauer, B. Schroeder, W. Herbst and M. Lill, Proc. 2nd World Conf. on Photovoltaic Solar Energy Conversion, 363 (1998).
10. V. Perez-Mendez, J. Morel, S.N. Kaplan, and R.A. Street, Nuclear Instruments and Methods in Physics Research, **252**, 478 (1986).
11. D. Holcomb, A. Wintenberg, and X. Deng, "Pixelated neutron beam monitor development", in Proc. of International Workshop on Position-Sensitive Neutron Detectors--Status and Perspectives, June 2001, Hahn-Meitner-Institut, Berlin, Germany.
12. M. Konagai, Kim W, Tasaki H, Hallerdt M, Takahashi K, *AIP Conf. Proc.* ***157***, 142-149 (1987).

# 8 Deposition of a-SiGe:H and nc-SiGe:H Films Using HWCVD

*Contributors: Xinmin Cao, Henry S. Povolny and Xunming Deng*

**Abstract**

Using hot-wire chemical vapor deposition (HWCVD) with coil-shaped tungsten filament, amorphous and nanocrystalline silicon-germanium (SiGe) films are deposited with a filament temperature $T_{fil}$ in the range of 1700 – 2000 °C, a substrate temperature $T_{sub}$ in the range of 150 – 400 °C, and a gas mixture with a disilane/germane/hydrogen gas mixture ratio of 3.4/1.7/7, 2.4/1.7/7 and 0/1.7/7, respectively. The structural properties of as-deposited films are investigated by Scanning electron microscopy (SEM), X-ray diffraction (XRD), Raman scattering and Fourier transform infrared (FTIR) absorption spectroscopy. The influence of the filament length on film property is also studied.

## 8.1 Introduction

Amorphous SiGe alloys are used as i-layers in the tandem and triple-junction amorphous silicon based solar cells. By varying the amount of Ge in the i-layer, the band gap can be varied from ~1.1 eV (in pure a-Ge:H films) to 1.8 eV (pure a-Si:H) films. Using a triple cell structure and with a PECVD method, United Solar Systems Corp. fabricated a-Si/a-SiGe/a-SiGe solar cells with 13% stabilized efficiency [1]. Using an intrinsic a-SiGe:H absorber layer deposited by HWCVD method, Lill et al achieved solar cells with an $\eta_{initial}$ = 6.4% for pin cell structure [2] and Wang et al achieved solar cells with $\eta_{initial}$ = 7.3% for nip cell structure [3], respectively.

Recently nc-Si:H material related investigation has attracted a great deal of attention for solar cell application. Schropp et al yielded $\eta$ = 5.97 % for HWCVD nip solar cells with a nanocrystalline absorber i-layer of an amorphous / nanocrystalline phase transition [4]. By integrating nc-Si:H absorber i-layers deposited by HWCVD, Klein et al achieved solar cells with an $\eta_{initial}$ = 7.4 % for pin cell structure and $\eta_{initial}$ = 9.4 % for nip cell structure, respectively [5]. It was assumed, by deposition near the amorphous to nanocrystalline phase transition, a highly conductive nc-Si:H with a compact morphology and effective grain boundary passivation could be achieved and thus the defect density in the films could be greatly reduced.

At the University of Toledo, we deposited a-SiGe:H and nc-SiGe:H films by HWCVD with different deposition parameters. The structural properties of as-deposited films are investigated by Scanning electron microscopy (SEM), X-ray diffraction (XRD), Raman scattering and Fourier transform infrared (FTIR) absorption spectroscopy. Our goal is to find suitable HW deposition conditions for SiGe films containing amorphous / nanocrystalline phase transition and thus to obtain high quality nc-SiGe:H films with a relatively high deposition rate for solar cell applications.

## 8.2 Experimental

The SiGe films, approximately up to 1.3 μm thick, are deposited on 7059 glass, crystalline silicon (c-Si) wafer and stainless steel (SS) substrates using Hot-Wire Chemical Vapor Deposition (HWCVD) with a coil-shaped tungsten filament in an ultrahigh-vacuum, multi-chamber, load-locked deposition system. The HWCVD system consists of a high vacuum chamber, a substrate holder, a coiled filament perpendicular to the substrate, two annular gas inlets near the substrate and one axial gas inlet directed through the filament coil, a gas confinement cup and an annular RF electrode for PECVD. The substrate holder, capable of holding a 10 cm by 10 cm substrate, is inverted over the gas confinement cup. Detailed description of this HWCVD system can be seen elsewhere [6, 7].

Two types (Type L and Type S) of coil-shaped filament with the same filament diameter of 0.75 mm but with different filament lengths have been used in this study. The parameters of these two types of filament coils are shown in Table 8-1. The coil-shaped filament Type L is made of tungsten wire 100 cm long and of 0.75 mm diameter, wound in a coil of approximately 7 mm in diameter and 47 mm long with around 45 turns. On the other hand, for the coil-shaped filament Type S we used only 30 cm long same tungsten wire, wound in a coil of approximately 8 mm in diameter and 20 mm in length with around 10 turns. The tops of the filament Type L and Type S both have the same distance of about 6 cm from the substrate.

***Table 8-1: The parameters of the coil-shaped filament used in this study***

| Filament: tungsten (W), diameter of 0.75 mm, coil shaped | | | | |
|---|---|---|---|---|
| Type | Filament length | Coil turns | Coil length | Coil diameter |
| Type L | 100 cm | 45 | 47 mm | 7 mm |
| Type S | 30 cm | 10 | 20 mm | 8 mm |

A gas mixture with a disilane/germane/hydrogen gas mixture ratio of 3.4/1.7/7, 2.4/1.7/7 and 0/1.7/7 is used for depositing amorphous and nanocrystalline silicon-germanium (SiGe) films. The filament temperature $T_{fil}$ is set in the range of 1700 – 2000 °C, while the substrate temperature $T_{sub}$ in the range of 150 – 400 °C.

Transmission measurements in the Vis-NIR range (400 nm – 3300 nm) are carried out to determine the thickness, optical gap and refractive index of these films.

The film surface topographies are investigated by Scanning electron microscopy (SEM); the crystalline fraction of the films are obtained from Raman scattering spectroscopy; the orientation and size of crystallites are detected by X-ray diffraction (XRD); and the bonded hydrogen content in the films and its bonding nature with Si and Ge is determined from Fourier transform infrared (FTIR) absorption spectroscopy.

## 8.3 Results and Discussions

### *8.3.1 Dependence of Deposition rate and surface topography on Tfil and Tsub*

The deposition rate $r_{dep}$ of SiGe-films deposited by HWCVD is significantly influenced by the filament temperature $T_{fil}$, but not that much by the substrate temperature $T_{sub}$, as shown in Fig. 8-1. At a $Si_2H_6$ flow rate $F_{Si2H6}$ = 3.4 sccm, $GeH_4$ flow rate $F_{GeH4}$ = 1.7 sccm, $H_2$ flow rate $F_{H2}$ = 7.0 sccm, a total process pressure p = 3.1 mTorr and a substrate temperature $T_{sub}$ = 200°C, the deposition rate $r_{dep}$ increases from 2.8 Å/s to 7.9 Å/s with increasing filament temperature $T_{fil}$ from 1800 °C to 2000°C. While the substrate temperature is at $T_{sub}$ = 300°C, the deposition rate $r_{dep}$ increases from 3.3 Å/s to 8.7 Å/s with increasing filament temperature $T_{fil}$ from 1800 °C to 2000°C. All the four depositions have the same deposition time of t = 15 min. The increase in deposition rate at the higher $T_{fil}$ may be attributed to the higher gas cracking efficiency due to higher filament temperature where availability of growth precursors ($SiH_3$ etc) and atomic hydrogen (H) both are expected to be high enough. In the further structural characterizations we shall verify the effects of these factors on material properties.

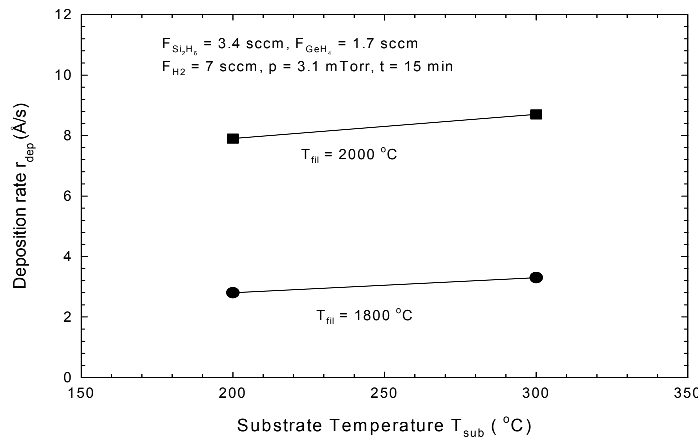


***Fig. 8-1: Dependence of the deposition rate $r_{dep}$ on the filament temperature $T_{fil}$ and the substrate Temperature $T_{sub}$ at a $Si_2H_6$ flow rate $F_{Si2H6}$ = 3.4 sccm, $GeH_4$ flow rate $F_{GeH4}$ = 1.7 sccm, $H_2$ flow rate $F_{H2}$ = 7.0 sccm, a total process pressure p = 3.1 mtorr.***

The film topographical structures of the above four SiGe samples are also characterized by SEM. Fig. 8-2a and 2b show the SEM images of the two samples deposited at $T_{fil}$ =1800 °C with the substrate temperature of $T_{sub}$ = 200°C and $T_{sub}$ = 300°C, respectively. The two films have relatively smooth surface. Fig. 8-2c and 2d show the SEM images of the two samples deposited at $T_{fil}$ =2000 °C with the substrate temperature of $T_{sub}$ = 200°C and $T_{sub}$ = 300°C, respectively. These films at $T_{fil}$ =2000 °C have very rough surfaces. This maybe results from the production of nanocrystalline SiGe grains at a relative high deposition rate.

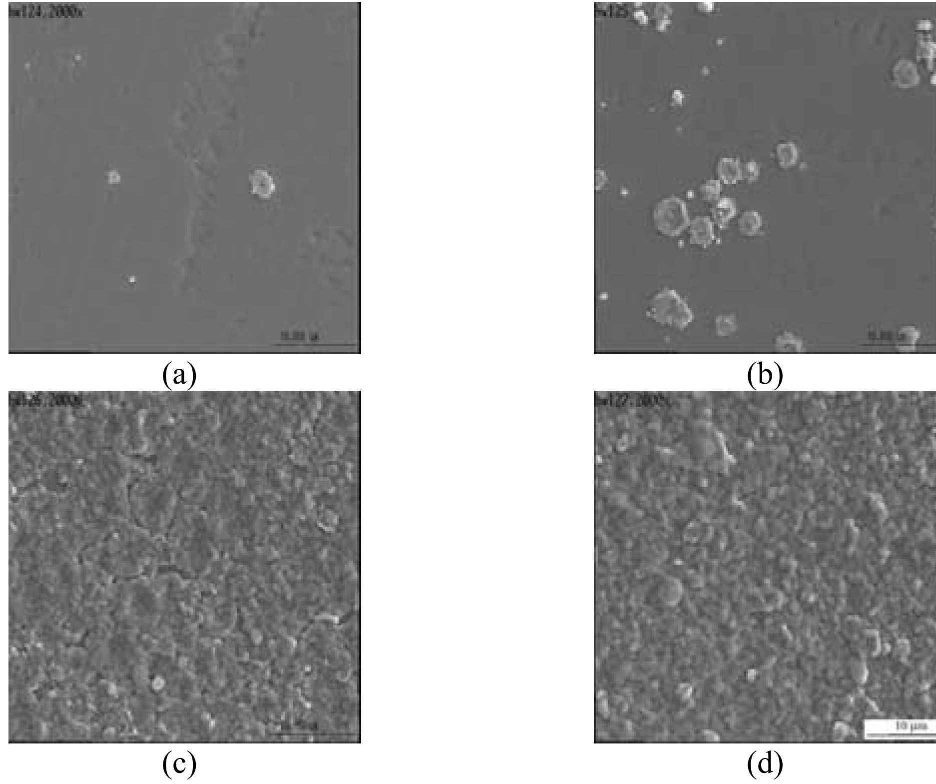


***Fig. 8-2: Top-view SEM images of SiGe samples deposited at a $Si_2H_6$ flow rate $F_{Si2H6}$ = 3.4 sccm, $GeH_4$ flow rate $F_{GeH4}$ = 1.7 sccm, $H_2$ flow rate $F_{H2}$ = 7.0 sccm, a total process pressure p = 3.1 mtorr using a) $T_{fil}$ =1800 °C and $T_{sub}$ = 200°C, b) $T_{fil}$ =1800 °C and $T_{sub}$ = 300°C, c) $T_{fil}$ =2000 °C and $T_{sub}$ = 200°C, and d) $T_{fil}$ =2000 °C and $T_{sub}$ = 300°C.***

### *8.3.2 Dependence of film crystallinity on different $T_{fil}$, $T_{sub}$ and gas mixtures*

Raman measurements are done on a series of SiGe films, which are deposited with different $GeH_4$, $Si_2H_6$ and $H_2$ gas mixtures at a filament temperature $T_{fil}$ ranged from 1800 °C to 2000°C and a substrate temperature $T_{sub}$ ranged from 150 to 300°C. From the Raman spectra as shown in Fig. 8-3, the Raman characteristic vibrations of dominant nanocrystalline phases could be observed clearly. Crystalline Si-Si TO band near 500 $cm^{-1}$, crystalline Si-Ge TO band near 400 $cm^{-1}$ and crystalline Ge-Ge TO band near 300 $cm^{-1}$ appear in the Raman spectra. It can be seen that the positions and intensities of the Si-Si, Si-Ge and Ge-Ge Raman peaks are obviously shifted and changed with the disilane/germane/hydrogen gas mixture ratio R. The Raman spectra of the HW samples HW124, HW125, HW126, HW127 and HW132, which are deposited at a disilane/germane/hydrogen gas mixture ratio of 3.4/1.7/7 corresponding to $R_H$ (=$[H_2]/([Si_2H_6]+[GeH_4]+[H_2])$) of 58% have a Si-Si Raman peak centered at 507 $cm^{-1}$, Si-Ge Raman peak at 400 $cm^{-1}$ and Ge-Ge Raman peak at 282 $cm^{-1}$. The intensity of the Si-Si Raman peak is also higher than those of Ge-Si and Ge-Ge Raman peaks. The Si-Si TO band in the nanocrystalline SiGe films are centered around 507 $cm^{-1}$ and have a peak shift of about 13 $cm^{-1}$ as compared to the crystalline Si-Si TO band centered near 520 $cm^{-1}$ in the single crystalline Si

films. This suggests that with the presence of Ge in the SiGe film the crystalline Si-Si bonding length becomes a little bigger than normal.

The Raman intensity of Ge-Ge and Si-Ge peak increases with increasing germane content in the gas mixture, meanwhile the Raman peaks are also shifted. As shown in the Raman spectra of the samples HW128, HW129, HW130 and HW131 with a disilane/germane/hydrogen gas mixture ratio of 2.4/1.7/7 corresponding to $R_H$ of 63 %, Si-Si peak is shifted to 502 $cm^{-1}$, Si-Ge Raman peak to 404 $cm^{-1}$ and Ge-Ge Raman peak to 287 $cm^{-1}$, while the intensity of Si-Ge and Ge-Ge peak also increase.

Raman measurements are also done on pure Ge films of the HW samples HW133-136 deposited with a disilane/germane/hydrogen gas mixture ratio of 0/1.7/7 (without disilane) corresponding to $R_H$ of 80%, and only sharp Ge-Ge TO peaks centered near 300 $cm^{-1}$ are present in these Raman spectra.

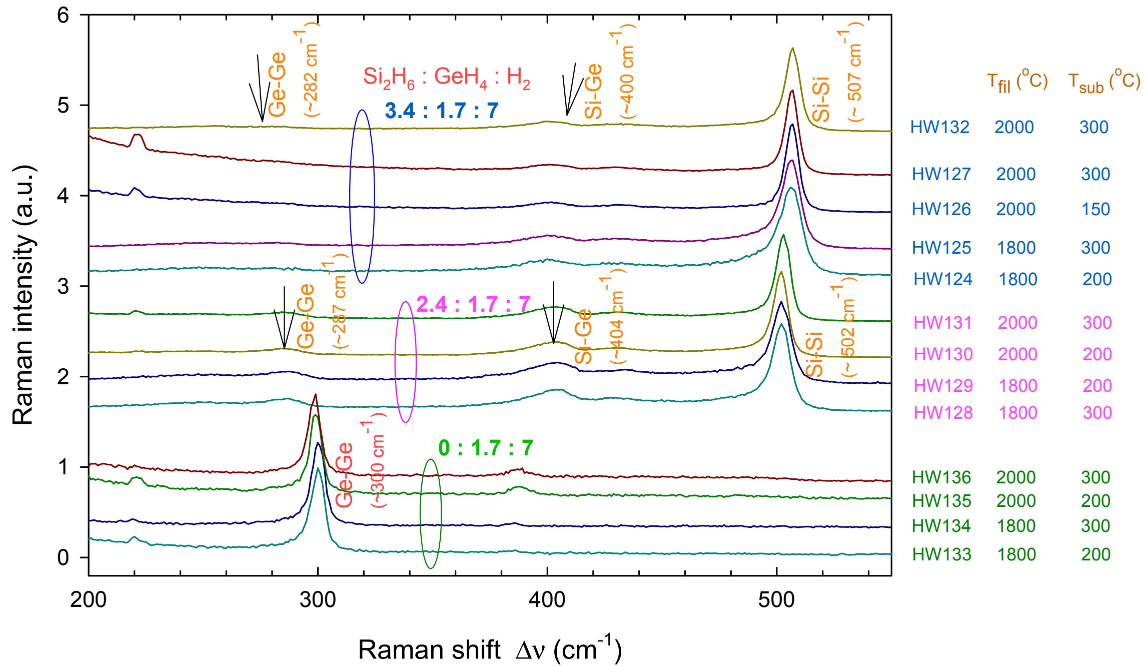


***Fig. 8-3: Raman spectra of SiGe and Ge films deposited with different $T_{fil}$, $T_{sub}$ and gas mixtures.***

The filament temperature $T_{fil}$ and substrate temperature $T_{sub}$ have influences on the film growth of amorphous and nanocrystalline phases. The Raman spectrum of sample HW127 deposited at $T_{fil}$ = 2000 and $T_{sub}$ = 300 °C has a narrow Si-Si TO band centered at 507 $cm^{-1}$ with a FWHM of only 7 $cm^{-1}$, which indicates HW127 is nanocrystalline SiGe with nearly 79% volume fraction of nc-SiGe phase. With decreasing filament temperature $T_{fil}$ and substrate temperature $T_{sub}$, as shown in the Raman spectrum of sample HW124 deposited at $T_{fil}$ = 1800 and $T_{sub}$ = 200 °C, the Si-Si band width FWHM increases to 14 $cm^{-1}$, meanwhile the left-side shoulder of Si-Si TO band rises. This indicates that HW124 is characteristic of nanocrystalline

SiGe with mixed-phase contributions of a-SiGe:H and nc-SiGe, and the crystalline volume fraction is $X_c \sim 60$ %.

Fig. 8-4 shows the grazing incidence diffraction (GID) X-ray pattern of the SiGe film deposited on a quartz glass substrate at a $Si_2H_6$ flow rate of $F_{Si2H6}$ = 3.4 sccm, $GeH_4$ flow rate of $F_{GeH4}$ = 1.7 sccm, $H_2$ flow rate of $F_{H2}$ = 7.0 sccm, a total process pressure of p = 2.5 mTorr, a substrate temperature of $T_{sub}$ = 200 °C and a filament temperature $T_{fil}$ = 1800°C for 10 min with a film thickness of d = 141 nm. In the GID X-ray spectrum, diffraction at the SiGe planes (111) centered at $2\theta$ = 28.30°, (220) centered at $2\theta$ = 46.96° and (311) centered at $2\theta$ = 55.66° can be seen clearly. With comparing the relative peak heights of (220) and (311) peaks to (111) peak, it can be determined that the crystallites of this SiGe film are randomly distributed. With X-ray diffraction patterns the crystallite size $d_{x\text{-}ray}$ can be calculated from the Debye-Scherrer equation.[8] The crystallite size of this SiGe film calculated from the peak (111) is $d_{x\text{-}ray}$ = 17 nm.

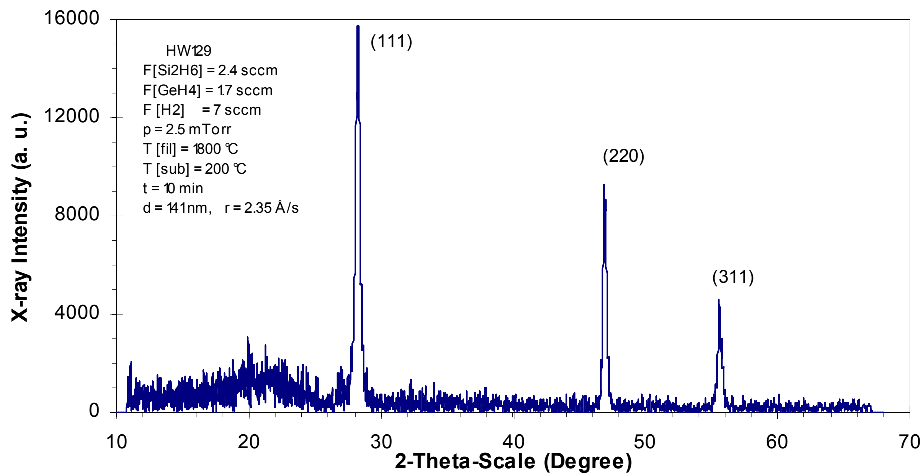


***Fig. 8-4: The GID X-ray spectrum of the SiGe film deposited at $F_{Si2H6}$ = 3.4 sccm, $F_{GeH4}$ = 1.7 sccm, $F_{H2}$ = 7.0 sccm, p = 2.5 mTorr, $T_{sub}$ = 200 °C and $T_{fil}$ = 1800°C for 10 min with a film thickness of d = 141 nm.***

### *8.3.3 Influence of filament length*

The above described SiGe and Ge films all have been deposited using the coil-shaped filament Type L with a typically filament length of 100cm. The Raman results show that all these films are of dominant nanocrystalline phases with the crystalline volume fraction $X_c > 80$ % even though the filament temperature is $T_{fil} \sim 1800$ °C and the substrate temperature as low as $T_{sub} \sim 150$ °C. The hydrogen content and bonding structure is determined from Fourier transform infrared (FTIR) absorption spectroscopy. The FTIR results show that the hot-wire nc-SiGe films have very small hydrogen contents of < 2%, which are nearly undetectable by our FTIR system.

If the filament is replaced with the coil-shaped filament Type S with a typically filament length of 30 cm, the film structures and deposition rates are greatly changed although the other deposition parameters are maintained at same values. Using filament Type S instead of Type L, one set of four deposition runs is made at $F_{Si2H6}$ = 3.4 sccm, $F_{GeH4}$ = 1.7 sccm, $F_{H2}$ = 7.0 sccm, t = 15 min and p = 3.1 mTorr by setting $T_{sub}$ = 200 °C and 300 °C, $T_{fil}$ = 1800°C and 2000°C, respectively. The four depositions have a nearly same deposition rate of about 5.7 Å/s. Raman results show that the four samples are characteristic of nearly 100% amorphous SiGe phase. As shown in Fig. 8-5a, the Raman spectrum of a-SiGe layer deposited at $T_{sub}$ = 200 °C and $T_{fil}$ = 1800°C consists of three main broad bands which are due to TO-mode Si-Si (~465 $cm^{-1}$), Si-Ge (~370 $cm^{-1}$) and Ge-Ge (~250 $cm^{-1}$) vibrations.

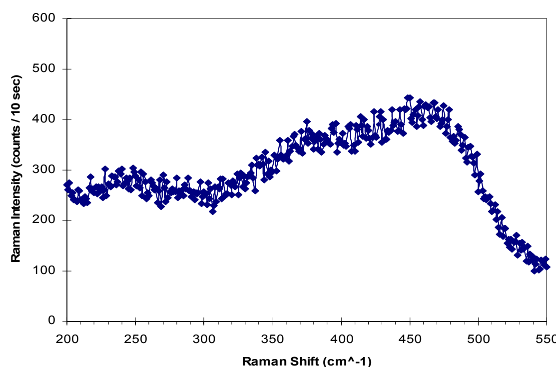


(a)

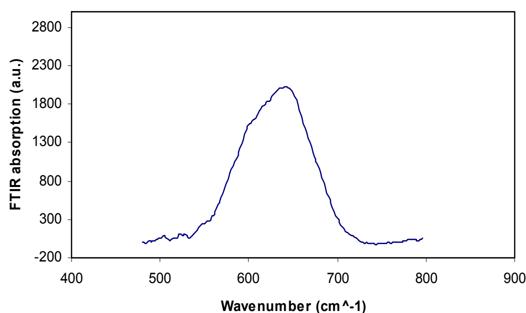


(b)

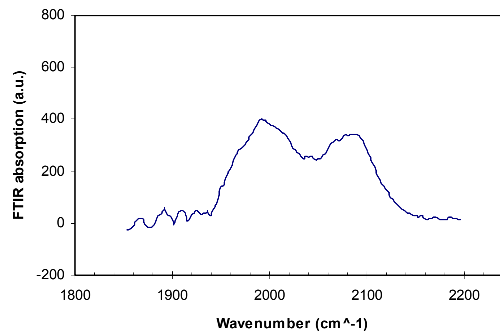


(c)

***Fig. 8-5: Raman and FTIR spectra of SiGe films deposited at $F_{Si2H6}$=3.4 sccm, $F_{GeH4}$=1.7 sccm, $F_{H2}$=7.0 sccm, p=3.1 mTorr, $T_{sub}$ = 200 °C and $T_{fil}$ = 1800°C for 15 min using filament Type S.***

Fig. 8-5b and Fig. 8-5c shows the FTIR absorption spectrum of this sample in the region of 400 – 800 $cm^{-1}$ and 1800 – 2200 $cm^{-1}$, respectively. The FTIR spectrum in 400 – 800 $cm^{-1}$ region has a peak centered at 640 $cm^{-1}$ and a shoulder at 590 $cm^{-1}$ corresponding to Si-H and Ge-H wagging modes respectively. A hydrogen content of about 7.6% is found out in this SiGe film by calculating the area under this curve in 400 – 800 $cm^{-1}$ region. The FTIR spectrum in 1800 – 2200 $cm^{-1}$ region has a peak centered at 1992 $cm^{-1}$ and a peak at 2086 $cm^{-1}$ corresponding to Si-H

and Si-$H_2$ stretching modes respectively. A Si-$H_2$/[Si-H+ Si-$H_2$] ratio of 0.43 are determined in this film by calculating the area under the corresponding peaks in 1800 – 2200 $cm^{-1}$ region.

From the Raman and FTIR results, it can be suggested that using the Filament Type L of 100 cm long, the disilane/germane/hydrogen gas mixture of 3.4/1.7/7, 2.4/1.7/7 and 0/1.7/7 corresponding to $R_H$ of 58% - 80%, has a high gas cracking efficiency resulting in the reaction area over the substrate with a high density of reactive hydrogen atoms , thus nanocrystalline SiGe films with high crystalline fractions of > 80% but with low hydrogen contents of < 2% are preferably grown. While the Filament Type S with a length of 30 cm has a relative lower gas cracking effect, as a result, only amorphous SiGe are preferably produced with the disilane/germane/hydrogen gas mixture ratio of 3.4/1.7/7.

## 8.4 Summary

Nanocrystalline SiGe films deposited at a rate about 8 Å/s result in rough surfaces. The Raman spectrum of nanocrystalline SiGe films consist of three main peaks which are due to TO-mode Si-Si (~500 $cm^{-1}$), Si-Ge (~400 $cm^{-1}$), Ge-Ge (~300 $cm^{-1}$). Peak positions and intensities are sensitive to Si/Ge content in layers, which related to gas flow ratio of $Si_2H_6/GeH_4/H_2$. Using a filament of 100 cm long, nanocrystalline SiGe films with crystalline fractions of > 80% and low hydrogen contents of < 2% are preferably grown. Using a short filament with length of 30cm, deposition of amorphous rather than nanocrystalline materials is obtained. The Raman spectrum of amorphous SiGe layer consists of three main broad bands which are due to TO-mode Si-Si (~465 $cm^{-1}$), Si-Ge (~370 $cm^{-1}$), Ge-Ge (~250 $cm^{-1}$).

**References:**


1. J. Yang, A. Banerjee, and S. Guha, Appl. Phys. Lett. 70, 2975 (1997).
2. M. Lill and B. Schroeder, J. Appl. Phys. 74, 1284 (1999).
3. Q. Wang, E. Iwaniczko, Y. Xu, W. Gao, B. P. Nelson, A. H. Mahan, R. S. Crandall, and H. M. Branz, MRS Spring Meeting Proc. 664, A4.3.1 (2000).
4. R. E. I. Schropp, Y. Xu, E. Iwaniczko, G. A. Zacharias, A. H. Mahan, MRS Symp. Proc. 715, A26.3.1 (2002).
5. S. Klein, F. Finger, R. Carius, B. Rech, L. Houben, M. Luysberg, M. Stutzmann, MRS Symp. Proc. 715, A26.4 (2002).
6. Herry S. Povolny, Doctoral Thesis “Amorphous and Microcrystalline Silicon Photovoltaic Devices Deposited by Hot-wire Chemical Vapor Deposition”, The University of Toledo (USA), March 2003.
7. X. Deng, “High Efficiency and High Rate Deposited Amorphous Silicon-Based Solar Cells”, NREL Phase I Annual Technical Progress Report (Sept. 01, 2001 – Aug. 31, 2002), pp21-26.
8. B. D. Cullity, Elements of X-Ray Diffraction, 2nd ed. (Addison-Wesley, Reading, MA, 1978), pp.281-284.

# 9 Amorphous Silicon Deposited Using Trisilane as Precursor

*Contributors: W. Du, X. Yang and X. Deng, UT*

*Mike Pikulin and John de Neufville, Voltaix.*

**Abstract**

We explored the deposition of hydrogenated amorphous silicon (a-Si:H) and hydrogenated nanocrystalline silicon (nc-Si:H) using trisilane ($Si_3H_8$) gas as the silicon precursor in a plasma enhanced CVD process, to improve our understanding of the growth chemistry and the dependence of Si:H properties on the use of precursors. The film study shows that the transition from amorphous to amorphous/nanocrystalline mixed phase with increasing hydrogen dilution R (($[H_2]/[Si_3H_8]$) or ($[H_2]/[Si_2H_6]$)) is more gradual for $Si_3H_8$-deposited Si:H as compared with disilane ($Si_2H_6$) deposited Si:H and for the former the transition occurs at a higher hydrogen dilution level R. The deposition rate of Si:H with different hydrogen dilution is more dependent on the atomic ratio of H to Si rather than the ratio of molecular hydrogen and silicon-containing precursors. Open circuit voltages ($V_{oc}$) of a-Si:H single-junction n-i-p solar cells versus hydrogen dilution is used as a measure of nanocrystalline formtion in the i-layer. Highest $V_{oc}$ is obtained when a-Si:H films are deposited using $Si_3H_8$ at R~200 while highest $V_{oc}$ is obtained for $Si_2H_6$ at R~100.

## 9.1 Introduction

Various silicon precursors, including $SiH_4$, $Si_2H_6$, $SiF_4$, and $SiH_2Cl_2$, have been used for the deposition of a-Si:H (or a-Si) in a plasma enhanced chemical vapor deposition (PECVD, rf 13.56 MHz) process. Among these different precursors, $SiH_4$ and $Si_2H_6$ were found to produce a-Si:H materials with the highest photovoltaic quality. Compared with $SiH_4$, $Si_2H_6$ has higher dissociation rate in plasma and results in different concentrations of reactive species such as $SiH_3$ in the plasma. Such a different concentrations of reactive $SiH_3$ species, believed to be responsible for the growth of high quality a-Si:H, leads to different deposition rate and different optimal level of hydrogen dilution for the growth of high quality a-Si:H.

When these silicon precursors are sufficiently diluted in hydrogen during PECVD process, nc-Si:H (or nc-Si), having grain size in the order of magnitude of 10nm, is often obtained. In the intermediate level of hydrogen dilution, a mixed phase with coexisting a-Si:H and nc-Si:H is usually obtained where nanometer sized Si crystals remain embedded in amorphous Si matrix. It is generally found that a-Si:H with highest stability under extended light illumination accompanied with reasonably high photosensitivity is often obtained at a hydrogen dilution level right below the transition from amorphous to mixed phase. A-Si:H deposited under these conditions are often referred to as "protocrystalline Si", or "edge Si" materials. The range of optimal hydrogen dilution for the deposition of high-quality protocrystalline Si depends on the selection of Si precursor and other deposition conditions and is generally quite narrow. It also changes with the thickness of the a-Si:H film as well as the types of substrates. The sharp nature of transition region hinders reproducibility of the materials deposited within. It is desirable to

have a silicon precursor that offers a wider range of hydrogen dilution for the deposition of high quality protocrystalline Si material.

Trisilane, $Si_3H_8$, is another member of the silicon-hydrogen compound gasses. It has a different dissociation rate than $SiH_4$ and $Si_2H_6$ in an rf plasma. It is expected that $Si_3H_8$ could lead to a higher concentration of SiH3 species in plasma when the gas is diluted in appropriate amount of hydrogen. This may lead to higher quality a-Si:H and/or wider window for the deposition of high quality a-Si:H. A systematic study of $Si_3H_8$ deposition of Si:H could lead to a deeper understanding of the nature of transition from amorphous to mixed and finally to nanocrystalline phase of Si:H during PECVD growth under high hydrogen dilution. Such a study may also lead to a-Si:H material with improved stability under extended illumination. In this work, the growth of Si:H near the transition region using $Si_3H_8$ and $Si_2H_6$ as the precursor gasses is studied. This comparative study is carried out by depositing and characterizing both single layer undoped films and solar cell devices.

## 9.2 Experiment details

Trisilane is a pyrophoric liquid. For PECVD or CVD applications it can be supplied as a gas mixture or as the pure liquid. Due to its low vapor pressure (approximately 250 T at room temperature), for any large volume application, liquid packaging is required. This normally involves a conventional MOCVD "bubbler", essentially a container with a "dip-tube" – a tube immersed in the liquid - and two valves, one connected to the "head space", and the second connected to the dip-tube. A carrier gas is passed down the dip-tube, creating a stream of bubbles containing a gas mixture of trisilane in the carrier gas, which is removed via the head space valve. The concentration of trisilane in that mixture can be controlled by the temperature of the bubbler and the pressure of the carrier gas.

From a regulatory standpoint, Trisilane is not listed on the USEPA's Toxic Substances Control Act ("TSCA") Inventory. It is supplied by Voltaix under a "Low Volume Exemption" (40 CFR 723) and its use is restricted to the formation of silicon and silicon compounds.

A-Si:H films and devices are grown in a multi-chamber PECVD system with a load lock chamber. In such a study, it is important to make sure that the measurement of the $Si_3H_8$ and $Si_2H_6$ gas flows is reliable. For this reason, the $Si_3H_8$ and $Si_2H_6$ gasses, both obtained from Voltaix, Inc., are introduced into the PECVD chamber via a common mass flow controller. The gas factors of the mass flow controller for $Si_3H_8$ and $Si_2H_6$ gasses were calibrated and verified by pressurizing the deposition chamber using $Si_3H_8$ and $Si_2H_6$ gasses separately, both through the same mass flow controller. In addition, the deposition of Si:H films and devices using $Si_3H_8$ and $Si_2H_6$ were carried out alternatively to avoid any unwanted effect due to the systematic and unknown drift, if any, of the deposition equipment and device processing procedures.

While hydrogen dilution is changed during the growth of these films, the other deposition conditions are kept to be the same as the standard i-layer deposition conditions used for the deposition of high-quality a-Si:H solar cells in the same PECVD system. These conditions: substrate temperature $T_s$ at 150ºC, chamber pressure at 0.6Torr and rf power at 25mW/cm$^2$, are

kept unchanged for films deposited using both $Si_3H_8$ and $Si_2H_6$. The hydrogen dilution R was varied from 71 to 286 and from 75 to 149 using $Si_3H_8$ and $Si_2H_6$ respectively. Various substrates, including quartz, glass (Corning 1737), c-Si wafer, and stainless steel foil, are used for Si:H deposition for various optical, electrical and structural characterization. The film thicknesses range from 250nm to 500nm.

A-Si:H solar cells with n-i-p structure were deposited on Al/ZnO coated stainless steel. Intrinsic-layer deposition condition was the same as described above. The window p-layer was deposited at low $T_s$, about 70-100 ºC, and high hydrogen dilution. ITO was sputtered on the p-layer as transparent conductive coating. Light soaking was done under white light at 1 sun intensity and the ambient temperature was ~ 40-50 °C.

Infrared absorption spectroscopy was measured for Si:H films deposited on c-Si substrate in the ranges from 400cm$^{-1}$ to 800 cm$^{-1}$ and from 1800cm$^{-1}$ to 2400 cm$^{-1}$ and with a resolution of 0.33 cm$^{-1}$. The integrated strength for the wagging mode at 640cm$^{-1}$ was used to obtain the H content (at.%). The stretching modes at 2000cm$^{-1}$ and 2100 cm$^{-1}$ were used to obtain the microstructure factor R* in the film. Gaussian distribution was used to fit the absorption peaks. Transmission spectra were recorded using a Cary 5 spectrophotometer. Scanning range was from 400nm to 2200nm. Thickness was calculated using the method described in the literature.[1] Raman scattering was performed to characterize the structure of Si:H films. 488nm laser line from a water-cooled $Ar^+$ laser was used for the excitation. Photoconductivity was measured when the samples were annealed in a test chamber purged with $N_2$. A pair of Ag electrodes, ~2 mm apart, were painted on the films. Samples are heated to 180ºC and the temperature dependence of dark conductivity is measured during the cooling process, from 180ºC to 50ºC. Activation energy was measured from a semilog plot (log σ *vs* 1000/T). Photoconductivity was measured using a ELH lamp at 100 mW/cm$^2$ intensity at room temperature (25ºC).

## 9.3 RESULTS AND DISCUSSIONS

Fig. 9-1 shows the deposition rate of intrinsic layers as a function of hydrogen dilution R. Film thickness was calculated from the transmission spectrum. The deposition rate of $Si_3H_8$ samples is higher than that of $Si_2H_6$ samples when the two films are deposited with the same R. As R is increased from 75 to 285 for $Si_3H_8$ samples, deposition rate is decreased from 0.45 Å/sec to 0.2 Å/sec. Lower deposition rate is observed for $Si_2H_6$ samples with the same R. In each series, smaller deposition rate is observed at higher dilution R. This decrease in deposition rate often accompanies with formation of nanocrystalline phase which is a more ordered structure. The increase in hydrogen dilution provides the required atomic hydrogen to etch out the disordered portion of the growing a-Si:H films and also provide the hydrogen coverage on the growing surface. Thus the deposition rate decreases and simultaneously these factors induce the propagation of nanocrystalline network in the films. It is additionally observed that, $R_t$, the hydrogen dilution level at which the transition from amorphous to an amorphous/nanocrystalline silicon mixed phase occurs, is higher for a-Si:H films deposited using $Si_3H_8$. $R_t$ is around 200 for $Si_3H_8$ while $R_t$ is around 150 for $Si_2H_6$. The deposition rate is also plotted against the atomic dilution ratio, $R_a$=[H]/[Si], which is the ratio of number of hydrogen and silicon atoms in the gas. Since $R_a$ is identical to R for $Si_2H_6$, only deposition rate dependence on $R_a$ for $Si_3H_8$ samples is

added in Fig. 9-1, as solid triangle symbols. It is further observed that the deposition rate *vs* $R_a$ curves are approximately the same for both gasses. Therefore, the deposition rate is more influenced by the ratio of the total number of Si atoms to hydrogen atoms directed into the chamber rather than the number of Si-containing molecules.

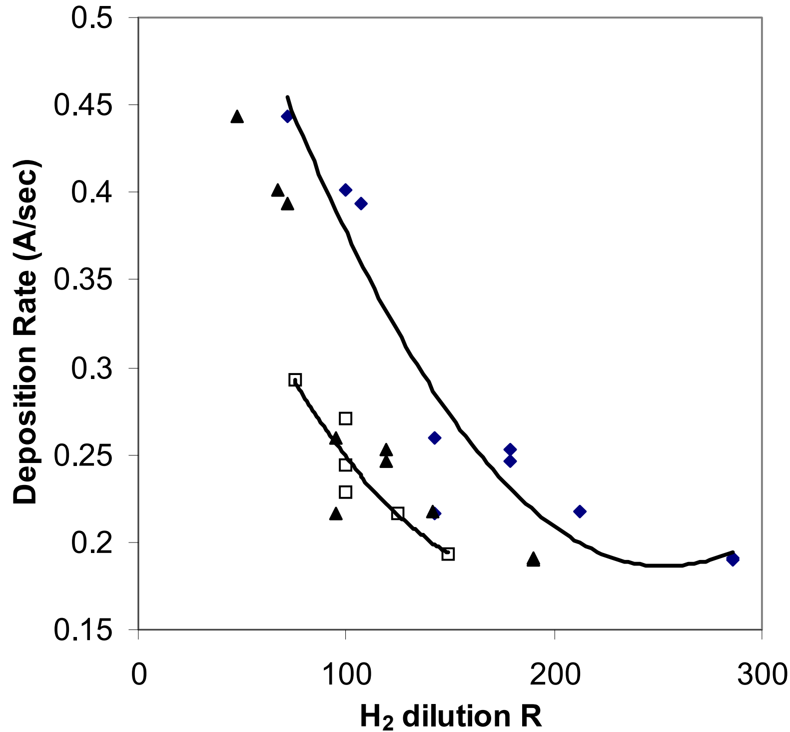


***Fig. 9-1: Deposition rates of intrinsic a-Si:H film deposited under the conditions of RF power =25mW/cm$^2$ and $T_s$=150ºC. Square symbols represent $Si_2H_6$ series and diamond symbols represent $Si_3H_8$ series; The solid triangles represent the relationship between deposition rates and $R_a$=[H]/[Si] for $Si_3H_8$ series.***

It is widely known that high-quality a-Si:H material is often deposited near the transition region from amorphous to nanocrystalline via a hydrogen dilution mediated path. A material deposited near such a transition region is sometimes referred to as protocrystalline or "edge" material. In order to find $R_t$ for both $Si_2H_6$ and $Si_3H_8$, a-Si:H films are deposited on a variety of substrates at different R. $Si_3H_8$-deposited films in this study are deposited with R ($H_2$ (sccm):$Si_3H_8$(sccm)) of: 71 (50:0.7); 107 (75:0.7); 143 (100:0.7); 179 (100:0.56), 213 (100:0.47) and 286 (100:0.35). $Si_2H_6$-deposited films in this study are deposited with R ($H_2$(sccm):$Si_2H_6$(sccm)) of 75 (75:1); 100 (100:1); 125 (100:0.8); and 149 (100:0.67). Figures 9-2a and 9-2b show the Raman spectra of two series of films deposited using $Si_3H_8$ and $Si_2H_6$, respectively.

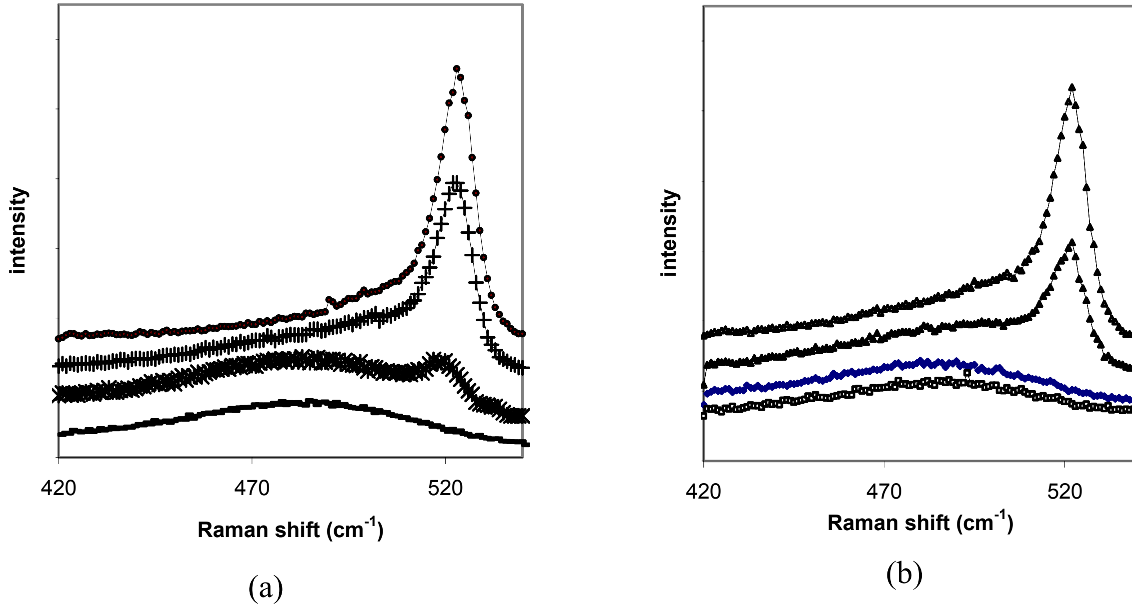


***Fig. 9-2: Raman spectra of the series of sample deposited using $Si_3H_8$ (2a) and $Si_2H_6$ (2b). In Fig. 9-2a, curves from bottom to top are for Si:H deposited with R=143, 179, 213, and 286. In Fig. 9-2b, curves from bottom to top are for a-Si:H deposited with R=75; 100; 125; and 150.***

***Table 9-1: Volume fraction of nanocrystalline silicon phase estimated from Raman spectra for two series of sample. Thicknesses of samples are also included in the Table.***

| Sample No | Gas precursor | Gas flow (sccm) | Ratio R | Thickness (nm) | nc –Si:H volume frac. (%) |
|---|---|---|---|---|---|
| GD1003 | $Si_2H_6$ | 1:75 | 75 | 176 | N.A. |
| GD1002 | $Si_2H_6$ | 1:100 | 100 | 165 | N.A. |
| GD1004 | $Si_2H_6$ | 0.8:100 | 125 | 195 | 13.6 |
| GD1005 | $Si_2H_6$ | 0.67:100 | 149 | 209 | 37.8 |
| GD1010 | $Si_3H_8$ | 0.7:100 | 143 | 234 | N.A. |
| GD1006 | $Si_3H_8$ | 0.56:100 | 179 | 340 | 2.8 |
| GD1009 | $Si_3H_8$ | 0.47:100 | 213 | 261 | 17.7 |
| GD1007 | $Si_3H_8$ | 0.35:100 | 286 | 273 | 57.2 |

Table 9-1 shows the volume fraction of nc-Si:H phase calculated using approaches described in the literature[2]. Fig. 9-2a shows that at R=143, the material is still amorphous while at R=179 formation of a-Si:H/nc-Si:H mixed phase starts. The volume fraction of the nc-Si:H phase calculated from the peak intensity is 2.8%. Therefore, $R_t$ is between 143 and 179 for $Si_3H_8$. For $Si_2H_6$-deposited samples, Fig. 9-2b indicates that $R_t$ is between 100 and 125, lower than that of $Si_3H_8$. It should be noted that Sample GD1006 with R=179 is thicker than other films such as GD1002. Under a high R, thicker a-Si:H is more likely to have nc-Si:H phase [3] It is likely that $R_t$ for Si3H8-deposited films is higher than 179 if the film thickness would be around 170nm (as

in GD1002), which is typical for the i-layer of a-Si:H top component cell in a triple-junction solar cell. As to be described later, solar cells made with $Si_3H_8$ at R=179 showed high $V_{oc}$, indicating that $R_t$ is greater than 179 for Si3H8-deposited films with around 170nm thickness. These Raman studies suggest that R~100 and R~180, for $Si_2H_6$ and $Si_3H_8$, respectively, may be optimum for deposition of a-Si:H solar cell intrinsic layers with thickness around150 to 200 nm.

The films described in Fig. 9-2 and Table 9-1 were also evaluated using Raman with excitation light through the quartz substrates. Such a measurement reveals the structure of the film grown during initial stage of the deposition. Raman scattering measurement show that the a-Si:H materials deposited on glass or quartz substrates during the initial stage of deposition is amorphous for all these samples described in Table 9-1 and Fig. 9-2.

Activation energy $E_a$ was calculated from temperature dependence of dark conductivity using $\sigma=\sigma_0 \exp(-E_a/kT)$. For undoped or n-type a-Si:H, $E_a$ is approximately the energy difference between the Fermi level and the conduction band edge. Fig. 9-3 shows the activation energy as a function of hydrogen dilution R for both $Si_3H_8$- and $Si_2H_6$-deposited samples. For $Si_3H_8$-deposited samples, $E_a$ is decreased from 0.85 eV at low R to 0.5 eV at high R. This decrease is believed to be due to the narrowing of the bandgaps of the deposited materials when there is a higher volume fraction of nc-Si:H phase in the sample. Similar trend is observed for $Si_2H_6$ deposited films. A major difference between the two series of films is that $E_a$ for $Si_2H_6$ samples decreases rapidly when R is increased to 150 while $E_a$ for $Si_3H_8$ samples decreases gradually, over a larger range of R, when R is increased to ~250. The gradual change in $E_a$ with increasing R may suggest that the range of R for the deposition of a-Si:H/nc-Si:H mixed phase is broader. The exact nature for such a difference between $Si_3H_8$ and $Si_2H_6$ is unclear.

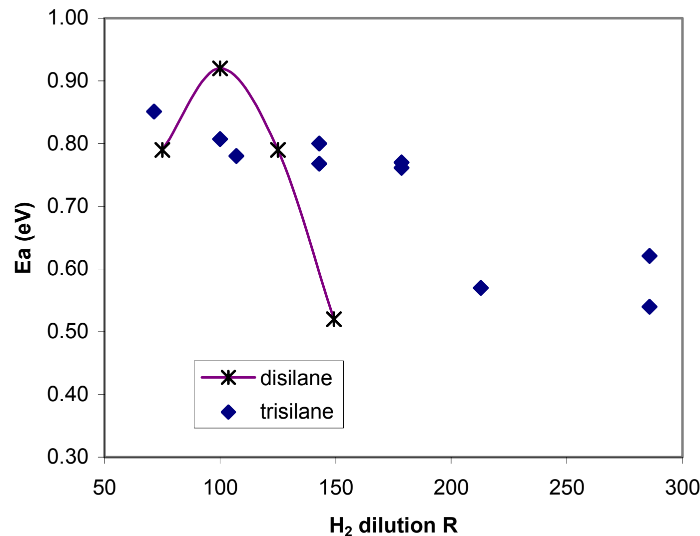


***Fig. 9-3: Activation energy of a-Si:H films made using $Si_2H_6$ and $Si_3H_8$ as a function of hydrogen dilution R.***

Fourier transform infrared spectroscopy (FTIR) was used to measure the content of bonded hydrogen in these Si:H films as well as the amount of hydrogen in different bonding

environment. A microstructure factor, R*, defined as the fraction of hydrogen in dihydride form among all hydrogen incorporated in the film, is calculated from the integrated strength of the $2100cm^{-1}$ peak and $2000cm^{-1}$ peak ($R^* = I(2100\ cm^{-1}) / [I(2100\ cm^{-1}) + I(2000\ cm^{-1})]$).[4] The microstructure factor R* is plotted against dilution R for $Si_3H_8$ and $Si_2H_6$ deposited films in Fig. 9-4.

Fig. 9-4 shows that for both series of films, R* decreases initially and increases again at higher R. The initial decrease is associated with the reduction of undesirable micro-voids in the films. The increase in R* at higher dilution R is believed to be associated with the nc-Si:H formation--hydrogen at grain boundaries bonds to Si mostly in dihydride form. In addition to these general trends, there are noticeable difference in the R* vs R between the two series of films. The increase in R* occurs at a higher R for $Si_3H_8$-deposited films, indicating that $R_t$ is higher for $Si_3H_8$. It is interesting to notice that for films deposited without hydrogen dilution (R=0), R* is lower for $Si_3H_8$ films. This is unexpected because the atomic ratio of H to Si is lower in $Si_3H_8$ than $Si_2H_6$. The lower R* (at R=0) for $Si_3H_8$ suggests that $Si_3H_8$ is dissociated in plasma into a form that is more desirable for the formation of dense a-Si:H. However, one needs to be cautious in drawing a general conclusion based on these results since other deposition conditions such as rf power, chamber pressure, substrate temperature may impact R* at R=0.

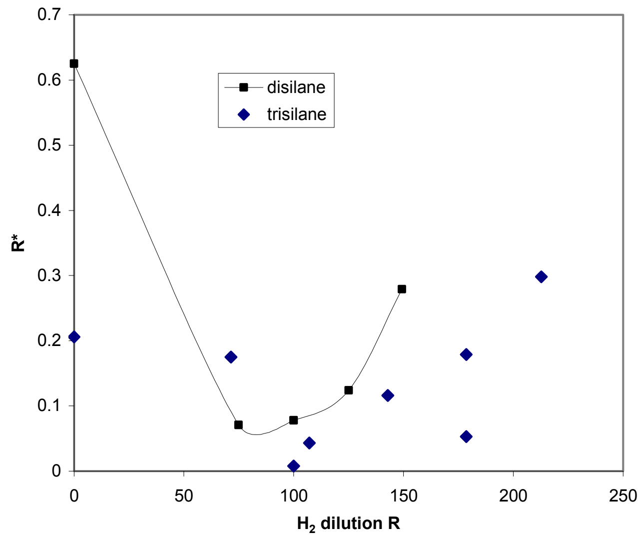


***Fig. 9-4: Microstructure factor R* as a function of hydrogen dilution R.***

Bonded hydrogen content in the Si:H films is estimated from the integrated peak strength of the Si-H wagging mode ($640\ cm^{-1}$). Fig. 9-5 shows the H content in the a-Si:H films for both series. For $Si_2H_6$ samples, H content is approximately 15-20 at.% at R~100. For $Si_3H_8$ samples, H content is approximately 20% at R~150, and decreases down to 6% at R>250. The absolute value of H content depends on the calibration factor used and the values in Fig. 9-5 may not be accurate in the absolute scale. However, relative change in H content is believed to be reproducible.

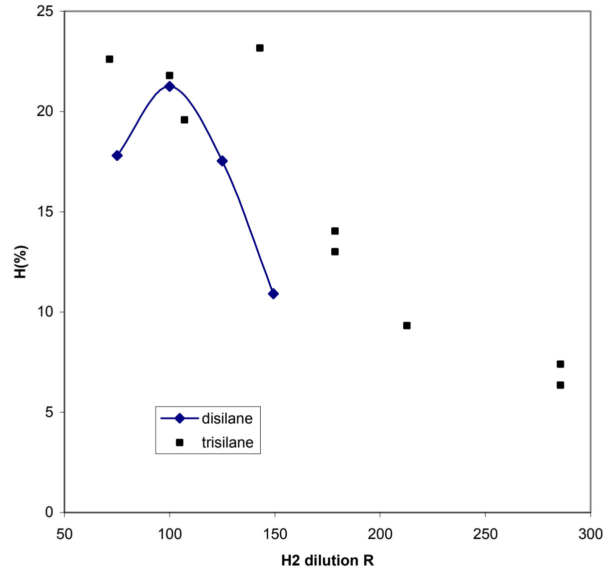


***Fig. 9-5: H content estimated from FTIR spectra as a function of $H_2$ dilution R.***

Fig. 9-6 shows photosensitivity of these a-Si:H films, which is the ratio of photoconductivity under 1 sun illumination and the dark-conductivity. The photosensitivity decreases with increased volume fraction of nc-Si:H phase due to the defects near the grain boundaries. The highest photosensitivity, 1×106, occurs at R~100, or $R_t$, for $Si_2H_6$ samples. The photosensitivity then decreases with increasing R, indicating the increase of nanocrystalline fraction in the material. The highest photosensitivity is nearly the same for the two series of samples. However, the decrease in photosensitivity at $R>R_t$ is more gradual for $Si_3H_8$, similar to the gradual decrease in its activation energy.

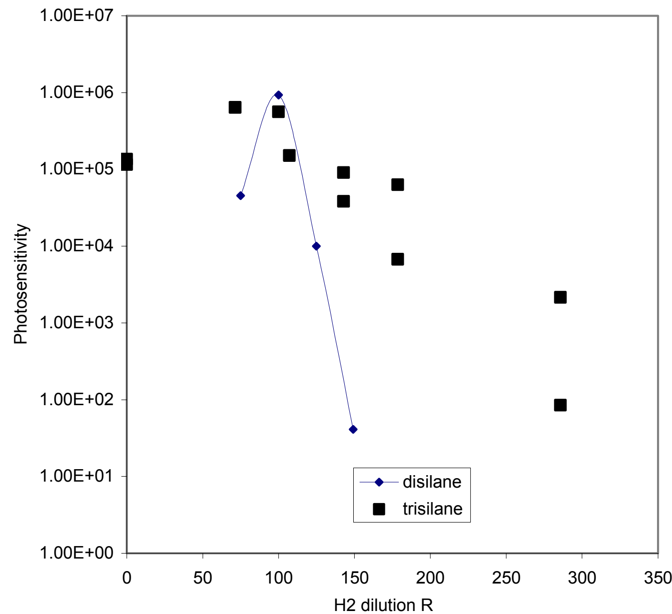


***Fig. 9-6: Photosensitivity of a-Si:H films deposited using $Si_2H_6$ and $Si_3H_8$ as a function of hydrogen dilution.***

Results in Fig. 9-6 indicate that when Si3H8 is used for the deposition of Si, the transition from amorphous to nanocrystalline is more gradual as compared with that for $Si_2H_6$. In other words, the H dilution range for mixed phase is broader when $Si_3H_8$ is used. Material with optimal optoelectronic performance is grown with R~180 at $T_s$~150 °C when $Si_3H_8$ is used. These materials have similar properties to those materials deposited using Si2H6 with R~100.

In order to further verify the findings from this materials study, two series of solar cells were fabricated using $Si_3H_8$ and $Si_2H_6$ with different hydrogen dilution R for the i-layers. When all other device parameters are kept the same, Voc of the solar cells are directly related to the i-layer bandgap. When appropriate level of R is used and the Si:H is near the transition from amorphous to mixed phase, Voc is the highest. At higher R, Voc drops due to the formation of nc-Si:H in the i-layer.

Fig. 9-7 shows the $V_{oc}$ of solar cells as a function of R for i-layers made using $Si_3H_8$ and $Si_2H_6$ at different R. For $Si_2H_6$ devices, $V_{oc}$ reaches its highest value (1.014V) at R~100, while for $Si_3H_8$ devices, $V_{oc}$ reaches its highest value (1.010V) at R~180. These results on solar cell devices are consistent with the findings in the materials study of single-layer films deposited on glass. Both series of solar cells, with ~200nm thick i-layers, were illuminated with white light at 1 sun intensity. After 100 hours of light soaking, $Si_3H_8$ devices degraded 11.7% and $Si_2H_6$ devices degraded 13.2%. These degradations are considered to be the same within experimental variations.

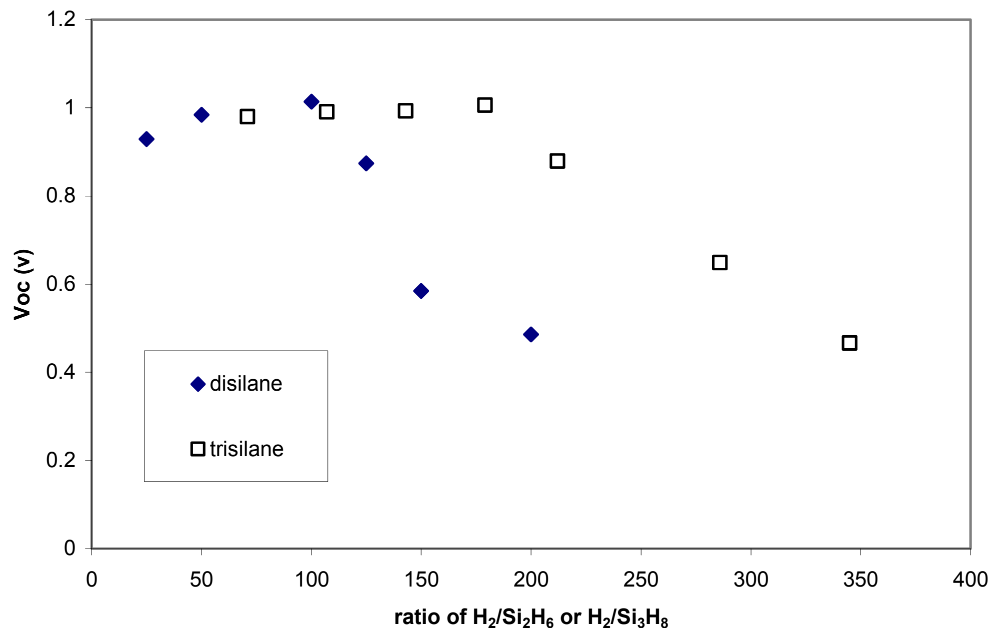


***Fig. 9-7: Open circuit voltage versus $H_2$ dilution for $Si_2H_6$ and $Si_3H_8$ devices.***

## 9.4 SUMMARY

Si:H films and solar cells deposited using $Si_3H_8$ and using $Si_2H_6$ are compared. At the same hydrogen dilution, $Si_3H_8$ leads to higher deposition rate. However, at the same atomic ratio of hydrogen and silicon, the deposition rate of Si:H using $Si_3H_8$ and $Si_2H_6$ is approximately the same. The deposition rate is more influenced by the ratio of the total number of Si atoms to hydrogen atoms introduced into the chamber rather than the number of Si-containing molecules. Measurement of activation energy, microstructure and photosensitivity indicate that 1) the transition from amorphous to amorphous/nanocrystalline mixed phase occurs at a higher hydrogen dilution level when $Si_3H_8$ is used; and 2) the transition from amorphous to mixed phase is more gradual for $Si_3H_8$ as compared with $Si_2H_6$. When appropriate level of R is used and the a-Si:H is near the transition from amorphous to mixed phase, $V_{oc}$ is the highest. At higher R, $V_{oc}$ decreases due to the formation of nc-Si:H in the i-layer. For $Si_2H_6$ devices, $V_{oc}$ reaches its highest value (1.014V) at R~100, while for $Si_3H_8$ devices, $V_{oc}$ reaches its highest value (1.010V) at R~180. These results on solar cell devices are consistent with the findings in the materials study of single-layer films deposited on glass.

### References


1. R. Swanepoel, J physics.E Sci.instrum. Vol 16,1983 p1914-1922.
2. H. Shanks etc. Phys. Stat. Sol (B) 100,43 (1980).
3. A. Ferlauto, R. Koval, C. Wronski, R. Collins, *Appl. Phys. Lett.* **80**, 2666 (2002).
4. M. H. Brodsky, M. Cardona, J. J. Cuomo, Phy. Rev. B 16 (1977) 3556.

# 10 Fine-Grained Nanocrystalline Silicon p-Layer for High-$V_{oc}$ a-Si:H Solar Cells

*Contributors:*

*Univ. of Toledo: Wenhui Du, Xianbo Liao, Xiesen Yang, Xianbi Xiang and Xunming Deng*

*Univ. of Michigan: Kai Sun*

**Abstract**

Amorphous silicon (a-Si:H) single-junction solar cells with high open circuit voltage ($V_{oc}$), up to 1.04 V, are routinely fabricated at the University of Toledo (UT) using a wide bandgap boron doped Si:H p-layer deposited at high hydrogen dilution and low substrate temperature and with a seed layer that promotes nanocrystalline silicon (nc-Si:H) formation.

It is important to understand the exact nanostructure of the p-type material used at UT and other laboratories to produce high-$V_{oc}$ solar cells. In an earlier paper, we reported our preliminary finding that these p-type materials used in UT's high-$V_{oc}$ solar cells are fine-grained nc-Si:H, based on a modeling study using AMPS. In this paper, we report our further investigation of the nanostructure of this p-type material using High Resolution Transmission Electron Microscope (HRTEM), which allows us to directly measure the nanostructure of the films, ~15nm thick, deposited on a-Si substrates. It is found from the HRTEM studies that the p-layer used at UT to obtain high-$V_{oc}$ a-Si solar cells is a mixed-phase material that contains fine-grained nc-Si:H embedded in an a-Si:H matrix. It is further concluded that the mixed phase p-layer with a higher volume fraction of nc-Si:H phase, within the range studied, leads to a higher $V_{oc}$. The optimum p-layer material for nip-type a-Si:H solar cells is neither at the onset of the transition between amorphous to (amorphous and nanocrystalline) mixed phase nor a nanocrystalline/microcrystalline material with a high volume fraction of crystalline phase.

## 10.1 Introduction

Amorphous silicon (a-Si:H) single-junction solar cells with high open circuit voltage ($V_{oc}$), up to 1.04 V, are routinely fabricated at the University of Toledo (UT) using a wide bandgap boron doped Si:H p-layer deposited at high hydrogen dilution and low substrate temperature and with a seed layer that promotes nanocrystalline silicon (nc-Si:H) formation [1]. There are several reports in the literature that provide conflicting suggestions about the structure of a p-type materials deposited under similar conditions [2, 3]. It is important to understand the exact nanostructure of the p-type material used at UT and other laboratories to produce high-Voc solar cells. Unfortunately, it is challenging to obtain results that lead to a definite conclusion since on one hand, the p-layer Si:H material, ~15nm thick, is deposited on an a-Si substrate in an a-Si n-i-p type solar cell and the commonly used methods to determine the nanostructure of these materials require the films to be at least 100nm in thickness and are deposited on glass or crystalline Si substrates while on the other hand, the nanostructure of the thin film Si:H based

material depends sensitively on the substrates and the thickness in addition to the deposition conditions such as hydrogen dilution and substrate temperature. In an earlier paper, we reported our preliminary finding that these p-type materials used in UT's high-Voc solar cells are fine-grained nc-Si:H, based on a modeling study using AMPS [4]. In this paper, we report our further investigation of the nanostructure of this p-type material using High Resolution Transmission Electron Microscope (HRTEM), which allows us to directly measure the nanostructure of the films, ~15nm thick, deposited on a-Si substrates.

## 10.2 Experimental

A-Si:H solar cells are deposited using RF-PECVD on stainless steel covered with an Al/ZnO back reflector. The n- and i-layers are deposited under the conditions reported earlier [1] and these are the same conditions used in the fabrication of high-efficiency triple-junction solar cells at UT [5]. These p-layers are deposited using a high hydrogen dilution, high rf power, and a low substrate temperature, and with a seed layer to promote nanocrystalline Si:H formation.

Raman scattering is performed to characterize the structure of films. The 488-nm laser line from a water-cooled Ar+ laser is used for the excitation. The samples used for Raman study are approximately 350 nm thick and are deposited on glass substrates. Optical transmission is also measured for these samples. Raman spectra are measured from both the front side of the films as well as the back side of films through the glass substrates.

For HRTEM, a Jeol 2010 STEM microscope is used. The samples for the HRTEM study are 15nm-thick boron-doped p-layer deposited on a 15nm-thick intrinsic a-Si:H layer that is grown under the same conditions as the intrinsic layer in a high-Voc a-Si:H solar cell. The Si:H layers, with a combined thickness of 30nm, are first deposited on a glass substrate and then peeled off from the substrates using diluted hydrofluoride acid for the HRTEM measurement.

## 10.3 Results and Discussions

Figure 10-1(a) shows the Raman spectrum of a 350 nm thick p-layer deposited on a glass substrate. The spectrum is deconvoluted into three major peaks, located at 480cm-1, 514 cm-1 and around 500cm-1, corresponding to the amorphous phase, the nanocrystalline phase and the grain boundary interfaces, respectively. According a bond polarizability model [6], a 514cm-1 Raman peak corresponds to a nc-Si with mean nanocrystalline grain size of approximately 2.1 nm. We believe that the actual grain size may be larger than this value since the phonon confinement effect may be overestimated in using this model without considering the existence of tensile stress in the film.[7]

Since the 350nm sample is thicker than the 15nm layer used in an actual solar cell, the nanostructure of the sublayer probed by Raman may have higher volume fraction of nanocrystalline phase than the initial 15nm deposited on the substrate. To effectively measure the nanostructure of the film initially deposited on the substrate, we measured Raman spectra also from the back side of the sample, through the glass substrate. The results are shown in Figure 1b.

Raman spectrum taken through the glass substrate shows a smaller crystalline volume fraction. However, the deconvoluted peaks still shows a 514cm$^{-1}$ Raman scattering peak, indicating the existence of fine-grained nc-Si during the initial growth of the film when it is deposited on glass.

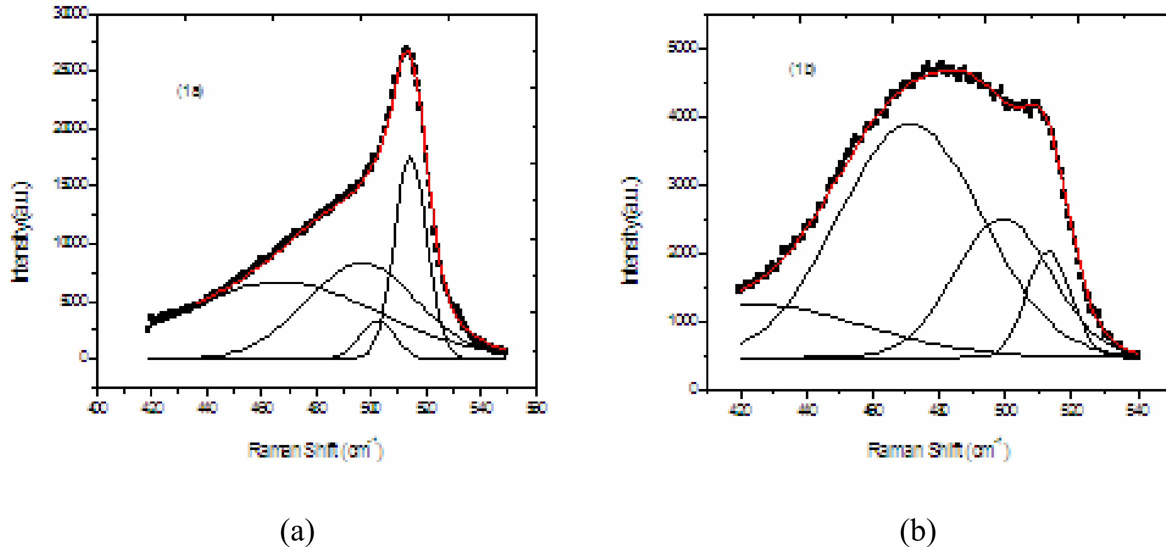


(a) (b)

***Fig.10-1: The Raman spectra taken from (a) the front side surface and (b)the back side of the p-layer through the glass substrate.***

One may still question the results from Raman spectrum obtained through the glass substrate because 1) at 488nm laser line, the Raman scattering may be from the sublayer of the film that is up to 100 nm thick which corresponds to the absorption depth for this laser line; and 2) the initial film is deposited on glass and therefore may have different nanostructure than those films deposited on a-Si substrate as in an n-i-p type solar cell.

In order to characterize the thin p-layer in a solar cell, HRTEM was performed on a 15-nm thick p-layer (Sample A) grown on a 15-nm intrinsic a-Si:H layer, which was deposited under identical conditions as those used in solar cells. Figure 10-2a shows a high-angle annular dark-field (HAADF) image, exhibiting many separated bright dots which are characteristics of nanocrystalline Si. Most of these bright dots, the nc-Si:H grains, have a size of around 3 to 5 nm, which is larger than the size estimated from Raman measurement. Figure 10-2a also shows that several large white dots are the clusters of 3 or 4 crystalline grains. Figure 10-2b is the selected-area electron diffraction (SAED), showing a diffraction pattern with crystalline feature for the area probed.

We deposited another p-layer (Sample B) on a-Si under the same conditions described above but without the seed layer that promotes nc-Si growth. Such a p-layer usually leads to an a-Si:H solar cell with approximately 20mV less in Voc. Fig. 10-2c shows a HAADF image of Sample B, exhibiting smaller volume fraction of nanocrystalline grains. In order to show that these white dots on Samples A and B are indeed nanocrystalline grains, nano-electron diffraction (NED) was measured for one of the bright dots in Fig. 10-2c (a grain in Sample B) and the result is shown in Fig. 10-2d. The interference fringes near the center indicate the white dots

correspond to crystalline structure. Comparing the HAADF images of Samples A and B shown in Fig. 10-2a and Fig. 10-2b, respectively, it is concluded that a p-layer material with higher volume fraction of nc-Si:H phase leads to a higher Voc in an a-Si n-i-p type solar cell.

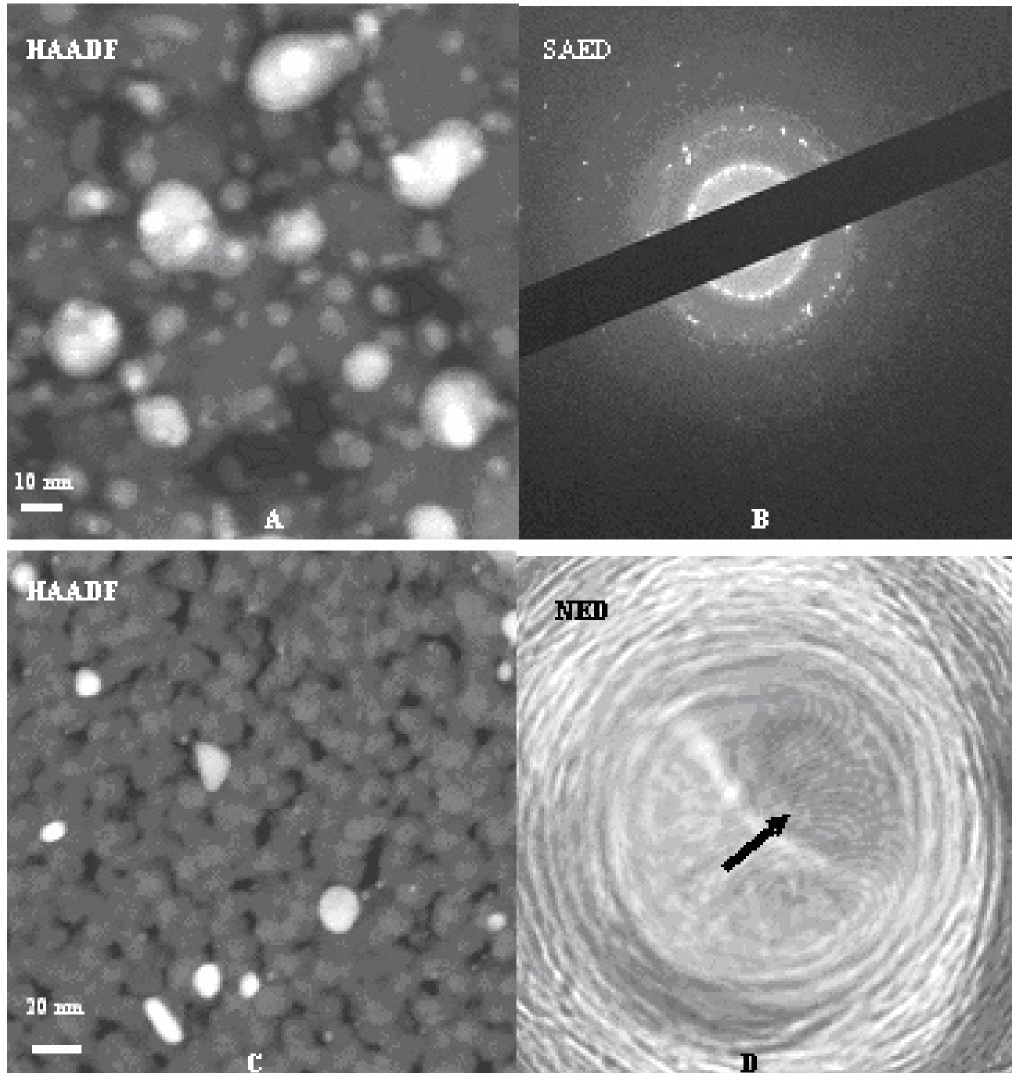


***Fig. 10-2: a) and b) are HAADF and SAED images of the Sample A with a seed layer between the p- and i-layer; c) and d) are HAADF and NED images of the Sample B which has a slightly less Voc.***

Another p-layer, Sample C, was deposited under a similar condition as Sample A but with higher rf power. Raman spectrum measured from both the front and backside on glass shows that this p-layer material is amorphous without any observable nc-Si:H phase. When this p-type material is used in an nip a-Si:H solar cell, it leads to a Voc of 0.98V, less than the p-type materials that contains fine-grained nc-Si:H.

A-Si:H nip solar cells, incorporating above-described nc-Si:H p-layers, are fabricated on stainless steel substrates coated with a Al/ZnO back reflector. The solar cells fabricated using

Sample A deposition conditions for the p-layer show an average Voc of 1.040 V. The cells with the highest performance show a Voc of 1.042 V, a fill factor of 0.734, a short circuit current of 11.6 mA/cm2, and an efficiency of 10.03 %.

## 10.4 Conclusion

The p-layer used at UT to obtain high-Voc a-Si solar cells is a mixed–phase material that contains nc-Si:H grains, ~3-5 nm in size, embedded in an a-Si:H matrix. Comparing HAADF images of two samples (Samples A and B), it is concluded that the mixed phase p-layer with a higher volume fraction of nc-Si:H phase, within the range studied, leads to a higher $V_{oc}$. The optimum p-layer material for nip-type a-Si:H solar cells is neither at the onset of the transition between amorphous to (amorphous and nanocrystalline) mixed phase nor a nanocrystalline/microcrystalline material with a high volume fraction of crystalline phase.

### References


1. X. Deng, Annual Subcontract Progress Report submitted from UT to NREL under Thin Film Partnership Program NDJ-2-30630-08, Phase I Report (2002) and Phase II Report (2003).
2. S. Guha, J. Yang, P. Nath, and M. Hack, Appl. Phys. Lett. 49, 218 (1986).
3. R. J. Koval, Chi Chen, G. M. Ferreira, A. S. Ferlauto, J. M. Pearce, P. I. Rovira, C. R. Wronski, and R. W. Collinsa, Appl. Phys. Lett. 81, 1258 (2002).
4. X. Liao, W. Wang and X. Deng, Proc. 29th IEEE-PVSC, 1234 (2002)
5. W. Wang, H. Povolny, W. Du, X. Liao and X. Deng, Proc. 29th IEEE-PVSC, 1082 (2002).
6. J. Zi, H. Buescher, C. Falter, W. Ludwig, K. Zhang and X. Xie, Appl. Phys. Lett. 69, 200 (1996).
7. V. Paillard, P. Puech, R. Sirvin, S. Hamma and P. Roca i Cabarrocas, J. Appl. Phys. 90, 3276 (2001).

# 11 Hydrogenated Nanocrystalline Silicon *p*-Layer in *a*-Si:H *n-i-p* Solar Cells

*Contributors:*

*Univ. of Toledo: W. Du, X. Liao, X.Yang, H. Povolny, X. Xiang, and X. Deng*

*Univ. of Michigan: K. Sun*

**Overview**

In the Quarterly report (12/1/03-2/28/04), we discussed the dependence of a-Si nip solar cell Voc on the structure of the p-layer, covering the transition from amorphous → protocrystalline → nanocrystalline+amorphous (nc+a) mixed phase. It is concluded that higher $V_{oc}$ is obtained when the p-layer is made with fine-grained nc-Si mixed with a-Si phase. In this Quarterly report, we discuss the dependence of a-Si nip solar cell $V_{oc}$ on the structure of the p-layer, covering the transition from (nc+a) mixed phase → microcrystalline silicon. It is concluded that $V_{oc}$ drops significantly when the microcrystalline silicon p-layer is used.

**Abstract**

This paper investigates the impacts of hydrogenated nanocrystalline silicon (*nc*-Si:H) *p*-layer on the photovoltaic parameters, especially the open circuit voltage ($V_{oc}$) of *n-i-p* type hydrogenated amorphous silicon (*a*-Si:H) solar cells. Raman scattering spectroscopy and transmission electron microscopy (TEM) analyses indicate that this p-layer is a diphasic material that contains nanocrystalline grains with size around 3-5 nm embedded in an amorphous silicon matrix. Optical transmission measurements show that the *nc*-Si *p*-layer has a wide bandgap of 1.96 eV, due to the quantum confinement effects (QCE). Using this kind of *p*-layer in *n-i-p a*-Si:H solar cells, the cell performances were improved with a $V_{oc}$ of 1.042 V, while the solar cell deposited under a similar condition but incorporating a hydrogenated microcrystalline silicon ($\mu c$-Si:H) *p*-layer leads to a $V_{oc}$ of 0.526 V.

## 11.1 Introduction

The limiting factors of open circuit voltage of *a*-Si:H solar cells have been an interesting topic since *a*-Si:H alloys became a viable material for photovoltaic devices. Theoretical considerations expected that recombination originating from band tail states puts a fundamental limit on the output voltage of *p-i-n a*-Si:H solar cells, and the maximum $V_{oc}$ calculated from the difference between the electron and hole quasi-Fermi levels in the intrinsic (*i*) layer is 1.0 ± 0.1 V.[1] Experimentally, using high hydrogen dilution or hydrogen-plasma treatment, *a*-Si:H solar cells with $V_{oc}$ greater than 1.0 V could be fabricated,[2,3] which is well consistent with the above theoretical estimation.

However, it is noted that this estimate holds only for the situation when the built-in-potential in the *i* layer, set up by the doped (*p* and *n*) layers, is greater than the difference between the electron and hole quasi-Fermi levels. In fact, the doping layers, especially the *p*-layer acting as a window layer in both superstrate and substrate structures, have great influences on $V_{oc}$ available in practical devices.

It was reported that using a *μc*-Si:H *p*-layer in *a*-Si:H *n-i-p* cells with a substrate structure on stainless steel (SS), the cell performance could be improved through an increase in the built-in potential of the junction and a decrease in the series resistance.[4] However, using a *μc*-Si:H *p*-layer in *a*-Si:H *p-i-n* cell with a superstrate structure on $SnO_2$ coated glass, it could induce a disastrous effect on the open circuit voltage and the fill factor (*FF*).[5] In a recent report, R. J. Koval *et al* argued that 10-20 nm thick *p*-layers prepared on *i*-layers under certain conditions may be amorphous even at hydrogen dilution values as high as 200, due to a possible barrier for microcrystal nucleation on an amorphous *i*-layer surface.[6] Moreover, they proposed that the maximum $V_{oc}$ is obtained by incorporating *p*-type doped Si:H layers that are protocrystalline in nature, and even relatively low substrate-induced microcrystalline fractions in the *p*-layer are detrimental.[6]

The question is why the use of a microcrystalline *p*-layer is detrimental for *a*-Si:H cell performances? An explanation was that this is due to the narrow bandgap ($E_g$) of *μc*-Si:H *p*-layer and a barrier at the *p/i* interface caused by the band offset between microcrystalline *p*-layer and amorphous *i*-layer.[5] This suggestion was confirmed by our simulation results,[7] using AMPS model developed at Penn State University.[8] Indeed, a "good" *μc*-Si:H *p*-layer with a large mean grain size (i.e., greater than 20 nm) and a large crystalline fraction should have a bandgap close to ~1.1 eV, the one of bulk crystalline silicon. However, if we could make a *μc*-Si:H *p*-layer with a wide bandgap, what will happen to the cells? And how can we make such a *p*-layer? One way to achieve a wide band gap *p*-layer is to use the QCE, i.e., to make *μc*-Si:H which comprise small Si nanocrystals embedded in an amorphous Si-H matrix. In this case the energy bangap of *μc*-Si:H should be enlarged by the QCE. In the following we prefer to use the term "nanocrystalline silicon", instead of "microcrystalline silicon" for such a kind of material. On the basis of the foregoing considerations it is appropriate in the present letter to identify the different effects of *nc*-Si:H and μc-Si:H *p*-layers on the performances of *a*-Si:H *n-i-p* cells.

## 11.2 Experimental

The p-layer samples were prepared using conventional rf (13.56 MHz) PECVD and a gas mixture of SiH4, BF3 and H2 in an ultrahigh-vacuum, multi-chamber, load-locked deposition system. For growing nc-Si:H p-layers we used a high hydrogen dilution ($H_2/SiH_4$=166) and a high gas pressure of 2 Torr as well as a high power density of 1.0 W/cm$^2$ at a low substrate temperature of 70 °C. To increase microcrystallinity in the μc-Si p-layers, the deposition parameters were changed to a higher hydrogen dilution ($H_2/SiH_4$=200), a low gas pressure of 0.6 Torr as well as a low power density of 35mW/cm$^2$ at 200 °C. Samples for use in a-Si:H n-i-p cells have a structure of SS/Al/ZnO/n-a-Si:H/i-a-Si:H/p-Si:H/ITO, with a protocrystalline i-layer deposited using a gas mixture of Si2H6 and H2 at a high hydrogen dilution ($H_2/Si_2H_6$=100) at 200°C. To enhance the formation of nanocrystalline nucleation sites for the p-layer deposition,

we inserted a seed layer between the p- and i-layer in the samples. For analyses of the optical and structural properties the p-layer samples were deposited on Corning 7059 glass using the identical conditions as used in the solar cells, but with different deposition times. The formation of silicon nanocrystals and their mean grain size in the samples were characterized by Raman scattering and TEM. In view of the fact that microcrystalline growth is sensitive to the substrate material and the accumulated thickness,9 we also made a thin sub-seed and i-layer (15 nm) before the p-layer deposition on Corning 7059 glass, simulating the p/i interface structure of the cell samples, and took the Raman signals from both sides, the front surface and the back surface through the glass substrate.

### 11.3 Results and Discussions

The obtained Raman spectra for the *nc*-Si:H and μc-Si:H *p*-layer samples are given in Fig.1, which were recorded near backscattering geometry using an $Ar^+$ laser operating at a wavelength of 488 nm and a double monochrometer in the silicon TO mode region. Curve (a) of Fig.1 shows the Raman spectrum of the μc-Si *p*-layer sample (~50 nm thick). This curve has a sharp peak at 521 $cm^{-1}$, which is typical for bulk crystalline Si. Curve (b) and (c) of Fig.1 are the spectra of the *nc*-Si:H *p*-layer sample (~350 nm thick), taken from the front surface and the back surface through the glass substrate, respectively. As generally observed with *nc*-Si:H, two peaks appear in the spectra, a broad peak at 480 $cm^{-1}$, which is characteristic of amorphous Si and a sharp peak at 514 $cm^{-1}$, which is characteristic of Si nanocrystals. It is seen that Curve (b) is dominated by the sharp peak at 514 $cm^{-1}$, while Curve (c) comprises a broad peak at 480 $cm^{-1}$ and a small shoulder at ~514$cm^{-1}$, demonstrating the reported dependence of crystallinity on the accumulated thickness.[9] The Gaussian deconvolution of the two Raman spectra data are listed in table 1, including the peak position ($P_k$), the peak area (A) of the TO modes and the volume crystalline fraction (C), which was determined using the ratio of peak area of crystalline to that of amorphous inclusions with a cross section ratio of 0.9.[10] As can be seen that the Raman spectrum taken from the backside shows a less volume crystalline fraction, although it has nearly the same Raman redshift of 7 $cm^{-1}$ with respect to the TO phonon mode in bulk crystalline Si. From this Raman redshift, we deduced the mean nanocrystal size to be 2.1 nm or 2.5 nm, according to a bond polarizability model of J. Zi *et al.*,[11] or a modified phonon confinement model of Campbell and Fauchet.[12,13] These estimated sizes might be smaller than the actual sizes, due to an overestimate of the phonon confinement effect without considering the existence of tensile stress in the film.[14]

***Table 11-1: Gaussion deconvolution of the Raman spectra of Curve (b) and Curve (c) in Fig.1, including the peak position ($P_K$) and the peak area (A) of the TO modes for crystalline ($TO_c$), amorphous ($TO_a$) and interfacial ($TO_i$) inclusions. The volume crystalline fraction (C) is also listed.***

| | $TO_c$ | | $TO_i$ | | $TO_a$ | | C |
|---|---|---|---|---|---|---|---|
| nc-Si p-layer | Pk($cm^{-1}$) | A(a.u.) | Pk($cm^{-1}$) | A(a.u.) | Pk($cm^{-1}$) | A(a.u.) | |
| Top surface | 514.2 | 87653 | 500.1 | 51031 | 480.2 | 194436 | 0.44 |
| Back surface | 514.0 | 52662 | 500.6 | 70339 | 480.3 | 228673 | 0.37 |

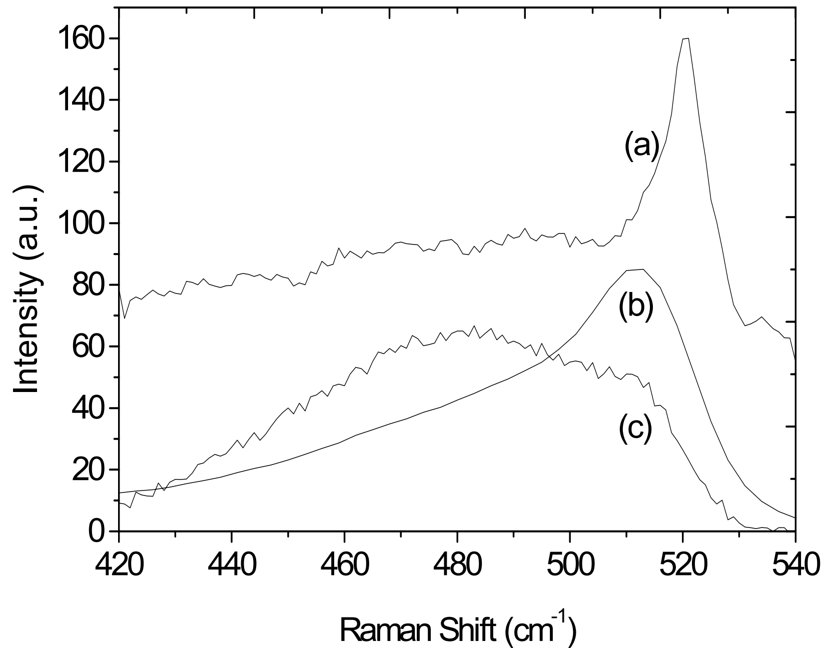


***Fig. 11-1: Raman spectra of the μc-Si:H p-layer (Curve a) and the nc-Si:H p-layer samples taken from the front surface (Curve b) and the back surface (Curve c) th***

In order to characterize the crystallization in a very thin p-layer, a JEOL 2010F STEM/TEM microscope was used. The films were lifted off from glass substrate by etching with a diluted HF solution and supported by a copper TEM grids. The thin p-layer sample has a hybrid, stacked structure, comprising a 15 nm thick p-layer on a 15 nm i-layer with a seed layer in between, which was deposited under identical conditions as those used in solar cells. Fig. 11-2(a) shows a high-angle annular dark-field (HAADF) image of the sample, where many separated bright dots were observed, which represent nanocrystalline particles. Most of the particles are ranging from 3 to 5 nm, larger than the estimated values from Raman study. Several large white dots in this figure are the clusters of 3 or 4 crystalline particles. In the insert a selected-area electron diffraction (SAED) is illustrated, indicating diffraction pattern with crystalline feature for the area probed. Fig. 11-2(b) shows a high-resolution electron microscopy (HREM) image, exhibiting the lattice image. The interference fringes separated by 0.31 nm correspond to the spacing of Si (111) planes of the nanocrystals. Fig. 11-2 (c) is a nano electron diffraction (NED) taken from one of the bright dots indicating the crystalline nature of the particle. These images clearly demonstrate that the p-layer deposited at a low substrate temperature and a high hydrogen dilution contains nanocrystalline Si particles of 3-5 nm in size. We estimated the effective energy bandgap of these Si nanocrystals should be enlarged to 2.3-1.9 eV, if it is treated as isolated spherical quantum dots saturated with hydrogen, based on the density-function approach of B. Delley and E.F. Steigmeier.[15] In fact the optical transmittance measurements performed on the same nc-Si:H p-layer sample used in the Raman scattering (Fig. 11-1) show that its Tauc optical bandgap is about 1.96 eV, confirming that the nc-Si:H p-layer indeed possesses a wide bandgap. However, one could not simply compare the Tauc bandgap

value with the above theoretical estimate, because the former is an effective bandgap width of a diphasic material with an indirect gap, while the latter is for isolated Si quantum dots.

Effectiveness of a thin nc-Si:H p-layer for a solar cell can be most convincingly judged in a cell configuration. We prepared n-i-p a-Si:H solar cells at a similar condition but using a nc-Si:H or μc-Si:H p-layer. The resultant typical I-V curves are demonstrated in Fig.3. It is observed that using a nc-Si:H p-layer the cell performances (Curve a) could be enhanced, with a $V_{oc}$ of 1.042 V, a FF of 0.734, a short circuit current of 11.6 mA/cm$^2$, and an efficiency of 8.87 %, while incorporating a μc-Si:H p-layer into the cell (Curve b ), the $V_{oc}$ decreased to 0.526 V.

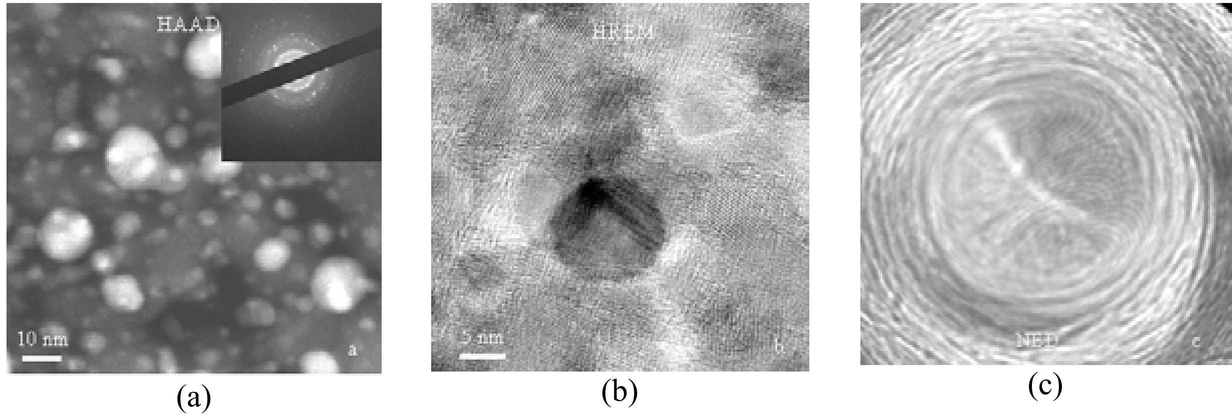


***Fig. 11-2: TEM micrographs of a thin nc-Si:H p-layer of 30 nm thick with a hybrid, stacked structure. (a) HAADF image, where bright dots represent nanocrystalline particles; in the insert is a SAED image, showing the diffraction pattern with crystalline features; (b) HREM image, exhibiting the lattice image; (c) Nano electron diffraction (NED) taken from one of the bright dots indicating the crystalline nature of the particle.***

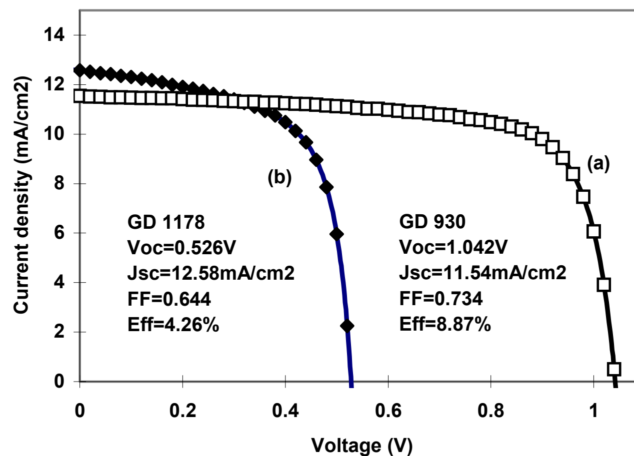


***Fig. 11-3: I-V characteristics of n-i-p a-Si:H solar cells on SS coated with Al/ZnO using the nc-Si:H p-layer (Curve a) or μc-Si:H p-layer into the cell (Curve b )***

**References:**


1 T. Tiedje, Appl. Phys. Lett. 40, 627 (1982).
2 B.Yan, J. Yang, and S. Guha, Appl. Phys. Lett. 83, 782 (2003).
3 S. Tsuge, Y. Hishikawa, S. Okamoto, M. Sasaki, S. Tsuda, S. Nakano, and Y. Kuwano, Mat. Rec. Soc. Symp. Proc. 258, 869(1992).
4 S. Guha, J. Yang, P. Nath, and M. Hack, Appl. Phys. Lett. 49, 218 (1986).
5 J. K. Rath, and R. E. I. Schropp, Solar Energy Materials and Solar Cells 53, 189(1998).
6 R. J. Koval, Chi Chen, G. M. Ferreira, A. S. Ferlauto, J. M. Pearce, P. I. Rovira, C. R. Wronski, and R. W. Collins, Appl. Phys. Lett. 81, 1258 (2002).
7 X. Liao, W. Wang and X. Deng, Proc. 29th IEEE-PVSC, 1234 (2002).
8 For AMPS, see http://www.psu.edu/dept/AMPS/.
9 Joohyun Koh, A. S. Ferlauto, P. I. Rovira, C. R. Wronski, and R. W. Collins, Appl. Phys. Lett. 75, 2286 (1999)
10 G. Yue, J. D. Lorentzen, J. Lin, D. Han, and Q Wang, Appl. Phys. Lett. 75, 492 (1999).
11 J. Zi, H. Buescher, C. Falter, W. Ludwig, K. Zhang and X. Xie, Appl. Phys. Lett. 69, 200 (1996).
12 Ch. Ossadnika, S. Veprek, and I. Gregora, Thin Solid Films 337, 148 (1999).
13 I. H. Campbell, P.M. Fauchet, Solid State Commun. 58, 739 (1986).
14 V. Paillard, P. Puech, R. Sirvin, S. Hamma and P. Roca i Cabarrocas, J. Appl. Phys. 90, 3276 (2001).
15 B. Delley and E.F. Steigmeier, Phys. Rev. B 47, 1397 (1997).

# 12 Modeling of Triple Junction a-Si Solar Cells Using ASA: Analysis of Device Performance under Various Failure Scenarios

*Contributors: Chandan Das and Xunming Deng*

**Abstract**

Triple junction a-Si solar cells have been modeled and simulated using the Advanced Semiconductor Analysis (ASA). The device performance is analyzed with numerically simulated I-V characteristics. We have studied several failure scenarios such as variations in the thickness of different layers of the multilayered triple-junction structure. Distinctive features of the I-V characteristics and solar parameters have been found which have been correlated and discussed with the basis of device physics.

## 12.1 Introduction

Manufacturing activities of amorphous silicon (a-Si) based thin film solar cells have experience a significant increase in the recent years. Solar panels with triple-junction spectrum-splitting structure are being manufactured in high-volume production. In the fabrication of an a-Si/a-SiGe/a-SiGe nip/nip/nip triple cell, the thickness, bandgap and other properties of each of the nine semiconductor layers as well as the other non-semiconductor layers need to be accurately controlled in order for a triple cell to produce its highest power output. An unintentional change, or a "failure", of any one of these layers could lead to undesirable changes in the solar cell I-V characteristics and quantum efficiency. These changes are often abnormal and difficult to understand.

Modeling of triple junction solar cells and numerical simulation of variation in layers to reproduce the effect of variations in the deposition sequence could help to predict the changes in behavior of the solar cell performance. These predicted results would be extremely helpful to readily point out the failure mechanism by eliminating a large number of possibilities, should any of these failures occur in solar cell fabrication including PV manufacturing. Unfortunately, no reports of comprehensive study of failure analysis for the fabrication of multiple-junction solar cells and/or the comparison of these predicted results with real multi-junction devices have been found. To assist the optimization of solar cell fabrication and cost-effective industrial photovoltaic production, there is a strong need for the study of various possible failure scenarios in the deposition steps associated with the fabrication of multilayered thin film solar cells. In the present work, we selected a number of failure mechanisms that may occur during triple-cell device fabrication and studied the numerically simulated current-voltage (I-V) characteristics using Advanced Semiconductor Analysis (ASA), a program developed by Technical University of Delft.[1] Deviated solar cell I-V characteristics predicted under various failure scenarios are compared to that of a normal case. In the future, we will report cross examination and verification of these predicted I-V performance with that of real triple-junction solar cell devices intentionally fabricated under these failure scenarios.

## 12.2 Modeling

A triple junction a-Si solar cell has been constructed in computer modeling with ASA. The cell has the following structure: Al/n-bottom/i-buffer/i-bottom/i-buffer/p-bottom/n-middle/i-buffer/i-middle/i-buffer/p-middle/n-top/i-top/p-top/TCO and the schematic diagram of this cell is given in Fig. 12-1. This structure is taken as the standard for the present study and its simulated I-V characteristic is designated as the normal case. The other different cases chosen for the present study are shown in the Table 1. When any one layer is varied, all other layers have been kept unchanged in each of these scenarios.

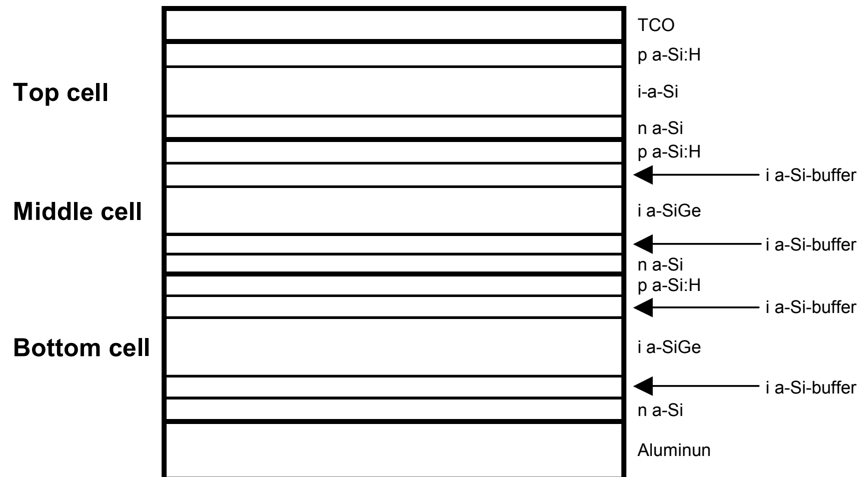


***Fig. 12-1: Schematic diagram of the modeled triple junction solar cell.***

***Table 12-1: Description of different simulation cases for the triple junction solar cells studied in the present work.***

| | | **Cases** (In the parenthesis, corresponding Fig. 12-sub-numbers are given) | |
|---|---|---|---|
| **n-layer** | Top cell | No layer [A1] | Five times more thickness [A2] |
| | Middle cell | No layer [B1] | Five times more thickness [B2] |
| | Bottom cell | - | - |
| **p-layer** | Top cell | - | - |
| | Middle cell | No layer [C1] | Five times more thickness [C2] |
| | Bottom cell | No layer [D1] | Five times more thickness [D2] |
| **i-layer** | Top cell | 10nm / 1nm layer [E1] | Five times more thickness [E2] |
| | Middle cell | - | - |
| | Bottom cell | 10nm layer/ no buffer layers [F1] | Five times more thickness [F2] |

## 12.3 Results and discussion

In Fig. 12-2, the dark and illuminated I-V characteristics of all these cases obtained from ASA simulation are shown; the figure sub-numbers correspond to the designated cases in the parenthesis in Table 1. The dark and illuminated I-V characteristics are presented by dotted and solid curves. In the "normal case" studied here, the device shows a I-V characteristics of $V_{oc}$=2.1V, $J_{sc}$=7.2 mA/cm$^2$ and FF=0.60 and the triple-cell current is limited by that of the middle cell under AM1.5 spectrum at the maximum power point. In Case A1, when we skip the n-layer of top cell, $V_{oc}$ drops to 1.4V and short circuit current ($J_{sc}$) remains almost the same with a slight increase. The lack of the top-cell n-layer leaves the triple junction structure as Al/n-bottom/i-buffer/i-bottom/i-buffer/p-bottom/n-middle/i-buffer/i-middle/i-buffer/p-middle/—/i-top/p-top/TCO, which has low $V_{oc}$ due to the lack of one functioning n-i-p diode. On the other hand, thicker n-layer (Case A2) reduces the $J_{sc}$ to 4.78 mA/cm$^2$ due to the reduced number of photons absorbed by the current-limiting middle cell, while the $V_{oc}$ stays unchanged.

In Case B1 where middle cell n-layer is skipped, the $V_{oc}$ drops to 1.42V and the FF drops to 0.49 while the $J_{sc}$ remains unchanged. In addition, the I-V characteristic becomes S-shaped with suppressed increase in $J_{sc}$ under forward bias. Further, the dark I-V characteristics shows no switching on of diode operation under forward bias. However, for the thicker middle cell n-layer (B2), no prominent variation is noticed except the reduction of FF to 0.58. We choose not to discuss the modeled results of the effect of the bottom cell n-layer in this report, since the effect of the variation of this layer's thickness depends sensitively on the choice of layer underneath, which is aluminum metal layer in the present study. For a similar reason, the effect of top-cell p-layer is also not discussed in this report.

When the middle-cell p-layer is skipped (C1), $V_{oc}$ is reduced as expected. However, in the case of thicker middle-cell p-layer (C2), we observe a peculiar I-V characteristics along with variation in $J_{sc}$, $V_{oc}$, and FF. It appears that under near open-circuit conditions, it is difficult for photo-generated holes to move from the middle-cell i/p interface to the (middle-p)/(top-n) tunnel junction, causing reduced triple-cell current (the kink in the light IV near 1.8V). Similar results are obtained in Cases D1 and D2 where bottom cell p-layer is skipped and made thicker, respectively. The only difference is that the behavior of dark I-V characteristic is different in D1 from that in C1.

In Case E1, where the thickness of the top-cell i-layer is decreased to 1 nm from its 40nm standard case, unexpected results in I-V characteristics has been obtained. In short-circuit condition, the current is diminished while with increase in forward bias (i.e. under loaded condition) current shows an increase. To understand this strange behavior, a case with the thickness of the top-cell i-layer being 10nm was simulated and the peculiar I-V characteristics is also observed, but with less pronounced features. This peculiar IV performance, observed only for much reduced thicknesses than the normal conditions, is not well understood and requires further study. With a top cell i-layer five times thicker (E2) than that of standard, a decrease in $J_{sc}$ is obtained due to the reduced light absorbed by the middle cell which is limiting the current. The $V_{oc}$ and the shape of the I-V characteristic remain unchanged. In Case E2, there is also an artificial increase in FF due to the increased current mis-match.

In the Cases F1 & F2, we varied the bottom cell i-layer thickness. The $J_{sc}$ is significantly reduced when the bottom cell i-layer is made only 10nm in thickness with both of the buffer layers skipped (Case F1). For Case F2, the thicker bottom-cell i-layer results in almost no change in triple-cell IV, since the $J_{sc}$ is still limited by the middle cell.

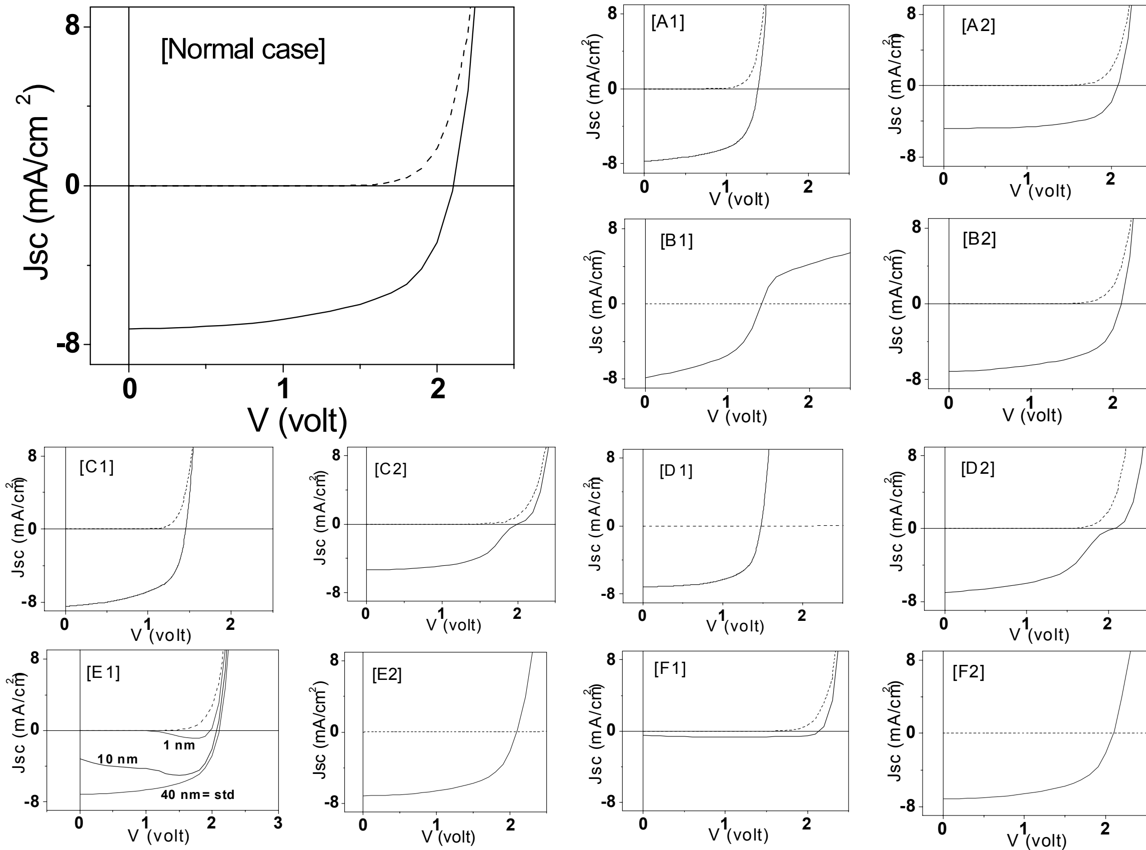


***Fig. 12-2: ASA generated I-V characteristics of the standard triple junction solar cell (Normal case) and cases designated in Table 1 as A1, A2, B1, B2, C1, C2, D1, D2, E1, E2, F1, and F2.***

## 12.4 Conclusion

Using ASA generated I-V results of a normal triple-junction a-Si/a-SiGe/a-SiGe solar cell and those under various "failure" conditions, we analyzed the expected and unexpected IV characteristics when one of the doped or undoped layers is made thicker (five times thicker) or thinner (zero thickness or significantly reduced thickness). Various IV performances are predicted under these failure scenarios. These findings and analyses can be used to assist fabrication of triple-junction a-Si bases solar cells in both research and manufacturing to quickly identify possible failure scenarios, should any of these occur.

**Reference:**

1. R. Schropp and M. Zeman, Amorphous and Microcrystalline Silicon Solar Cells, Modeling, Materials and Device Technology, Kluwer Academic Publishers,1998. Part II.

# 13 Measurement of Component-Cell Current-Voltage Characteristics in a Tandem-Junction Two-Terminal Solar Cell

*Contributors: Chandan Das, Xianbi Xiang and Xunming Deng*

**Abstract**

A new method for measuring component cell current-voltage (I-V) characteristics in a tandem-junction two-terminal solar cell is described. The measurements are performed with (a-Si/a-SiGe) tandem structure solar cell using two separate light beams of different wavelengths. The I-V characteristics of the component cells are obtained and open-circuit voltage ($V_{oc}$), short-circuit current ($I_{sc}$) and fill-factor (FF) are calculated. This method could be a useful tool for evaluation and optimization of multijunction solar cells.

**Keywords**

Measurement method, I-V characteristics, component cells, tandem junction, solar cells

## 13.1 Introduction

In the course of fabricating and optimizing multiple-junction, two-terminal solar cells, it is important to be able to determine the performance of the individual component cells, since a separate single cell, even fabricated under the same conditions, may perform differently from the corresponding component cell within a multiple junction stack. Some differences are reproducible, such as those due to differences in the sub-structure; however, other differences can arise from unrecognized or uncontrolled parameters. The latter is particularly true for production processes insofar as all cells fabricated under identical conditions should have identical performance, but from time to time, are different due to unrecognized parameter variations. Sometimes there are even unidentified catastrophic changes. Without a technique to measure component cell performance in the multiple-junction stack, one could not identify immediately which of the component cells failed or degraded and, therefore, important production time for a multijunction device manufacturer would be wasted. Kurtz et. al. [1] developed a process to measure component cells in a tandem device. However, these approaches call for an initial estimate of the component cell $V_{oc}$. If the initial estimate is not accurate, different results may be obtained. Thus, the applicability of this method is limited. In this work, we report the use of a new technique developed at the University of Toledo [2] to measure component cell I-V in a tandem stack without any initial assumptions.

## 13.2 Outline of Methodology

In order to extract the information about current of a component cell in a tandem stack, where the components cells rely on spectrum-splitting absorption, one could easily make the

tandem current limited by one component cell, by flooding the other component cell with a proper color of light. Thus under such a condition, the current of the one component cell could be measured and I-V could be drawn. However, to get information about individual voltage of each component, there is no such direct way and in a two terminal device structure, voltage is always measured as the sum of the two component voltage. Therefore, the challenge is to get the information about the contribution of voltage from each component in the total tandem voltage. The following procedure deals with this problem.

The procedures for measuring component-cell I-V characteristics consist of two major parts: 1) measurement of open circuit voltage ($V_{oc}$) of each of the component cells inside a tandem cell; and 2) measurement of the short circuit current ($I_{sc}$) and fill factor (FF) of the component cells.

To illustrate the measurement procedures, we describe in detail the measurement of top component cell in a two-terminal, tandem-junction a-Si/a-SiGe solar cell.

Step 1: Measurement of $V_{oc}$ of each of the component cells under a given illumination.

This step consists of several sub-steps:

1A) Measure the relationship between $V_{oc}$ (top) and $I_{sc}$ (top) for the top component cell;
1B) Measure the relation between $V_{oc}$ (bottom) and $I_{sc}$ (bottom) for the bottom component cell;
1C) Measure $I_{sc}$ (top) and $I_{sc}$ (bottom) under a given illumination;
1D) Obtain the $V'_{oc}$ (top) and $V'_{oc}$ (bottom) from the calibration curves generated in Steps 1A and 1B for the top and bottom cells under the given illumination corresponding to the $I_{sc}$ values obtained in Step 1C; and
1E) Compare [$V'_{oc}$ (top) + $V'_{oc}$ (bottom)] with the measured $V_{oc}$ (tandem) to obtain $V_{oc}$(top) and $V_{oc}$ (bottom) under this given illumination.

Step 2: Measurement of $I_{sc}$ and FF of component cells:

2A) Keep the tandem cell under top-cell current limiting condition, i.e., stronger red illumination and relatively weaker blue illumination and scan the I-V of the tandem cell.
2B) Subtract the voltage of the tandem cell with $V_{oc}$ of the bottom cell, obtained above, for this given illumination. Replot the I-V curve of the tandem cell, after $V_{oc}$(bottom) is subtracted, under the illumination in which the tandem-cell current is limited by that of the top cell. This replotted curve is the I-V characteristics of the top component cell.
2C) Keep the tandem cell under bottom-cell current limiting condition and repeat these steps to obtain the bottom cell I-V characteristics.

### 13.3 Description of the Procedures and Results

Step 1A: At first, to make sure that the relationship between $V_{oc}$ and $I_{sc}$ of an a-Si or a-SiGe cell is independent, or weakly dependent at most, on the wavelength of the illumination, single-junction a-Si and a-SiGe cells are used and measured under various monochromatic lights. It is found that the $V_{oc}$ vs $I_{sc}$ curves are indeed independent of the wavelength of the illumination as shown in Fig. 13-1 and Fig. 13-2 for top and bottom single junction cells, respectively. In the discussions afterward, all measurements are carried out in a two-terminal tandem structure. The quantum efficiency (QE) of the a-Si/a-SiGe tandem cell is measured using a method developed by Burdick and Glatfelter [3]. The tandem cell is illuminated with a blue light; a 400 nm monochromatic light is used in this measurement so that the blue light is fully absorbed by the top cell and the bottom cell is in dark. Fig. 13-3 shows that the bottom-cell QE at 400nm is zero. Under the 400 nm blue light, the bottom cell is in dark and does not contribute to the tandem cell $V_{oc}$. Extreme care was taken to make sure that there is no scattered red light near the sample. The $V_{oc}$ of the tandem cell, therefore, is approximately the $V_{oc}$ of the top cell, $V_{oc}$ (top), under this 400 nm light. The current of the tandem cell is, however, limited by the current of the bottom cell. To measure the current of the top cell, a relatively more intense red bias light, obtained from a tungsten lamp with a 610 nm long-pass filter, is illuminated on the tandem cell so that the current of tandem cell is limited by the top cell. By taking the difference of the tandem-cell $I_{sc}$ with and without the 400 nm blue light, the $I_{sc}$ of the top cell, $I_{sc}$ (top), under this particular 400 nm light is obtained. Varying the intensity of the 400 nm blue light, the relationship of $V_{oc}$ (top) and $I_{sc}$ (top) is obtained, as shown in Fig. 13-4. It is possible that the $V_{oc}$ (top) vs $I_{sc}$ (top) relationship shown in Fig. 13-4 is slightly different from the actual relationship since there might be a small contribution of the voltage from the bottom cell under 400 nm light.

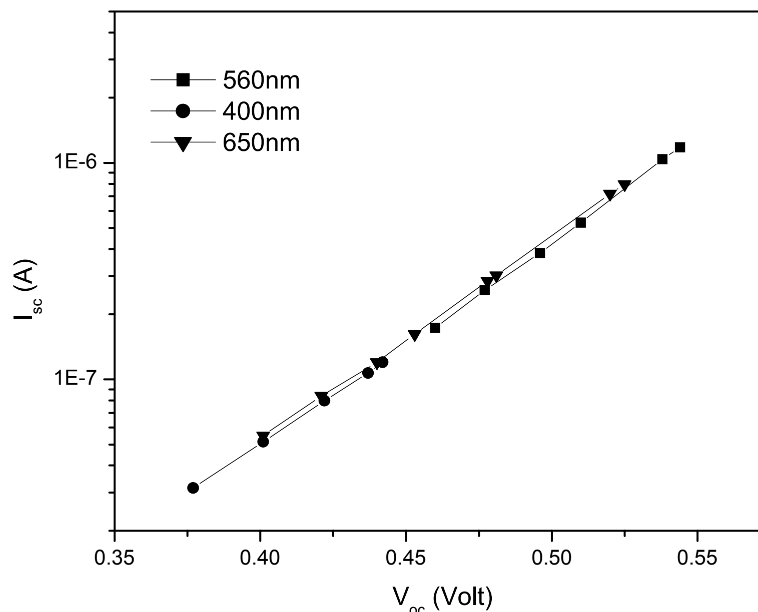


***Fig. 13-1: Relationship between $V_{oc}$ and $I_{sc}$ of single junction top cell under intensity variation of different wavelength of monochromatic light.***

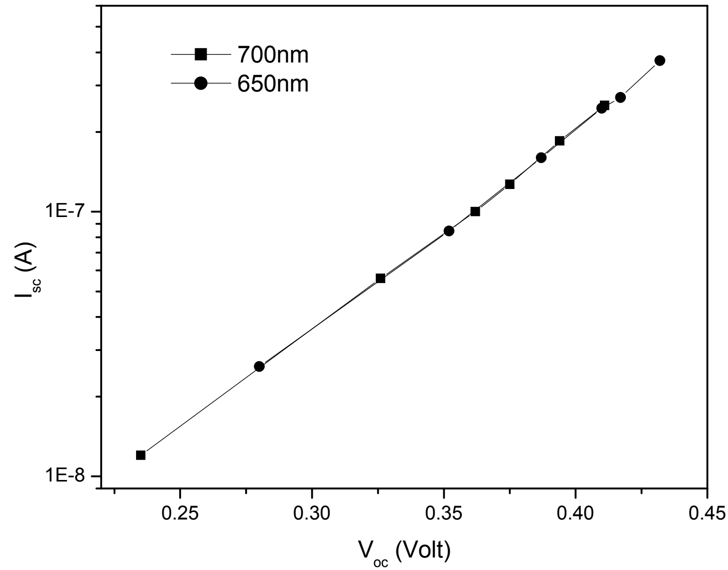


***Fig. 13-2: Relationship between $V_{oc}$ and $I_{sc}$ of single junction bottom cell under intensity variation of different wavelength of monochromatic light.***

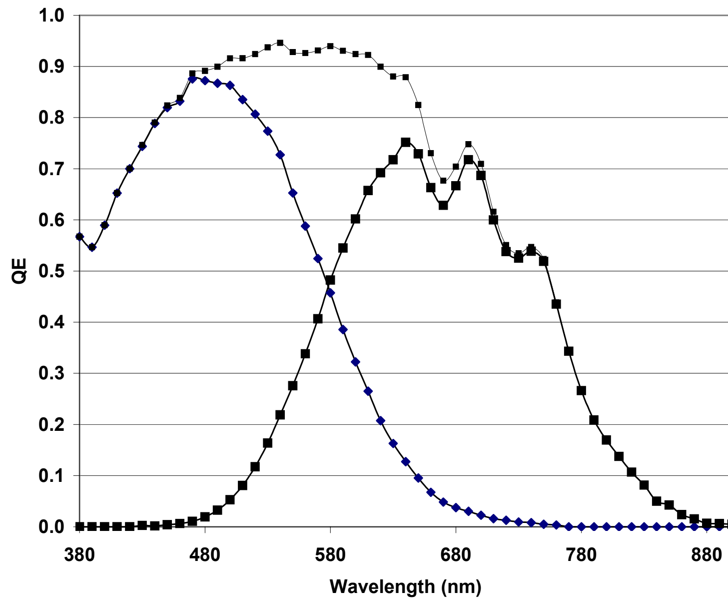


***Fig. 13-3: Quantum efficiency curves of a tandem-junction a-Si/a-SiGe solar cell used in this study to illustrate the method.***

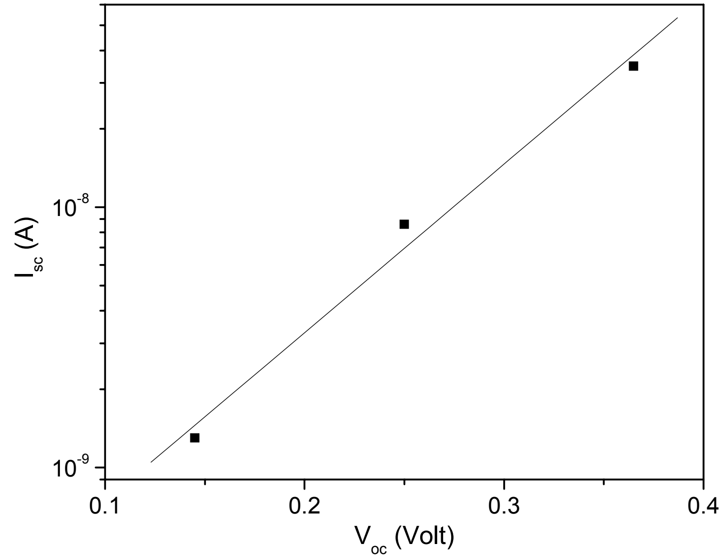


***Fig. 13-4: Relationship between $V_{oc}$ and $I_{sc}$ of top component cell in a tandem cell under variation of 400 nm light intensity.***

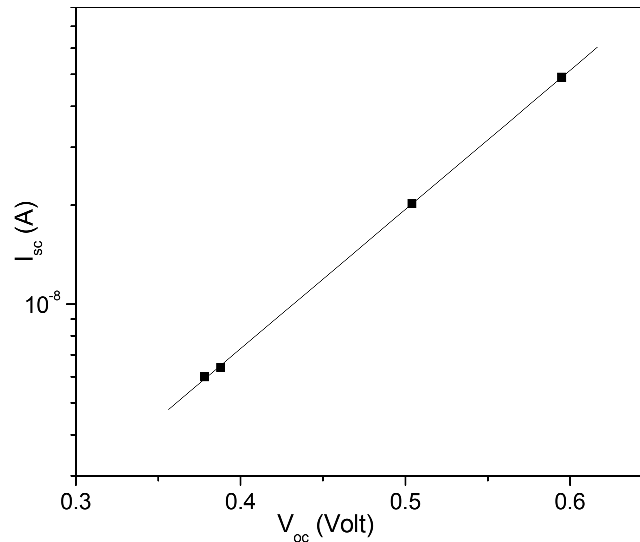


***Fig. 13-5: Relationship between $V_{oc}$ and $I_{sc}$ of bottom component cell in a tandem cell under variation of 700 nm light intensity.***

Step 1B: A similar approach is taken for measuring the $V_{oc}$ (bottom) and $I_{sc}$ (bottom) relationship except that in this case the red light is a 700 nm monochromatic light and the blue light is from the tungsten lamp with a 470 nm short-pass filter. Under the 700 nm red light, the top cell is in dark and does not contribute to the tandem cell $V_{oc}$. The tandem cell $V_{oc}$ is therefore the $V_{oc}$ of the bottom cell. The blue bias light allows one to measure $I_{sc}$ (bottom). The obtained $V_{oc}$ (bottom) and $I_{sc}$ (bottom) relationship is shown in Fig. 13-5.

Step 1C: Under a given illumination, the $I_{sc}$ (tandem) is either $I_{sc}$ (top) or $I_{sc}$ (bottom) depending on the relative intensity of the blue and red light. Fig. 13-6 shows the $I_{sc}$ of a tandem

cell under illumination of a fixed-intensity blue light and a varying-intensity red light. The $I_{sc}$ (tandem) is plotted against the intensity of the red light measured with a detector voltage response. At the highest red-light intensity, the current of the tandem cell is limited by the top-cell current and with the decrease of the red-light intensity to a certain level, this current remains almost constant. Further reduction of red-light intensity makes the tandem cell current to be limited by the bottom-cell current and thus the tandem-cell current decreases with the red-light intensity. The point of inversion, where the dependence on limitation of component current shifts, is obtained by the sharp change of the slope of the curve. At this point, both the component cells have the same current, i.e. $I_{sc}$ (top) = $I_{sc}$ (bottom)= $4.54 \times 10^{-8}$ A, for the sample shown in Fig. 13-6. Generally, at low red-light intensity, the tandem-cell current is limited by the bottom cell, while at high red-light intensity, the tandem is limited by the top cell. By increasing the red and blue light separately from a given illumination, one can determine the $I_{sc}$ (top) and $I_{sc}$ (bottom) of the tandem cell under this given illumination.

Step 1D: The $V_{oc}$ of the top and bottom component cells of the tandem cell under the given illumination is then obtained from the $I_{sc}$ (top) and $I_{sc}$ (bottom) values from Step 1C and the $I_{sc}$ vs $V_{oc}$ relationships from Steps 1A (Fig. 13-4) and 1B (Fig. 13-5). A given illumination is used as an example to illustrate the procedures. Under this illumination, the $I_{sc}$(top) and $I_{sc}$(bottom) as determined from Step 1C were $3.7 \times 10^{-8}$A and $4.54 \times 10^{-8}$A, respectively. The $V_{oc}$ (tandem) under this given illumination is measured to be 0.815V. Using the $I_{sc}$ vs $V_{oc}$ curves established in Step 1A (Fig. 13-4) and Step 1B (Fig. 13-5), the calculated open circuit voltages for the top and bottom cells, $V'_{oc}$(top) and $V'_{oc}$(bottom), are 0.354V and 0.593V, respectively, and the total combined voltage, $V'_{oc}$(tandem), is 0.947V.

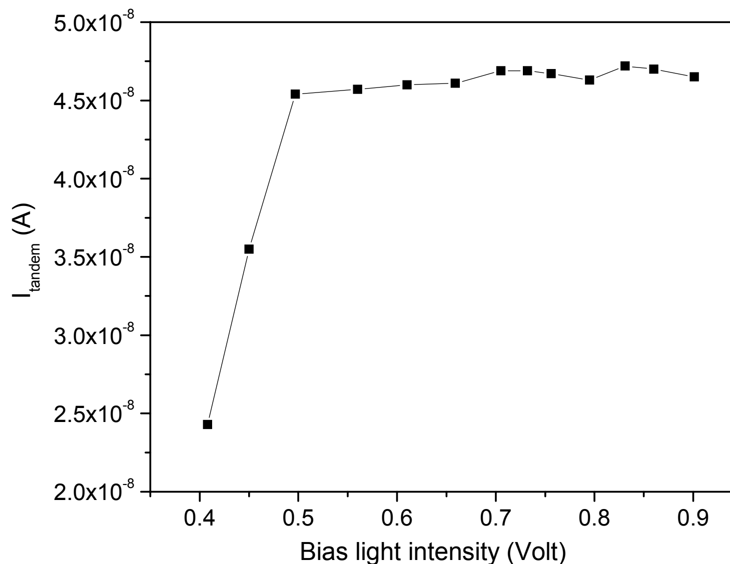


***Fig. 13-6: Variation of tandem cell current ($I_{tandem}$) with variation of intensity of red light as a function of detector voltage.***

Step 1E: $V'_{oc}$(tandem) is higher than 0.815V, the measured value for $V_{oc}$(tandem). This is because during Step 1A (Step 1B) when the tandem cell is illuminated with blue (red) light, the bottom (top) cell may generate a small voltage even though most of the blue (red) light is

absorbed by the top (bottom) cell. Assuming that the error introduced in Steps 1A and 1B are about the same magnitude, we obtain the $V_{oc}$(top)=$V_{oc}$'(top)×[$V_{oc}$(tandem)/V'$_{oc}$(tandem)] =0.305V and $V_{oc}$(bottom) = $V_{oc}$'(bottom) × [$V_{oc}$(tandem)/ V'$_{oc}$(tandem)] =0.510V, under the given illumination in this example.

Step2. Measurement of $I_{sc}$ and FF of component cells

Step 2A: The tandem cell is kept under the illumination described above, which generates higher $I_{sc}$ (bottom) than $I_{sc}$ (top). A varying electrical bias is applied on the tandem cell to scan the I(tandem) *vs* V(tandem) characteristics. In this case, I(tandem) is I(top) since the current of the tandem cell is limited by that of the top cell.

Step 2B: Near the maximum-power operating point of the tandem device in which the current is limited by the top, the voltage of the bottom cell is approximately $V_{oc}$ (bottom). Subtracting $V_{oc}$ (bottom) obtained in Step 1E, we obtain the voltage of the top cell V(top) = [V(tandem) – $V_{oc}$(bottom)], which, combined with the I(top), provides the I-V characteristics of the top component cell, as shown in Fig. 13-7 for the given illumination described above.

Step 2C: A different illumination which has stronger blue light, is used to measure the component cell I-V characteristics of the bottom cell. The result is shown in Fig. 13-8.

The I-V curves shown in Figures 7 & 8 represent the I-V curves of the top and bottom component cells respectively in the a-Si/a-SiGe tandem-junction solar cell under the given illumination. The FF for the top and bottom components under this illumination are calculated as 0.48 and 0.27 respectively. Same method could be used to determine the I-V characteristic for the device under 1-sun illumination.

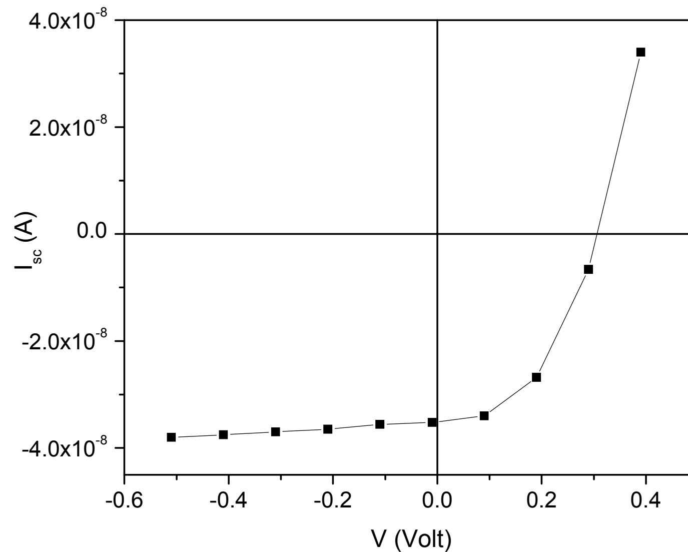


***Fig. 13-7: I-V characteristic of top component cell in a tandem-junction cell.***

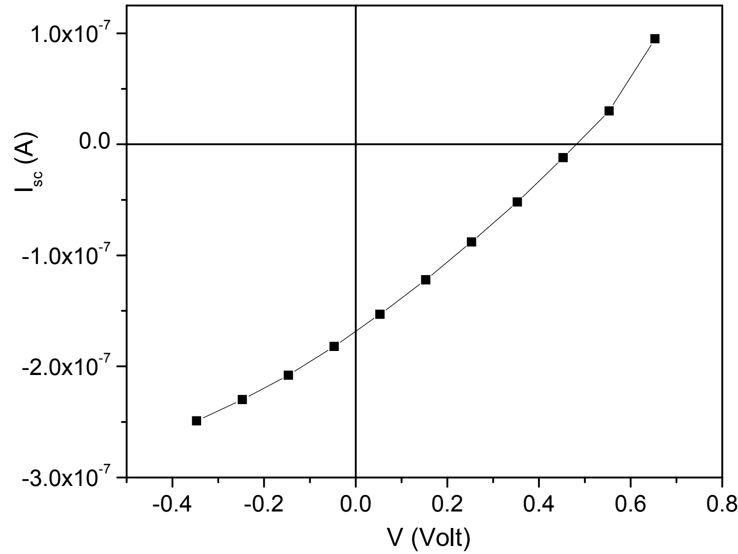


***Fig. 13-8: I-V characteristic of bottom component cell in a tandem-junction cell.***

## 13.4 Conclusion

A new method to measure the component cell I-V characteristics of a multiple-junction, two-terminal cell has been developed [2] and described. The new method is demonstrated to measure the component-cell I-V characteristics of the tandem-junction cell effectively. Further works are ongoing to demonstrate the method for 1-sun illumination and for triple-junction solar cells.

**References:**

1. S. Kurtz, K. Emery and J. M. Olson, Proc. of 1st WCPEC, 1773 (1994).
2. X. Deng, "Method for Measuring Component Cell Current-Voltage Characteristics in a Multi-junction, Two-terminal Stacked Solar Cell", University of Toledo Invention Disclosures for Patent Application, April 11, 2002 and July 9, 2004.
3. J. Burdick and T. Gletfelter, Solar Cells 18, 301 (1986).

# 14 Amorphous Silicon Based Minimodules with Silicone Elastomer Encapsulation

*Contributors: Aarohi Vijh and Xunming Deng*

## 14.1 Introduction

Ethyl vinyl acetate (EVA) is the most commonly used material for the encapsulation of terrestrial solar cells. It is well known that EVA turns yellow upon extended exposure to ultraviolet light. This yellowing upon exposure to UV light is a characteristic of most carbon based polymers. Silicon-based polymers (silicones) may not show this effect. Although silicones were used to encapsulate solar cells in the 1970s and 1980s, they were dropped in favour of ethyl vinyl acetate due to its lower cost [1]. However, the price of silicone elastomers has come down over the years and their quality and ease of application have improved, which may make them suitable for encapsulating solar cells once again. We have recently fabricated 4"x 4" and 4"x8" minimodules encapsulated with a combination of a silicone elastomer and Dupont Tefzel.

## 14.2 Experimental Details

The silicone used in our experiments was Dow Corning's Sylgard 182. Sylgard 182 is a blend of silanes $(\text{-Si-})_n$ and siloxanes $(\text{-Si-O-Si-})_n$ with alkyl groups substituting some of the hydrogen atoms, i.e. it has a silicon backbone, which makes it different from carbon based polymers such as EVA. Glass slides were encapsulated on both sides with EVA/Tefzel and silicone elastomer/Tefzel in a vacuum laminator. The EVA was obtained from Specialized Technology Resources. Figure 14-1 compares the light transmission of these samples with that of a plain glass slide.

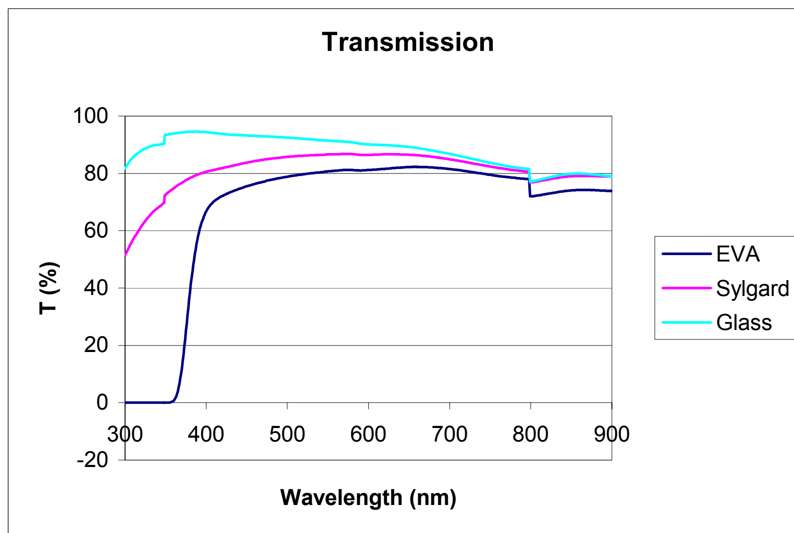


***Fig. 14-1: Transmission of glass encapsulated with EVA and Sylgard.***

In the thickness applied, the Sylgard-encapsulated slide showed better light transmission throughout the visible wavelength range than the EVA encapsulated slide. Its UV cutoff was more gradual than that of EVA, which blocked all light of wavelength shorter than 360 nm.

Two minimodules were then fabricated from 4”x4” single junction amorphous silicon-germanium solar cells and encapsulated with Sylgard 182 and Tefzel in the vacuum laminator. The first minimodule had a single 4”x4” a-SiGe n-i-p cell while the second consisted of two 4”x4” cells in series. Each cell had an active area of approximately 81 $cm^2$. Current collection grids consisting of tinned copper wire applied to the ITO front contact with conductive silver paint for the series interconnected cells, and conducting graphite paint for the single cell. Reverse-protection diodes were also attached between the bus bars of the cells. Before application of grids, the cells were shunt-passivated using a light-assisted electrochemical method [2], details of which will be reported separately. The cells were then vacuum laminated with Sylgard 182 and Tefzel at 125°C for 30 minutes. Being a liquid, Sylgard 182 flows well, and no trapped bubbles were found in the laminated minimodules. Coverage of raised features (e.g. the diodes and grid lines) was excellent. Figure 14-2 shows a photo of the 4”x4” and 4”x8” minimodules. The discolouration on the surface of the cells is a result of the shunt passivation process.

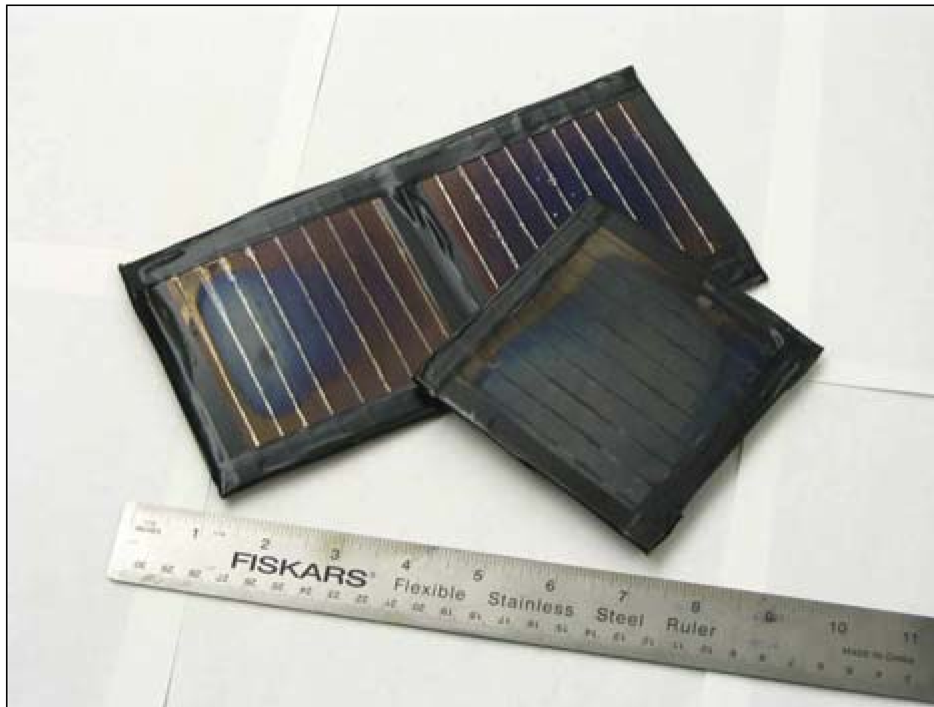


***Fig. 14-2: Silicone elastomer encapsulated a-SiGe based minimodules***

The cells produced the expected open circuit voltages of 0.8 V and 1.6 V for the single and two-cell minimodules, respectively. The short circuit current was 183 mA for the 4”x4” minimodule, and 760 mA for the 4”x8” interconnected minimodule, corresponding to current densities of 2.2 and 9.4 $mA/cm^2$, respectively. The currents were limited by the series resistance of the grids and interconnects, which at approximately 1 Ω per cell for the silver paint-attached

grids and 4 Ω per cell for the carbon paint-attached grids, were excessive for the expected $I_{sc}$ of ~1.6A. With the reverse protection diodes removed and under a reverse bias, the current in the 4"x8" minimodule increased to approximately 1.0A.

## 14.3 Conclusion

Both minimodules encapsulated with silicone elastomer functioned well. The quality of the encapsulant in terms of adhesion and bubble-free lamination was found to be good. Its light transmission for the thickness applied was found to be better than that of EVA. We conclude that silicone elastomers can be used as an alternative encapsulant for encapsulating solar cells.

### References


1. Muirhead, I.J. and Hawkins, B.K., *An assessment of photovoltaic power in the Telstra network*, Annual Conference of the Australian and New Zealand Solar Energy Society – SOLAR, 1995

2. Vijh, A. and Deng, X., *Light Assisted Shunt Passivation for Amorphous Silicon Photovoltaics,* Patent Application submitted to USPTO, April 2004.

# 15 Expansion of UT's Fabrication Capability for Triple-Junction Amorphous Silicon Based Solar Cells

*Contributors: H. Povolny and X. Deng*

Triple junction solar cells have been fabricated at UT using a multi-chamber rf PECVD deposition system made by GSI in 1990. The original system consisted of two PECVD deposition chambers and a load chamber. Figure 1 shows a photo of the original system. Several years ago, the load chamber was converted to become a dual purpose chamber: 1) designated deposition chamber for the n-type Si:H based materials and 2) the load lock chamber.

The three PECVD deposition chambers produce high quality amorphous and microcrystalline silicon and silicon germanium alloy with the each of the doped layers, n and p, deposited in a dedicated deposition chamber. The chamber dedicated to intrinsic silicon and silicon germanium alloys has been equipped with a VHF power supply and impedance matching network in order to explore the deposition process and film quality at higher frequency. This allows us to deposit high-quality materials at higher deposition rates than can be achieved with standard RF PECVD.

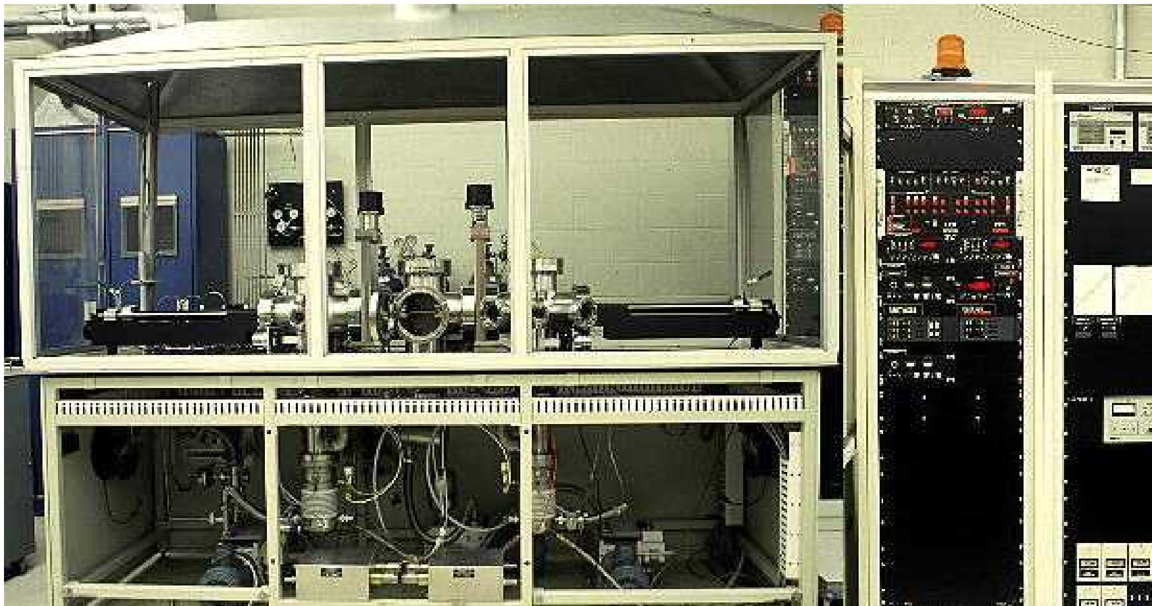

***Fig. 15-1: A photo of UT's PECVD system before expansion.***

A novel Hot-Wire CVD chamber was also added several years ago to explore high deposition rate microcrystalline silicon as well as high deposition rates of amorphous silicon.

Figure 15-2 shows a photo of the HWCVD system. The chamber uses a coiled filament design which leads to extremely high gas disassociation rates. There are three separate gas inlets, one directed through the coiled filament, an annular gas inlet just above the filament, and an annular gas inlet just below the substrate. This allows us to study the effects of gas injection position on film growth and film properties. Finally, the chamber includes RF cathode so that PECVD can be done as well.

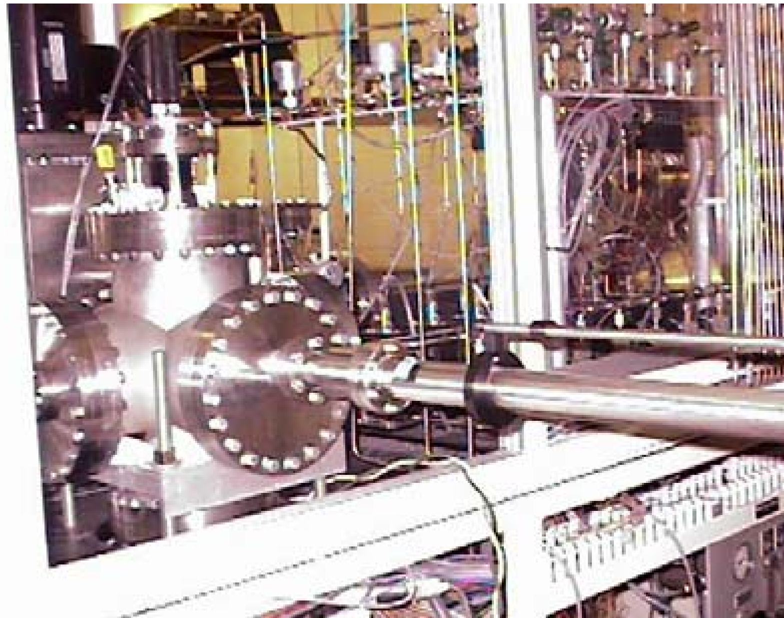

***Fig. 15-2: A photo of UT's HWCVD chamber integrated to the multi-chamber PECVD system.***

During this program period, we have carried out a major expansion to this deposition system to include 4 sputter deposition chambers and an additional load lock chamber. With this expansion, all of the 12 layers in a triple-junction solar cells, Al/ZnO/nipnipnip/ITO, can be made without vacuum break at the interfaces. Fig. 15-3 shows a AutoCAD drawing of the system before the expansion and Fig. 15-4 shows the AutoCAD drawing of four additional chambers (1 load lock and 3 sputter chambers for Al, ZnO and ITO, as previously designed).

The four sputter chambers were added for the purpose of making back reflector and top contact layers, as well as other metal and oxide layers, without vacuum break. Each sputter chamber has a sample rotation stage so that we can evenly coat a four inch square substrate using only a three inch diameter sputter target. A second gas inlet allows for reactive sputtering and an easily accessible bottom flange allows for the possibility of incorporating other processes into our system with minimal difficulty or downtime.

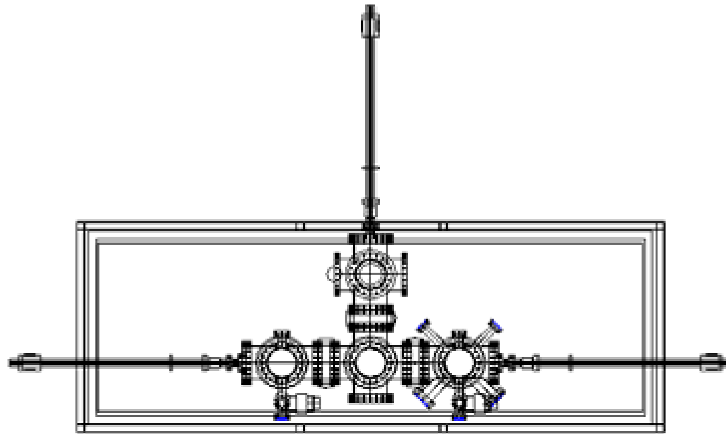

***Fig. 15-3: AutoCAD drawing of the PECVD/HWCVD system before recent expansion.***

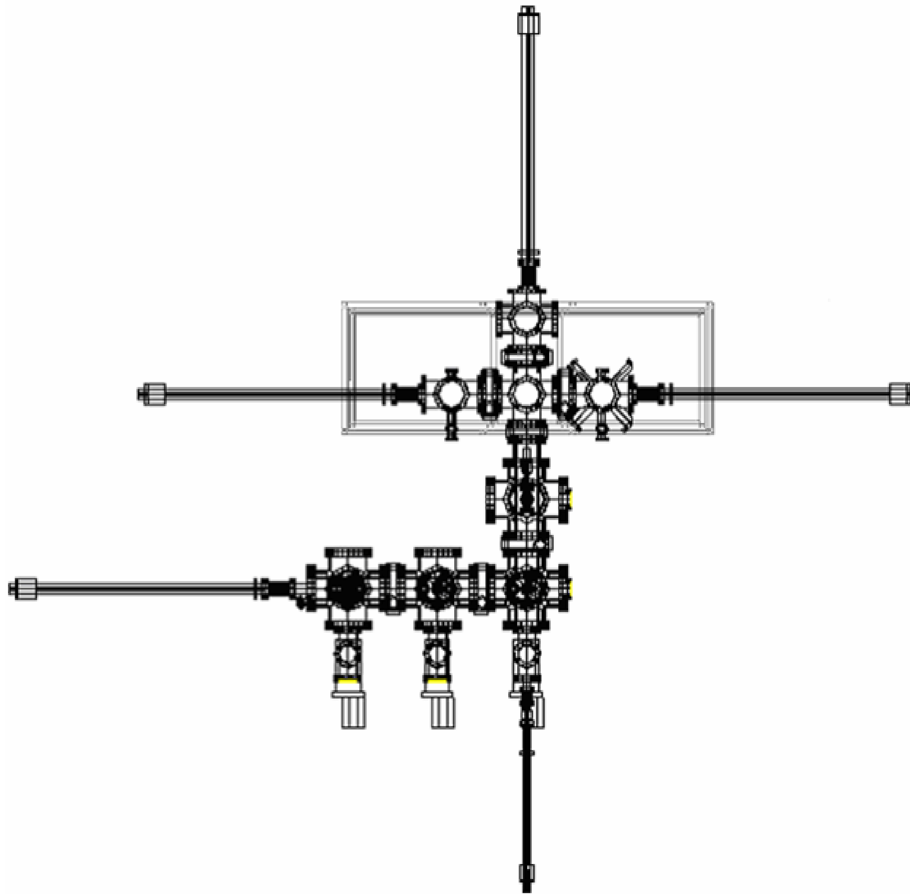

***Fig. 15-4: AutoCAD drawing of the multi-chamber deposition system with additional chambers (1 load lock and 3 sputtering chambers for Al, ZnO and ITO layers, as previously planned).***

The load-lock chamber is equipped with a substrate elevator capable of holding up to ten individually selectable substrates at one time. This is vital for any system of this size and versatility so that multiple chambers can be used at the same time without interfering with each other and without requiring a vacuum break. Partially completed devices can be stored in the load chamber until the next chamber and operator are ready for them without interfering with the workings of any of the other chambers. The elevator is equipped with a manipulator arm so that substrates can be moved between holders with different masks in situ. With appropriate masks, this allows us to perform combinatorial design of experiment in addition to simple patterning of individual layers.

Over all, the expanded combination HWCVD/PECVD/VHFPECVD/Sputter deposition system with integral load-lock incorporating multiple substrate capability with interchangeable masks provides remarkable versatility to carry out a variety of key studies in various aspects of photovoltaic devices.

The design and the optimization of this four additional sputter chambers are supported by NREL while the acquisition of the system components and the installation were supported by a research grant from Air Force Research Laboratory. Figure 15-5 is a photo of the entire system with nine chambers--3 PECVD, 1 HWCVD, 4 Sputtering, and 1 Load lock chambers. Initial films have already been made using these new sputter chambers. The optimization is underway and will be reported extensively in the next Quarterly Report.

***Fig. 15-5: Photo of the entire system with nine chambers--3 PECVD, 1 HWCVD, 4 Sputtering, and 1 Load lock chambers.***

# REPORT DOCUMENTATION PAGE

*Form Approved*
*OMB No. 0704-0188*

The public reporting burden for this collection of information is estimated to average 1 hour per response, including the time for reviewing instructions, searching existing data sources, gathering and maintaining the data needed, and completing and reviewing the collection of information. Send comments regarding this burden estimate or any other aspect of this collection of information, including suggestions for reducing the burden, to Department of Defense, Executive Services and Communications Directorate (0704-0188). Respondents should be aware that notwithstanding any other provision of law, no person shall be subject to any penalty for failing to comply with a collection of information if it does not display a currently valid OMB control number.

**PLEASE DO NOT RETURN YOUR FORM TO THE ABOVE ORGANIZATION.**

**1. REPORT DATE** *(DD-MM-YYYY)*
January 2006

**2. REPORT TYPE**
Subcontract Report

**3. DATES COVERED** *(From - To)*
1 September 2001–6 March 2005

**4. TITLE AND SUBTITLE**
High Efficiency and High Rate Deposited Amorphous Silicon-Based Solar Cells: Final Technical Report, 1 September 2001 – 6 March 2005

**5a. CONTRACT NUMBER**
DE-AC36-99-GO10337

**5b. GRANT NUMBER**

**5c. PROGRAM ELEMENT NUMBER**

**6. AUTHOR(S)**
X. Deng

**5d. PROJECT NUMBER**
NREL/SR-520-39091

**5e. TASK NUMBER**
PVB65101

**5f. WORK UNIT NUMBER**

**7. PERFORMING ORGANIZATION NAME(S) AND ADDRESS(ES)**
Department of Physics and Astronomy
University of Toledo
Toledo, OH 43606

**8. PERFORMING ORGANIZATION REPORT NUMBER**
NDJ-2-30630-08

**9. SPONSORING/MONITORING AGENCY NAME(S) AND ADDRESS(ES)**
National Renewable Energy Laboratory
1617 Cole Blvd.
Golden, CO 80401-3393

**10. SPONSOR/MONITOR'S ACRONYM(S)**
NREL

**11. SPONSORING/MONITORING AGENCY REPORT NUMBER**
NREL/SR-520-39091

**12. DISTRIBUTION AVAILABILITY STATEMENT**
National Technical Information Service
U.S. Department of Commerce
5285 Port Royal Road
Springfield, VA 22161

**13. SUPPLEMENTARY NOTES**
NREL Technical Monitor: Bolko von Roedern

**14. ABSTRACT** *(Maximum **200 Words**)*

The objectives for the University of Toledo are to: (1) establish a transferable knowledge and technology base for fabricating high-efficiency triple-junction a-Si-based solar cells, and (2) develop high-rate deposition techniques for growing a-Si-based and related alloys, including poly-Si, μc-Si, a-SiGe, and a-Si films and photovoltaic devices with these materials.

**15. SUBJECT TERMS**
PV; high efficiency, high-rate deposition; triple-junction; solar cells; devices; amorphous silicon;

| `+ | | | 17. LIMITATION OF ABSTRACT | 18. NUMBER OF PAGES | 19a. NAME OF RESPONSIBLE PERSON |
|---|---|---|---|---|---|
| a. REPORT | b. ABSTRACT | c. THIS PAGE | | | |
| Unclassified | Unclassified | Unclassified | UL | | 19b. TELEPONE NUMBER (*Include area code*) |

**Standard Form 298** (Rev. 8/98)
Prescribed by ANSI Std. Z39.18

F1146-E(05/2004)